Investigations of gradient-drift and two-stream instabilities with analytical models and Particle-in-Cell simulations

A Thesis Submitted to the College of Graduate and Postdoctoral Studies
in Partial Fulfilment of the Requirements for the degree of
Master of Science

in the Department of Physics and Engineering Physics
University of Saskatchewan
Saskatoon

by
Mina Papahn Zadeh

Permission to use

In presenting this thesis in partial fulfillment of the requirements for a Postgraduate degree from the University of Saskatchewan, I agree that the Libraries of this University may make it freely available for inspection. I further agree that permission for copying of this thesis in any manner, in whole or in part, for scholarly purposes may be granted by the professor or professors who supervised my thesis work or, in their absence, by the Head of the Department or the Dean of the College in which my thesis work was done. It is understood that any copying or publication, or use of this thesis or parts thereof for financial gain shall not be allowed without my written permission. It is also understood that due recognition shall be given to me and to the University of Saskatchewan in any scholarly use which may be made of any material in my thesis.

Requests for permission to copy or to make other use of the material in this thesis in whole or part should be addressed to:

Head of the Department of Physics and Engineering Physics
Physics Building
116 Science Place
University of Saskatchewan
Saskatoon, Saskatchewan S7N 5E2
Canada
OR
Dean
College of Graduate and Postdoctoral Studies
University of Saskatchewan
116 Thorvaldson Building, 110 Science Place
Saskatoon, Saskatchewan S7N 5C9
Canada

Abstract

Plasmas with drifting electrons in crossed electric **E** and magnetic **B** field are used as ion sources in several applications including space propulsion and material processing. Despite long history, the nature of plasma instabilities in specific systems remains obscure. Gradient drift modes driven by combinations of the electron $\mathbf{E} \times \mathbf{B}$ drift and density gradient have been considered as one of the primary sources of fluctuations. In this work, we have verified the linear instability criteria for three possible regimes: ion-acoustic, modified two-stream, and electron cyclotron drift modes without the effect of the density gradients. For plasma parameters of interest for electric propulsion, we have studied the effects of finite values of the wave vector along the magnetic field and investigated the broadening and overlap of the cyclotron resonances and the transitions toward the ion-acoustic regime.

Studying the influence of density gradient on the Electron Cyclotron Drift Instability (ECDI), we show that for purely azimuthal modes, instabilities are enhanced for negative gradient density, while the positive gradients reduce growth rates. The lower-hybrid modes, which are a special case of more general ECDI, are then studied by eigenfrequencies analysis from the kinetic theory and comparison with an advanced fluid model, verifying the validity of the fluid model for different limits. The results indicate that in linear stage, the growth rates from the fluid model agree well with the kinetic theory.

This research also looks at the linear and nonlinear aspects of Buneman instability in magnetized and unmagnetized plasma, as a limit of ECDI. In this regard, the 1D (one-dimensional) particle in cell (PIC) simulations in the limit of cold electrons for the magnetized case are performed. The linear stage of the instability agrees well with the theoretical prediction. In the case of unmagnetized Buneman instability, it is found that in the regime of low drift velocity, the growth rate of the linear stage of the instability in 1D-PIC simulations differs significantly from the theoretical results. Hereof a series of highly resolved PIC simulations are performed with two different PIC codes. The initial noise due to particle discreteness is identified as a cause for discrepancies. The results of the performed simulations reveal that, although a quiet start scheme does not entirely solve the noise issue in PIC simulation, it improves the accuracy of linear growth rates.

Acknowledgements

I want to express my sincere gratitude to my supervisor, Professor Andrei Smolyakov, for his continuous support of my study, patience, motivation, enthusiasm, immense knowledge, and valuable comments. His guidance helped me to write my thesis despite many problems throughout my education.

I also wish to thank the government of Canada for providing this opportunity for me to study in a high-quality research environment.

I would also like to give my deepest gratitude to my committee members for their excellent suggestions that have notably improved this thesis. Specific thanks go to my friends in the theoretical plasma physics group: Arash Tavassoli, Oleksandr Chapurin, Trevor Zintel, Meghraj Sengupta, who created an exceptional research atmosphere and helped me with their advice and suggestions.

My special thanks are to my family, particularly my beloved husband and my strong and intelligent son, for their constant support, encouragement, and patience. I am very grateful to my parents for their eternal love and motivation.

Contents

List of tables

List of figures

List of symbols

$\mathbf{k}$	Wave vector
$\mathbf{E}$	Electric field
$\mathbf{B}$	Magnetic field
E_0	Magnitude of electric field
B_0	Magnitude of magnetic field
t	Time
$v_{t\alpha},\ v_t$	Thermal velocity of the particles type α
N_0	Total number of particles from each type species (electrons, ions)
$n_\alpha,\ n$	Number density of particle type α
$u_\alpha,\ u_\beta$	Average velocity of the particles type α and β
m_α	Mass of the particles type α
q_α	Charge of the particles type α
e	Charge of electron
$\mathbf{P}_\alpha$	Stress tensor of the particles type α
$p_\alpha,\ p$	Scalar pressure of the particles type α
K_B	Boltzmann constant
$T_\alpha,\ T$	Temperature of the particles type α
$\mathbf{I}$	Identity matrix
$\mathbf{\Pi}_\alpha$	Viscosity tensor
ν	Collision frequency
γ	Ratio of specific heats C_p/C_v
C_p	Heat capacity at constant pressure
C_v	Heat capacity at constant volume
N	Number of degrees of freedom
ϵ_0	Vacuum permittivity
μ_0	Vacuum permeability
$(\mathbf{x}, \mathbf{v})$	Coordinate of phase space
$(\mathbf{x}_i(t),\ \mathbf{v}_i(t))$	Coordinates of particles
N_α	Microscopic density of particles type α

$\mathbf{E}^M$	Microscopic electric field
$\mathbf{B}^M$	Microscopic magnetic field
ρ^M	Microscopic charge density
$\mathbf{j}^M$	Microscopic current
$f_\alpha,\ f$	Single-particle distribution function
N	Density in $6N_0$-dimensional phase space
$\mathbf{X}_i(t)$	Set of positions $\mathbf{x}_i$ occupied by the ith particle at successive time t
$\mathbf{V}_i(t)$	Set of velocities $\mathbf{v}_i$ taken by the ith particle at successive time t
λ_D	Debye length
$f_{\alpha,\beta}$	Joint two-particle distribution function
ρ	Charge density
$\mathbf{j}$	Current density
f_n	Distribution function of neutral atoms
$\mathbf{p}$	Momentum
$H,\ H_\perp$	Energy, perpendicular energy
$f_{0\alpha}$	Equilibrium distribution function
$n_{0\alpha}$	Initial density of particles type α
ω	Frequency
$\tilde{f}_\alpha$	Perturbed distribution function
$\tilde{\mathbf{E}}$	Perturbed electric field
$\tilde{\phi}$	Perturbed potential
$\tilde{n}_\alpha$	Perturbed density of particles type α
K_α	Susceptibility of particles type α
$\omega_{p\alpha}$	Plasma frequency of particles type α
$Z(\xi)$	Plasma dispersion function
$\Omega_{c\alpha}$	Cyclotron frequency Of particles type α
ρ_α	Larmor radius of charged particle type α
I_m	Modified Bessel function of order m
$\mathbf{v}_n$	Diamagnetic drift or density gradient drift velocity
L_n	Density gradient length
$\mathbf{v}_E$	$\mathbf{E}\times\mathbf{B}$ Drift velocity
c_s	Ion sound velocity
γ	Growth rate
α	Angle between k and k_y
$G(1,1)$	Gordeyev integral
v_T	Temperature gradient drift velocity
v_B	Average ∇B drift velocity
v_d	Net drift velocity

$L_T,\ L_B$	Temperature gradient length, magnetic field gradient length
d	Plasma thickness in slab geometry & length of acceleration channel
$T_{\perp\alpha}$	Perpendicular temperature of particle type α
$v_{y\alpha}$	Flow velocity of particle type α
v_{0i}	Equilibrium ion flow
ω_{LH}	Lower-hybrid frequency
$n_0(x)$	Prescribed density in space
$f_0(v)$	Prescribed inlet velocity distribution function in velocity
N_w	Weight of macro-particle
N_D	Number of particles in the Debye cube
Δx	Spatial step
Δt	Time step
$N(j)$	Assigned number of particle to the jth grid point
N_p	Total number macro-particles
X_j	Spacial position of grid point
x_i	Coordinate of particle
v_i	Velocity of particle
$S(x)$	Particle shape function
$E_j,\ \phi_j$	Electric field and potential on the jth grid point
τ_p	Plasma oscillation period
τ_c	Particle-particle collision time
$\tilde{k}$	Numeric wave number
$\mathbf{v}_0$	Initial electron beam velocity
$\mathbf{v}_{(e,i)1}$	Perturbed electron or ion velocity
$n_{(e,i)1}$	Perturbed electron or ion density
$\mathbf{E}_1$	Perturbed electric field
$d(x')$	Density function
R_s	Numerical sequence
L	Size of simulation box
m	Mode number
x_0	Electron's equilibrium position
ϵ	Amplitude of perturbation
J_n	Bessel function of order of n

List of abbreviations

ECDI	Electron cyclotron drift instability
PIC	Particle-in-cell
1D	One dimension
2D	Two dimension
3D	Three dimension
1D2v	one spatial, two velocity
IAI	Ion acoustic instability
MTSI	Modified two-stream instability
LHDI	Lower-hybrid drift instability
MBTSI	Magnetized Buneman two-stream instability
BBGKY	Bogoliubov-Born-Gree-Kirkwood-Yvon
PDE	Partial differential equation
ODE	Ordinary differential equation
EQM	Equation of motion
PPC	Particle per cell
NGP	Nearest grid point
CIC	Cloud-in-cell
FFT	Fast Fourier transform
CFL	Courant-Friedrichs-Lewy

Chapter 1

Introduction

1.1 Motivation and thesis outline

The Hall thruster is an efficient electric propulsion device developed to replace chemical systems for many orbit propulsion tasks on geostationary satellites and long-range missions. In this annular device, a propellant that is usually xenon gas is ionized and then accelerated by the electric field. Figure (1.1) shows the Hall-thruster geometry that is used throughout my thesis.

In a Hall thruster, the axial electric field is created by the potential difference maintained between the central anode and the cathode placed near the open end of the thruster where the magnitude of magnetic field $\mathbf{B}$ is maximum. The cathode also serves as a source of electrons moving to the anode as well as the electrons neutralizing the accelerated ions. This radial magnetic field confines the electrons in the Larmor orbit and reduces axial electron mobility. The existence of the radial magnetic field and axial electric field cause the electrons to drift in the azimuthal direction, therefore, forming the Hall current. The ratio of E/B is selected such that the electron Larmor radius is much smaller, but the ion Larmor radius is much larger than the anode to cathode spacing. Hence, the ions can be freely accelerated out of the device and neutralized by the electrons from the cathode to maintain charge neutrality within the plasma plume.

Due to the difference in the magnitude of the electron and ion velocities, $\mathbf{v}_d = \mathbf{v}_e - \mathbf{v}_i$, various micro instabilities and plasma oscillations can develop in Hall thrusters. These phenomena play an essential role in controlling the transport, mobility of electrons, and even full thrust of the device. Hence, for improving the performance of Hall thrusters, we need to better understand the inner physical phenomena related to waves and instabilities. Since $\mathbf{v}_d$ varies as a function of position, different instabilities can dominate at different radial locations of Hall thruster devices. My thesis treats the main features of three types of instabilities (and their combinations) as listed below:

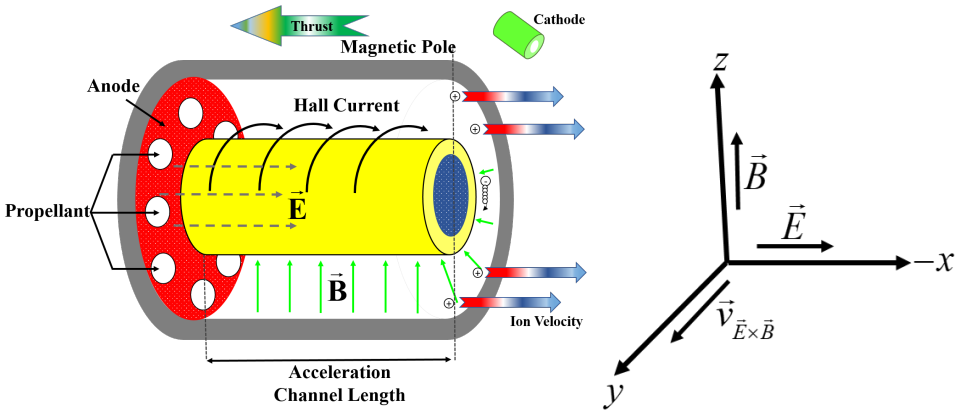

(a) (b)

Figure 1.1: (a) Schematic Hall Thruster and (b) $\mathbf{E} \times \mathbf{B}$ configuration of Hall thruster in Cartesian coordinate system, showing the relevant directions. Magnetic field $\mathbf{B}$ is in the radial direction (z) and the electric field $\mathbf{E}$ in the axial direction ($-x$). The electron drift velocity and direction of the fluctuating electric field is in the azimuthal direction (y).

1) Electron cyclotron drift,
2) Lower-hybrid-drift ($\mathbf{k} \cdot \mathbf{B} = 0$),
3) Buneman (cold electron-ion two-stream).

Chapter 1 reviews the basic plasma models, waves in partially magnetized plasma. Chapter 2 is devoted to a study of the linear aspects of electron cyclotron drift instability (ECDI) through the numerical solution of general dispersion relation with and without gradient of density. In chapter 3, I analyze the stability of lower hybrid drift from the fluid and kinetic approach.

As we are interested in the nonlinear aspect of plasma instabilities, I use one of the simulation methods called particle-in-cell (PIC). Chapter 4 shows the basic ideas of the PIC algorithm.

Electron cyclotron drift instability as one of the possible instabilities of Hall thruster has the limit of Buneman instability. Therefore, in chapter 5, I study the linear and nonlinear aspects of the simple case of Buneman instability in magnetized and unmagnetized plasma through 1D-PIC simulations.

The derivations of the dispersion relations in chapters 2 and 3 follow the standard treatments presented in previous literature. I solve the dispersion relation of the ECDI multi resonance using the Python solver developed originally in our group by O. Chapurin and S. Janhunen. In chapter 3, I use my own Python solver to compare the dispersion relations of fluid and the kinetic theories, this comparison is performed for the first time, as presented. I produce all numerical solutions and present the results graphically in various regimes of interest for our applications. A new regime of low-hybrid instability is revealed

in chapter 3. The presentation of the basics of the PIC method in chapter 5 follows the previous literature. In chapter 5, I perform PIC simulations using the commercial (VSim) and open source (Xes1) PIC codes. Parts of the results presented in chapter 5 are published in Ref. [1] and in another paper being prepared for publication [2].

1.2 Plasma models

Plasma is a quasi-neutral gas of charged particles that exhibits collective behavior due to the long range of the Coulomb force. The existence of various forms of interactions among different particles leads to many phenomena. Self-consistent electric and magnetic fields affect the particle orbits, and particle orbits affect the fields. Therefore, the general solution to any problem in plasma physics can be pretty complicated. These difficulties impel scientists to use mathematical modeling for studying plasma. A large number of different models are used for plasma systems that can be expressed in the form of integrodifferential equations. Each of these approaches can explain the different properties of the plasma. Among these approaches, kinetic and fluid methods are most general.

1.2.1 Fluid plasma model

The most straightforward description of plasma is provided by a fluid model that is sufficiently accurate to describe many plasma phenomena at a large scale based on macroscopic quantities such as density, momentum, temperature, etc.

A huge number of particles in plasma make it impossible to trace the motion of individual ones by Newton's equation. On the other hand, the frequent collision between particles keeps them moving together in a fluid element. Therefore, we study the motion of these fluid elements based on the self-consistent forces from the average electric and magnetic fields produced by many other particles. From the fluid description's view, plasma can be partitioned into small boxes while particles do not stay inside them. They leave a box with a length size of l after a transit time $t = l/v_t$ where v_t is particles thermal velocity and particles from neighboring boxes enter this volume. In this regard, these boxes count the gain and loss of the total number of particles, the total momentum, or the heat content [3].

There are two main representations of fluid boxes. The first view considers fixed boxes in space and watches fluid move through the volume element (Eulerian), while in the second view, boxes are transformed to a moving frame and move as fluid moves (Lagrangian). Describing the evolution of plasma based on the fluid approach stands on the following set of fluid equations.

Continuity equation

The equation of continuity originated from matter conservation. It means that the total number of particles N_0 from each type (electrons, ions, or neutral particles) in a volume V can change if particles are generated or lost as a result of the collision, and there is a net flux of particles over the surface S enclosing that volume. This equation can be written as follows:

$$\frac{\partial n_\alpha}{\partial t} + \nabla \cdot (n_\alpha \mathbf{u}_\alpha) = \left(\frac{\delta n_\alpha}{\delta t}\right)_{coll}, \tag{1.1}$$

where n_α indicates the number density of particle type α, $n_\alpha \mathbf{u}_\alpha$ is the flux number density and $\delta n_\alpha / \delta t$ shows the collision term that is due to the ionization, recombination, attachment and so on. In the absence of interactions leading to the creation or destruction of particles of type α, the collision term is equal to zero.

Equation of motion

The evolution of plasma particles in a fluid box is controlled by electromagnetic Lorentz force, pressure force and collision. Therefore, the equation of motion can be written in general form,

$$m_\alpha n_\alpha [\frac{\partial \mathbf{u}_\alpha}{\partial t} + (\mathbf{u}_\alpha \cdot \nabla)\mathbf{u}_\alpha] = q_\alpha n_\alpha (\mathbf{E} + \mathbf{u}_\alpha \times \mathbf{B}) - \nabla \cdot \mathbf{P}_\alpha - m_\alpha n_\alpha (\mathbf{u}_\alpha - \mathbf{u}_\beta)\nu, \tag{1.2}$$

where $\mathbf{u}_\alpha$ is the average velocity of the particles type α that move together in the fluid (element) box, $\mathbf{P}_\alpha$ is stress tensor with components $P_{ij} = m_\alpha n_\alpha \overline{(u_i - u_{i,\alpha})(u_j - u_{j,\alpha})}$ that can be decomposed into two terms as $\mathbf{P}_\alpha = p_\alpha \mathbf{I} + \mathbf{\Pi}_\alpha$, where $p_\alpha = n_\alpha K_B T_\alpha$ is the scalar pressure, $\mathbf{\Pi}_\alpha$ is the viscosity tensor, and $\mathbf{I}$ is the identity matrix, $\nabla \cdot \mathbf{P}_\alpha$ indicates the force associated with the scalar pressure and viscous forces. For the Maxwellian distribution function, the off-diagonal elements of pressure tensor vanish $\mathbf{\Pi}_\alpha = 0$ and pressure tensor converts to the gradient of pressure. The last term of Eq. (1.2) represents a collision between particle type α with particle type β that has velocity $\mathbf{u}_\beta$ and ν is collision frequency.

Equation of state

In the simplest case, when the thermal conductivity is low, and most ways of energy transfer are neglected, the thermodynamic equation of state, which relates p to n for each species, describes the variation of p in time in plasma,

$$p = Cn^\gamma, \tag{1.3}$$

where C is a constant and γ indicates how much the temperature of a plasma increases when it is compressed. It is defined by the ratio of specific heats C_p/C_v. The term ∇p is

given by:

$$\frac{\nabla p}{p} = \gamma \frac{\nabla n}{n}. \tag{1.4}$$

For isothermal compression when the compression is slow compared to thermal conduction, $\gamma = 1$, and we have,

$$\nabla p = K_B T \nabla n, \tag{1.5}$$

and for enough fast compression compared to heat conduction we have adiabatic compression with $\gamma = (2 + N)/N$ which is larger than 1 due to the changes in $K_B T$. Here N denotes the number of degrees of freedom [4]. Maxwell equations are used to close the set of equations in fluid approximation of plasma.

$$\begin{aligned}
\nabla \times \mathbf{B} =& \mu_0 \epsilon_0 \frac{\partial \mathbf{E}}{\partial t} + \mu_0 \sum_\alpha (n_\alpha q_\alpha \mathbf{u}_\alpha), \\
\nabla \times \mathbf{E} =& -\frac{\partial \mathbf{B}}{\partial t}, \\
\epsilon_0 \nabla \cdot \mathbf{E} =& \sum_\alpha n_\alpha q_\alpha, \\
\nabla \cdot \mathbf{B} =& 0.
\end{aligned} \tag{1.6}$$

1.2.2 Kinetic plasma model

Dynamical processes in the statistical mechanics of plasma physics are often described by kinetic theory. A theoretical foundation for the kinetic theory of classical plasmas consists of four stages. The first stage is based on defining a six-dimensional phase-space distribution function called the "Klimontovich distribution function," which obeys a continuity equation in the phase-space. Then, investigating the dynamical behavior of the system of N-interacting particles using the Liouville equation, which is followed by multi-particle distribution functions, and finally, the system of charged particles described by BBGKY (Bogoliubov-Born-Gree-Kirkwood-Yvon) hierarchy equations. The following literature review is adapted from Ref. [5].

The microscopic density of particles type α in the phase space $(\mathbf{x}, \mathbf{v})$ is expressed by summation of the six-dimensional delta function,

$$N_\alpha(\mathbf{x}, \mathbf{v}, t) = \sum_{1 \le i \le N_0} \delta[\mathbf{x} - \mathbf{x}_i(t)] \delta[\mathbf{v} - \mathbf{v}_i(t)]], \tag{1.7}$$

as it is known as the Klimontovich distribution function. Here $(\mathbf{x}_i(t),\ \mathbf{v}_i(t))$ are the Lagrangian coordinates of particle itself, whereas $(\mathbf{x},\ \mathbf{v})$ are the Eulerian coordinates of the phase space and N_0 shows the number of particles for each species. Time development

of $N_\alpha(\mathbf{x}, \mathbf{v}, t)$ leads to Klimontovich equation as follows:

$$\frac{\partial N_\alpha(\mathbf{x}, \mathbf{v}, t)}{\partial t} + \mathbf{v} \cdot \frac{\partial N_\alpha(\mathbf{x}, \mathbf{v}, t)}{\partial \mathbf{x}} + \frac{q_\alpha}{m_\alpha}(\mathbf{E}^M + \mathbf{v} \times \mathbf{B}^M) \cdot \frac{\partial N_\alpha(\mathbf{x}, \mathbf{v}, t)}{\partial \mathbf{v}} = 0. \tag{1.8}$$

Here $\mathbf{E}^M$ and $\mathbf{B}^M$ are microscopic fields produced self consistently by point particles themselves, plus the externally applied fields that satisfy Maxwell's equations. Therefore, for completing the model, we need the Maxwell equations:

$$\begin{aligned}
\nabla \times \mathbf{B}^M =& \mu_0 \epsilon_0 \frac{\partial \mathbf{E}^M}{\partial t} + \mu_0 \mathbf{j}^M, \\
\nabla \times \mathbf{E}^M =& -\frac{\partial \mathbf{B}^M}{\partial t}, \\
\nabla \cdot \mathbf{E}^M =& \frac{1}{\epsilon_0} \rho^M, \\
\nabla \cdot \mathbf{B}^M =& 0,
\end{aligned} \tag{1.9}$$

where the microscopic charge density is

$$\rho^M = \sum_{\alpha=e,i} q_\alpha \int d^3 v N_\alpha(\mathbf{x}, \mathbf{v}, t), \tag{1.10}$$

and the microscopic current is

$$\mathbf{j}^M = \sum_{\alpha=e,i} q_\alpha \int d^3 v \mathbf{v} N_\alpha(\mathbf{x}, \mathbf{v}, t). \tag{1.11}$$

It is worth noting that conservation of particles in the phase space can be interpreted when we consider $dN_\alpha(\mathbf{x}, \mathbf{v}, t)/dt = 0$. Eqs. (1.8) and (1.9) provide a complete set for describing plasma behavior. However, since the Klimontovich equation contains all particle orbits, it is far too detailed for practical purposes, especially if we introduce the collisional effects into it. Therefore, a statistical approach is utilized by adding a random fluctuation term to each quantity that shows the microscopic scale of evolution.

$$\begin{aligned}
\mathbf{E}^M =& \mathbf{E} + \delta\mathbf{E}, \\
\mathbf{B}^M =& \mathbf{B} + \delta\mathbf{B}, \\
N_\alpha =& f_\alpha + \delta N_\alpha.
\end{aligned} \tag{1.12}$$

By definition, in plasma for scale larger than Debye length, the ensemble average of fluctuations $< \delta... >$ is zero. Therefore, we have $\mathbf{E} =< \mathbf{E}^M >$, $\mathbf{B} =< \mathbf{B}^M >$, and $f_\alpha(\mathbf{x}, \mathbf{v}, t) =< N_\alpha(\mathbf{x}, \mathbf{v}, t) >$. The ensemble averaging of the spiky function $N_\alpha(\mathbf{x}, \mathbf{v}, t)$ defined a smooth function called single-particle distribution function f_α and shows how many particles are likely to be found in a small volume box $\Delta\mathbf{x}\Delta\mathbf{v}$ of the phase space [5].

The Klimontovich equation describes the behavior of individual particles, while the

"Liouville equation" describes the behavior of plasma as a system of particles. Based on Klimontovich equation $N_\alpha(\mathbf{x}, \mathbf{v}, t)$ is the density of particles in six-dimensional phase space, while in a system with N_0 particles of Liouville equation, N is the density in $6N_0$-dimensional phase space, here $\mathbf{X}_i(t)$ and $\mathbf{V}_i(t)$ are the set of positions $\mathbf{x}_i$ and velocities $\mathbf{v}_i$ respectively taken by the ith particle at successive time t,

$$N(\mathbf{x}_1, \mathbf{v}_1, \mathbf{x}_2, \mathbf{v}_2, ...\mathbf{x}_{N_0}, \mathbf{v}_{N_0}, t) = \prod_{i=1}^{N_0} \delta[\mathbf{x}_i - \mathbf{X}_i(t)]\delta[\mathbf{v}_i - \mathbf{V}_i(t)]], \tag{1.13}$$

$$\frac{\partial N}{\partial t} + \sum_i^{N_0} \nabla_{\mathbf{x}_i} \cdot (\mathbf{v}_i N) + \sum_i^{N_0} \nabla_{\mathbf{v}_i} \cdot (\dot{\mathbf{V}}_i N) = \frac{dN}{dt}. \tag{1.14}$$

The Liouville equation describes the exact orbit of a single point in $6N_0$-dimensional phase space, and the ensemble of such a system gives practical information. The distribution function of a system f_{N_0} which is introduced as follows:

$$f_{N_0}(\mathbf{x}_1, \mathbf{v}_1, \mathbf{x}_2, \mathbf{v}_2, ...\mathbf{x}_{N_0}, \mathbf{v}_{N_0}, t) d\mathbf{x}_1 d\mathbf{v}_1 d\mathbf{x}_2 d\mathbf{v}_2 ... d\mathbf{x}_{N_0} d\mathbf{v}_{N_0}, \tag{1.15}$$

shows the probability that a particular system at time t has in $6N_0$-dimensional phase space at point $(\mathbf{x}_1, \mathbf{v}_1, \mathbf{x}_2, \mathbf{v}_2, ...\mathbf{x}_{N_0}, \mathbf{v}_{N_0})$. Also, it satisfies the Liouville equation for an N-body system,

$$\frac{D f_{N_0}}{Dt} = \frac{\partial f_{N_0}}{\partial t} + \sum_i^{N_0} \mathbf{v}_i \cdot \nabla_{\mathbf{x}_i} f_{N_0} + \sum_i^{N_0} \dot{\mathbf{V}}_i \cdot \nabla_{\mathbf{v}_i} f_{N_0}. \tag{1.16}$$

As discussed above, the density f_{N_0} represents the joint probability density that each particle has [5]. To be able to study this system, we consider reduced distributions that are functions of fewer variables, such as one-particle distribution function f_α which neglects the influence of its near neighbor, two-particle distribution function $f_{\alpha,\beta}$ that contains the interaction between two particles, or three-particle distribution function $f_{\alpha,\beta,\gamma}$ and so on. The Liouville equation for each case of the distribution function is coupled to the next higher distribution function through the acceleration term. This chain of statistical equations is known as the BBGKY hierarchy, and it can be solved by terminating the chain by ignoring particle interaction based on valid approximation [6].

Since for plasma, the range of the forces $r_0 \approx \lambda_D$ is much larger than interparticle spacing $n^{-1/3}$ the joint distribution $f_{\alpha,\beta}$ in a small volume V, $n^{-1} << V << \lambda_D^3$, is determined by particles that are outside of volume and independent of internal interaction of two particles, therefore $f_{\alpha,\beta} = f_\alpha f_\beta$. The simplest approximation to the chain of BBGKY hierarchy equations in plasma is, neglecting all terms of particle interactions. In this approximation, we will obtain a zero-order kinetic equation for plasma called the

Vlasov equation (1.17) or occasionally, the collisionless Boltzmann equation [6].

$$\frac{\partial f_\alpha(\mathbf{x},\mathbf{v},t)}{\partial t} + \mathbf{v}\cdot\nabla f_\alpha(\mathbf{x},\mathbf{v},t) + \frac{q_\alpha}{m_\alpha}(\mathbf{E}+\mathbf{v}\times\mathbf{B})\cdot\nabla_v f_\alpha(\mathbf{x},\mathbf{v},t) = 0, \tag{1.17}$$

where the symbol ∇ denotes the gradient in (x, y, z) space and ∇_v stands for gradient in velocity space. Here, the distribution function referred to the one-particle distribution function f_α. The assumption here is that the phase densities at different points in 6D phase space are completely independent, and there is just a collective interaction via electromagnetic fields. The Vlasov equation is valid when the number of particles in a Debye sphere becomes infinite. In this regard, any fluctuations due to the discreteness of the particles can be neglected.

Charge density and current density can be obtained at each point in space from the appropriate integrals of the distribution function,

$$\rho(\mathbf{x},t) = \sum_{\alpha=e,i} q_\alpha \int f_\alpha(\mathbf{x},\mathbf{v},t)d^3v, \tag{1.18}$$

$$\mathbf{j}(\mathbf{x},t) = \sum_{\alpha=e,i} q_\alpha \int \mathbf{v} f_\alpha(\mathbf{x},\mathbf{v},t)d^3v, \tag{1.19}$$

here $\mathbf{v}$ is the average flow velocity. Eqs. (1.17) to (1.19) and the Maxwell equations, form a closed set of self-consistent equations for f_α to be solved simultaneously and called the Vlasov-Maxwell system.

Since the Vlasov equation is a partial differential equation (PDE), the general solution of that can come from a characteristic system that converts PDE into ordinary differential equation (ODE). These characteristics are formally written as follows:

$$\frac{d\mathbf{x}}{\mathbf{v}} = dt, \tag{1.20}$$

$$\frac{d\mathbf{v}}{\frac{q_\alpha}{m_\alpha}[\mathbf{E}+\mathbf{v}\times\mathbf{B}]} = dt. \tag{1.21}$$

As particles move around in phase space, they follow the contours of constant distribution function f_α. Therefore the solution of ODEs pieces together to form a surface that provides a solution f_α to Vlasov equation.

The fundamental difference in the physical content between the Vlasov equation and the Klimontovich equation is worth noting. The Klimontovich equation deals with the microscopic distribution function, containing all the fine structures arising from the individuality of the particles. In contrast, the Vlasov equation is concerned with a coarse-grained distribution function obtained from a statistical average of the microscopic distribution function.

The first-order of the kinetic equation can be obtained by retaining two-particle dis-

tribution function in BBGKY hierarchy equations, which gives collisional correction to the Vlasov equation. In this regard, one method that can be practical to solve f_α is, modelling the $f_{\alpha,\beta}$. Such a case is the collisional Boltzmann equation. For instance, in the presence of collisions with neutral atoms, which is more common in cold plasmas, the Eq. (1.17) can be written by collision term that model by $\nu(f_n - f_\alpha)$,

$$\frac{\partial f_\alpha(\mathbf{x},\mathbf{v},t)}{\partial t} + \mathbf{v}\cdot\nabla f_\alpha(\mathbf{x},\mathbf{v},t) + \frac{q_\alpha}{m_\alpha}(\mathbf{E}+\mathbf{v}\times\mathbf{B})\cdot\nabla_v f_\alpha(\mathbf{x},\mathbf{v},t) = \nu(f_n - f_\alpha), \quad (1.22)$$

where f_n is the distribution function of neutral atoms and ν is constant collision frequency.

In an equilibrium when there are no external electric and magnetic fields, the most probable single-particle distribution function can be expressed by Maxwell-Boltzmann distribution. In this case, the constants of motion are energy and momentum, and the particle distribution function is only function of v [6],

$$\begin{aligned} \mathbf{p} =& m\mathbf{v}, \\ H =& \frac{m}{2}(v_x^2 + v_y^2 + v_y^2), \\ f_{0\alpha}(v_x, v_y, v_z) =& n_{0\alpha}\left(\frac{1}{2\pi v_{t\alpha}^2}\right)^{3/2}\exp\left(-\frac{v^2}{2v_{t\alpha}^2}\right), \end{aligned} \quad (1.23)$$

where $v_{t\alpha} = \sqrt{T_\alpha/m_\alpha}$ is thermal velocity particle type α. It is worth bearing in mind that in the case of longitudinal waves $\mathbf{k} \parallel \mathbf{E}$, where $\mathbf{k}$ is the wave vector and $\nabla\times\mathbf{E} = 0$, the magnetic field is stationary $\partial_t\mathbf{B} = 0$ and the system reduces to the electrostatic approximation which is used in the following.

The plasma fluid equations can be derived by taking velocity moments of the Vlasov Eq. (1.17). Its derivation can be found in general plasma physics books [7, 4].

1.3 Plasma waves

The foundation of plasma evolution is waves that propagate energy through plasma and send information outside for observers to reveal what is occurring inside the plasma. They can also become unstable, and their amplitudes grow to the point that they disrupt plasma confinement. In this section, I describe electrostatic waves in a homogeneous and inhomogeneous plasma.

1.3.1 Electrostatic waves in homogeneous plasma

In homogeneous plasma, the initial distribution functions of individual plasma species are free of any anisotropies, and it is independent of the position and direction of the velocity (1.23). Therefore, the imaginary part of wave frequency is zero or negative, and there are electrostatic fluctuations (waves) that are normal modes that may be slowly damped in time or space due to Landau damping [8]. Here we consider collisionless plasma to describe

the evolution of distribution function through the Vlasov equation. In the following, I study electrostatic waves in unmagnetized and magnetized plasma.

Electrostatic waves in unmagnetized homogeneous plasma

The main procedure for determining the electrostatic normal modes of plasma based on kinetic theory is applying Fourier/Laplace analysis in the linear Vlasov equation for getting particle densities fluctuation to insert into the Poisson equation. This procedure yields a dispersion relation that defines the relation between frequency and wave vector [8].

In this regard, we use Maxwellian distribution (1.23) for the stationary equilibrium state of plasma. For solving the unmagnetized Vlasov Eq. (1.17), we consider weak plasma fluctuations. This means that the fluctuating fields are sufficiently small in amplitude that both the electric field and the distribution functions can be expanded around equilibrium, in the following form:

$$f_\alpha(\mathbf{x},\mathbf{v},t) = f_{0\alpha}(\mathbf{x},\mathbf{v}) + \tilde{f}_\alpha(\mathbf{x},\mathbf{v},t), \tag{1.24}$$

$$\mathbf{E}(\mathbf{x},t) = \tilde{\mathbf{E}}(\mathbf{x},t). \tag{1.25}$$

The following relation is obtained after linearization of the Vlasov equation,

$$\frac{\partial \tilde{f}_\alpha}{\partial t} + \mathbf{v}\cdot\frac{\partial \tilde{f}_\alpha}{\partial \mathbf{x}} + \frac{q_\alpha}{m_\alpha}\tilde{\mathbf{E}}(\mathbf{x},t)\cdot\frac{\partial f_{0\alpha}}{\partial \mathbf{v}} = 0. \tag{1.26}$$

Seeking a solution in the form of $\tilde{h}(\mathbf{x},\mathbf{v},t) = \tilde{h}(\mathbf{k},\mathbf{v},\omega)e^{i\mathbf{k}.\mathbf{x}-i\omega t}$ leads us to find $\tilde{f}_\alpha$ from Eq. (1.26) in the Fourier space,

$$\tilde{f}_\alpha(\mathbf{k},\mathbf{v},\omega) = -\frac{q_\alpha}{m_\alpha(\omega-\mathbf{k}\cdot\mathbf{v})}\tilde{\phi}(k,\omega)\mathbf{k}\cdot\frac{\partial f_{0\alpha}}{\partial \mathbf{v}}, \tag{1.27}$$

where $\tilde{\phi}$ is the perturbed potential which is replaced by the fluctuating electric field originated from $\tilde{\mathbf{E}}(\mathbf{x},t) = -\nabla\tilde{\phi}(x,t)$. The density perturbation of αth type of particle can be calculated by integrating of perturbed distribution function over the velocity space,

$$\tilde{n}_\alpha(\mathbf{k},\omega) = \int \tilde{f}_\alpha d^3v = \frac{q_\alpha}{m_\alpha}\tilde{\phi}(k,\omega)\int\frac{d^3v}{(\mathbf{k}\cdot\mathbf{v}-\omega)}\mathbf{k}\cdot\frac{\partial f_{0\alpha}}{\partial \mathbf{v}}. \tag{1.28}$$

We can define the αth component of susceptibility as follows:

$$K_\alpha(\mathbf{k},\omega) = -\frac{\omega_{p\alpha}^2}{n_{0\alpha}k^2}\int\frac{d^3v}{(\mathbf{k}\cdot\mathbf{v}-\omega)}\mathbf{k}\cdot\frac{\partial f_{0\alpha}}{\partial \mathbf{v}}, \tag{1.29}$$

where $\omega_{p\alpha} = \sqrt{n_{0\alpha}q_\alpha^2/\epsilon_0 m_\alpha}$ denotes plasma frequency for species α, and

$$\tilde{n}_\alpha(\mathbf{k},\omega) = -\frac{k^2\epsilon_0}{q_\alpha}\tilde{\phi}(\mathbf{k},\omega)K_\alpha(\mathbf{k},\omega). \tag{1.30}$$

By using Poisson's equation, we get the linear dispersion equation:

$$1 + \sum_{\alpha} K_{\alpha}(\mathbf{k}, \omega) = 0, \tag{1.31}$$

Dispersion equation ($1 + \sum K_{\alpha}(\mathbf{k}, \omega) = 0$) shows the relationship between ω and k for the plasma modes. By using Eq. (1.29) the linear susceptibility can be written as follows:

$$K_{\alpha}(\mathbf{k}, \omega) = -\frac{\omega_{p\alpha}^2}{n_{0\alpha} k^2} \int \frac{dv_k}{(v_k - \omega/k_k)} \frac{\partial f_{0\alpha}}{\partial v_k}. \tag{1.32}$$

It should be noted that Eq. (1.32) contains one singularity at $\omega = k_k v_k$ due to the particle-wave resonant interaction where k_k is the wave vector along v_k that may be either positive or negative. There are two approaches for obtaining the eigenfrequencies of dispersion relation containing a singularity. The first approach is to take the principal value of the integral, as done by Vlasov in Ref. [9], therefore neglecting wave damping due to the Landau effect. The second approach is, using plasma dispersion function $Z(\xi)$ which appears in kinetic dispersion equations derived from Maxwellian or semi-Maxwellian distribution function and defined as follows:

$$Z(\xi) = \frac{1}{\sqrt{\pi}} \int_{-\infty}^{\infty} \frac{e^{-s^2}}{s - \xi} ds, \quad \mathrm{Im}\xi > 0. \tag{1.33}$$

And differential equation of that with respect to ξ is,

$$Z'(\xi) = \frac{-1}{\sqrt{\pi}} \int_{-\infty}^{\infty} \frac{2s e^{-s^2}}{s - \xi} ds, \tag{1.34}$$

which yields via the integration by parts,

$$Z'(\xi) = -2(1 + \xi Z(\xi)), \tag{1.35}$$

$$K_{\alpha}(\mathbf{k}, \omega) = \frac{2\omega_{p\alpha}^2}{k^2 v_{t\alpha}^2} [1 + \frac{\omega}{\sqrt{2} k_k v_{t\alpha}} \frac{1}{\sqrt{\pi}} \int_{-\infty}^{\infty} \frac{dv_k \exp(-v_k^2)}{v_k - \left(\frac{\omega}{\sqrt{2} k_k v_{t\alpha}}\right)}]. \tag{1.36}$$

The integral $\frac{1}{\sqrt{\pi}} \int_{-\infty}^{\infty} \frac{dv_k \exp(-v_k^2)}{v_k - \left(\frac{\omega}{\sqrt{2} k_k v_{t\alpha}}\right)}$ is Z and ξ is $\omega/\sqrt{2} k_k v_{t\alpha}$ that is a complex variable,

$$K_{\alpha}(\mathbf{k}, \omega) = -\frac{\omega_{p\alpha}^2}{2k^2 v_{t\alpha}^2} Z' \left(\frac{\omega}{\sqrt{2} k_k v_{t\alpha}} \right). \tag{1.37}$$

Therefore, we obtain the general dispersion relation of electrostatic waves in unmagnetized plasma:

$$1 - \sum_{\alpha} \frac{\omega_{p\alpha}^2}{2k^2 v_{t\alpha}^2} Z' \left(\frac{\omega}{\sqrt{2} k_k v_{t\alpha}} \right) = 0. \tag{1.38}$$

The basic longitudinal modes are high-frequency electron plasma oscillations with finite

electron temperature where the effect of heavy ions can be neglected. Imposing this limit, $\omega_{pi} = 0$ and asymptotic expansion of Z function for cold electrons in Eq. (1.38) leads to dispersion equation for Langmuir wave [10]:

$$\omega^2 = \omega_{pe}^2 + 3v_{te}^2 k^2. \tag{1.39}$$

This result can also be obtained from fluid theory [4].

Electrostatic waves in magnetized homogeneous plasma

Applying weak plasma fluctuation approximation to the linear Vlasov equation of electrostatic waves in the presence of a magnetic field $\mathbf{B} = B_0\hat{z}$ leads to,

$$\frac{\partial \tilde{f}_\alpha}{\partial t} + \mathbf{v}\cdot\frac{\partial \tilde{f}_\alpha}{\partial \mathbf{x}} + \frac{q_\alpha}{m_\alpha}(\mathbf{v}\times\mathbf{B})\cdot\frac{\partial \tilde{f}_\alpha}{\partial \mathbf{v}} = -\frac{q_\alpha}{m_\alpha}\tilde{\mathbf{E}}(\mathbf{x},t)\cdot\frac{\partial f_{0\alpha}}{\partial \mathbf{v}}. \tag{1.40}$$

We use the method of integration over unperturbed orbits to solve this equation and calculate the dispersion equation as follows (detailed in Appendix A):

$$1 + \sum_\alpha \left(\frac{\omega_{p\alpha}^2}{k^2 v_{t\alpha}^2}[1 + \frac{\omega}{\sqrt{2}k_z v_{t\alpha}} \sum_{m=-\infty}^{m=\infty} \exp\left(-\frac{k_y^2 v_{t\alpha}^2}{\Omega_{c\alpha}^2}\right) I_m\left(\frac{k_y^2 v_{t\alpha}^2}{\Omega_{c\alpha}^2}\right) Z\left(\frac{\omega + m\Omega_{c\alpha}}{\sqrt{2}k_z v_{t\alpha}}\right)] \right), \tag{1.41}$$

where $\Omega_{c\alpha} = eB_0/m_\alpha$ is cyclotron frequency, and I_m denotes modified Bessel function of order m. As it is clear from Eq. (1.41) and the definition of plasma dispersion function in Eq. (1.33) that the presence of magnetic field results in wave-particle interaction for different modes,

$$\omega = k_z v_z - m\Omega_{c\alpha} \qquad (m = 0, \pm 1, \pm 2, ...). \tag{1.42}$$

In the limit of $k_y = 0$ and $k = k_z$, which result in $\mathbf{k}\times\mathbf{B} = 0$, the linear dispersion relation (1.41) reduces to unmagnetized plasma dispersion relation (1.38) [8].

1.3.2 Electrostatic waves in inhomogeneous plasma

Under laboratory conditions, the complete homogeneity of a confined plasma cannot be achieved. Due to gradients of density, temperature, pressure, magnetic field strength, particle drift, or plasma current will exist in plasma. These gradients support drift waves, and then the kinetic energy of these drifts can be transferred to the waves.

In this thesis, I consider and analyze the linear theory of density gradient, which drives modes. The drift wave propagates mainly perpendicular to both the magnetic field and gradient. In this subsection, I examine the drift wave originating from a density gradient in partially magnetized plasma from the fluid approach through its set of Eqs. (1.1-1.6). Partially magnetized plasma means that there is an external magnetic field that affects just only electrons, not ions. The main reason for this assumption is that the ion Larmore

radius is typically larger than the system size $\rho_i >> L$ while electron Larmore radius is $\rho_e << L$ and also, the ion cyclotron frequency is lower than the oscillation frequency $\Omega_{ci} << \omega << \Omega_{ce}$. Here L is the device length and $\rho_\alpha = \sqrt{T_\alpha/m_\alpha\Omega_{c_\alpha}^2}$ is Larmor radius of charged particle type α. When the plasma density is inhomogeneous across magnetic

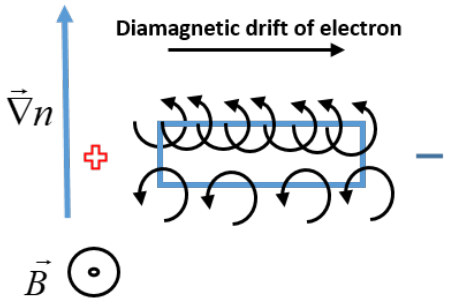

Figure 1.2: The density gradient causes the electrons to drift causing the diamagnetic current.

field, the magnetically confined electrons are affected by the $\mathbf{v}_E = (\tilde{\mathbf{E}}\times\mathbf{B})/B_0^2$ drift where magnetic field is $\mathbf{B} = B_0\hat{z}$. The physical mechanism of this drift is shown in Fig. (1.2). Consider a plasma with the gradient of density toward up; I have drawn a cartoon of the orbits of electrons gyrating in a magnetic field. Through any fixed volume element, the superposition of electron motion to right and left leads to a net drift of electrons toward right due to region of higher density, which is called diamagnetic drift.

$$\mathbf{v}_n = -\frac{T_e\nabla n_{0e}\times\mathbf{B}}{q_\alpha n_0 B_0^2} \tag{1.43}$$

The response of electrons and ions to the density gradient, drift them into the opposite directions and produce the diamagnetic current and the polarised electric field $\tilde{\mathbf{E}}$ [4].

In the following, the peculiar eigenmode of this partially magnetized plasma can be obtained. We start from the continuity equation,

$$\frac{\partial\tilde{n}_e}{\partial t} + \mathbf{v}_E\cdot\nabla n_{0e} = 0. \tag{1.44}$$

The density gradient is introduced by linearizing the density profile around the density of reference n_0. The density is written as

$$n_{0e} = n_0\left(1+\frac{x}{L_n}\right), \tag{1.45}$$

where L_n is the gradient length defined by $L_n^{-1} = dn_{0e}/n_0dx$, which gives

$$\omega\tilde{n}_e - \frac{k_y\tilde{\phi}n_0}{B_0L_n} = 0. \tag{1.46}$$

We have the following continuity equation and the equation of motion for the cold ions

that are unmagnetized:

$$\frac{\partial \tilde{n}_i}{\partial t} + n_0 \nabla \cdot \tilde{\mathbf{v}}_i = 0,$$
$$\frac{\partial \tilde{\mathbf{v}}_i}{\partial t} = -\frac{e}{m_i} \nabla \tilde{\phi}, \tag{1.47}$$

which gives

$$\tilde{n}_i = n_0 \frac{k^2 e \tilde{\phi}}{\omega^2 m_i}. \tag{1.48}$$

Dispersion relation of this "anti-drift waves" can be obtained by applying the quasi-neutrality $\tilde{n}_i = \tilde{n}_e$ assumption

$$\omega = \frac{k^2 c_s^2}{k_y v_n}, \tag{1.49}$$

here diamagnetic drift is shown by $\mathbf{v}_n = \left| T_e/(eB_0 L_n) \right| \ \hat{y}$ [11].

Chapter 2

Electron cyclotron drift instability (ECDI)

2.1 Analytical description of ECDI

Plasma instabilities are the normal modes of a system whose amplitudes grow in space or time. Electrostatic plasma instabilities can be excited by the drifting of the electrons with respect to the ions in the direction perpendicular to a magnetic field. The source of this drift can be a gradient in density or the $\mathbf{E} \times \mathbf{B}$ drift in the case of Hall-effect thrusters. Linear theory can describe relatively weak plasma fluctuations, but it cannot describe the final fate of plasma instabilities; therefore, nonlinear theories and computer simulations are used to describe the final stage of plasma instabilities.

In this and the next chapters, I present a linear theory of electron cyclotron drift instability and lower-hybrid drift instability and then analyze their dispersion relation with typical parameters relevant to Hall thrusters.

The electron cyclotron drift instability, as exists in partially magnetized cross-field plasma, is driven by the significant $\mathbf{E} \times \mathbf{B}$ drift of electrons relative to ions. Theoretical study of ECDI through its linear dispersion relation reveals many of its features. In this respect, we consider electrostatic waves with initial electron drift velocity $\mathbf{v}_E = E_0/B_0\ \hat{y}$ across a uniform magnetic field. Since the effect of the magnetic field on ions is neglected, we use the susceptibility of the electrostatic wave in unmagnetized homogeneous plasma for ions Eq. (1.38) and the susceptibility of the electrostatic wave in magnetized homogeneous plasma with initial uniform electric $\mathbf{E} = -E_0\hat{x}$ for electrons Eq. (1.41). Therefore, 2-dimensional linear dispersion relation of ECDI from Eq. (1.38) has the form of:

$$1 + K_i(\mathbf{k}, \omega) + K_e(\mathbf{k}, \omega) = 0, \tag{2.1}$$

$$K_i(\mathbf{k},\omega) = -\frac{k_i^2}{2k^2} Z'\left(\frac{\omega}{\sqrt{2}kv_{ti}}\right), \tag{2.2}$$

$$K_e(\mathbf{k},\omega) = \frac{k_e^2}{k^2}\left[1 + \frac{(\omega - k_y v_E)}{\sqrt{2}k_z v_{te}} \sum_{m=-\infty}^{m=\infty} \exp\left(-\frac{k_y^2 v_{te}^2}{\Omega_{ce}^2}\right) I_m\left(\frac{k_y^2 v_{te}^2}{\Omega_{ce}^2}\right) Z\left(\frac{\omega - k_y v_E + m\Omega_{ce}}{\sqrt{2}k_z v_{te}}\right)\right], \tag{2.3}$$

where $k_i = \omega_{pi}/v_{ti}$ and $k_e = \omega_{pe}/v_{te}$. In the limit of the cold ions where $\omega > k_z v_{ti}$, the asymptotic series of plasma dispersion function becomes

$$if\ \ |\zeta| >> 1\ \Rightarrow Z(\zeta) = \frac{-1}{\zeta} - \frac{1}{2\zeta^3}. \tag{2.4}$$

Therefore we have

$$K_i(\mathbf{k},\omega) = -\frac{k_i^2}{2k^2} Z'\left(\frac{\omega}{\sqrt{2}kv_{ti}}\right) = \frac{2k_i^2}{2k^2}\left[1 + \frac{\omega}{\sqrt{2}kv_{ti}} Z\left(\frac{\omega}{\sqrt{2}kv_{ti}}\right)\right],$$

$$= \frac{k_i^2}{k^2}\left[1 + \frac{\omega}{\sqrt{2}kv_{ti}}\left[\frac{-\sqrt{2}kv_{ti}}{\omega} - \frac{1}{2}\left(\frac{\sqrt{2}kv_{ti}}{\omega}\right)^3\right]\right] = \frac{k_i^2}{k^2}\left[-\left(\frac{kv_{ti}}{\omega}\right)^2\right] = -\frac{\omega_{pi}^2}{\omega^2}. \tag{2.5}$$

and the ion susceptibility becomes

$$K_i(\mathbf{k},\omega) = -\frac{\omega_{pi}^2}{\omega^2}. \tag{2.6}$$

2.2 Numerical solution

In this section, I present the general behavior of the growth rate and frequency of 2D-ECDI by solving the dispersion relation of Eq. (2.1) in Python numerically using the technique described in Ref.[12]. The solution is calculated by a fixed point iteration using the relative error as a stopping condition. This solver uses the convergence condition that $|1 - \omega_{i+1}/\omega_i| < 10^{-6}$ for $i \geq 15$. The SciPy.special Faddeeva function is used to get good numerical accuracy of the plasma dispersion function for a wide range of arguments.

In the case of the cold ions where $T_e >> T_i$, the general dispersion equation of ECDI consists of three main instabilities: ion-acoustic, modified two-stream, and electron cyclotron drift instabilities [13]. In this section I examine each of them.

2.2.1 Ion-acoustic instability(IAI)

Fig. (2.1) represents the growth rate and frequency of the ion-acoustic instability as a function of $k_y\rho_e$ for different values of v_E/v_{te}. The ratio of k_z/k_y is constant for each curve. Three distinct zones for each curve are distinguishable, $k_y\rho_e < 1$, $1 < k_y\rho_e \leq 4$ and $k_y\rho_e > 4$. According to Gary [14] at $k_y\rho_e > 4$ the ion acoustic instability behaves

like the zero magnetic field case. It is clear more in the frequency plot where all curves fall on the blue dash-line with constant slope which is related to the magnetic field free frequency of ion acoustic wave, i.e. $\omega = k_y c_s/(1 + k^2\lambda_D^2)^{1/2}$.

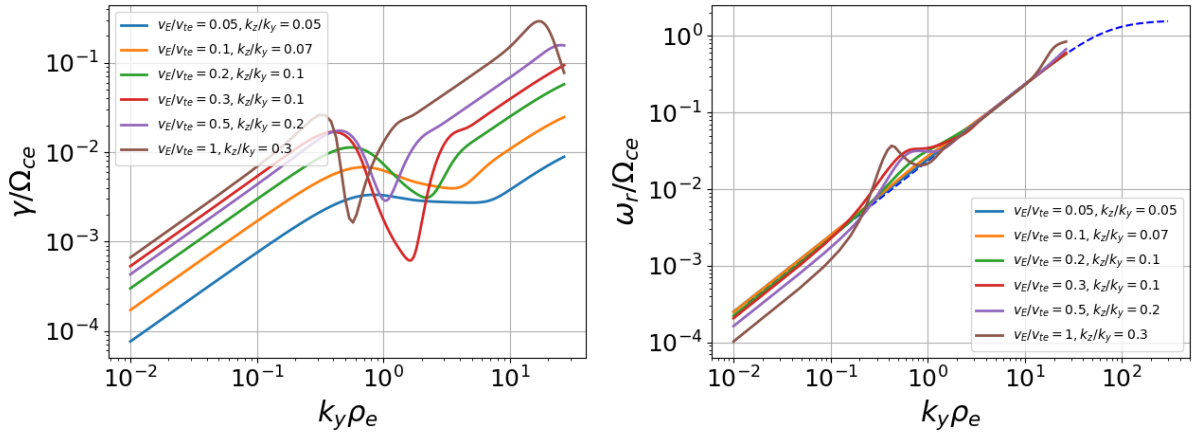

(a) **(b)**

Figure 2.1: (a) Growth rate and (b) frequency of the ion-acoustic instability as a function of $k_y\rho_e$ for the following parameters:, $\omega_{pe}/\Omega_{ce} = 68$, $m_i/m_e = 1836$, $T_e = 1$ eV, $T_i = 0$ eV, and $n = 1 \times 10^{17}$ m^{-3}. The value of k_z/k_y for the curve with v_E/v_{te} labelling with 0.05, 0.1, 0.2, 0.3, 0.5, and 1 is 0.05, 0.07, 0.1, 0.1, 0.2, and 0.3 respectively.

Figure (2.1a) depicts an increase in growth rate γ for $k_y\rho_e < 1$ where the magnetic field is strong and then transits into field-free case as $k_y\rho_e$ increases. The point is that as k_z/k_y decreases, the ion-acoustic instability changes from dissipative mode driven by the pole resonances $\omega - k_y v_E - m\Omega_{ce} - k_z v_z$ to the reactive instability due to coupling of the sound wave and the Doppler-shifted Bernstein wave instability [13].

2.2.2 Modified two-stream instability(MTSI)

In the case of low frequency where $\omega - k_y v_E << \Omega_{ce}$, we only consider the $m = 0$ term of the infinite sum of Eq. (2.1) with the cold ion. Assuming $k_y\rho_e << 1$, the asymptotic series of the plasma dispersion function Z, results in:

$$1 + \frac{\omega_{pe}^2}{\Omega_{ce}^2} - \frac{k_z^2}{k_y^2}\frac{\omega_{pe}^2}{(\omega - k_y v_E)^2} - \frac{\omega_{pi}^2}{\omega^2} = 0. \tag{2.7}$$

This dispersion relation shows the reactive nature of the MTSI mode. In this case of the cold plasma, the instability occurs due to the coupling of the lower-hybrid mode (the second and last terms) with the beam mode $\omega = k_y v_E$. Note that for the reactive instabilities, the algebraic dispersion equations with real coefficients produce the complex conjugate solutions; one of this is an unstable mode. Figure (2.2) shows growth rate and frequency of modified two-stream instability versus k_z/k_y for different v_E/v_{te} and $k_y\rho_e$

as found from general dispersion equation. It can be seen from Fig. (2.2) that as k_z/k_y

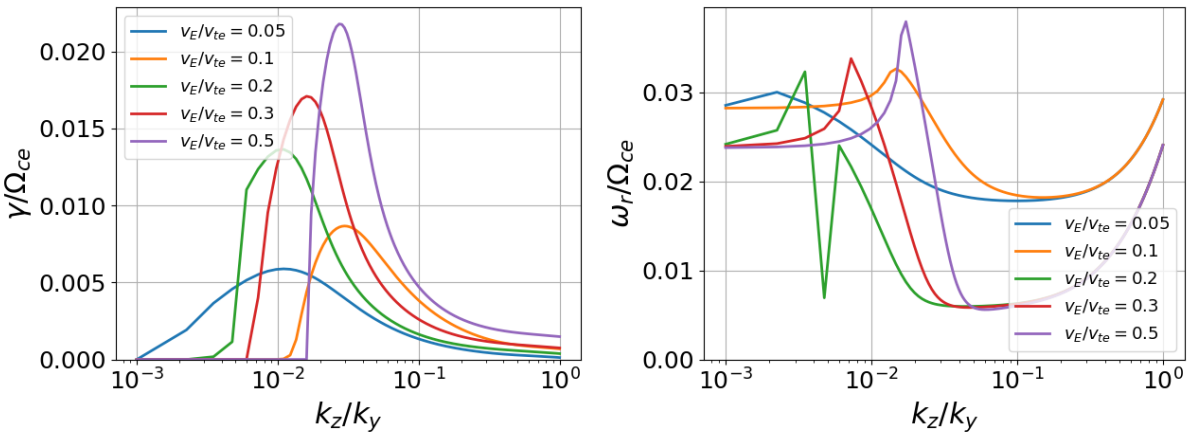

Figure 2.2: (a) Growth rate and (b) frequency of the modified two stream instability as a function of k_z/k_y for parameters used in the solver, $\omega_{pe}/\Omega_{ce} = 68$, $m_i/m_e = 1836$, $T_e = 1$ eV, $T_i = 0$ eV, and $n = 1 \times 10^{17}$ m^{-3}. The value of $k_y\rho_e = 0.75$ is used for the curve with $v_E/v_{te} = 0.05,\ 0.1$, and for the curves with label $v_E/v_{te} = 0.2,\ 0.3,\ 0.5$ the $k_y\rho_e = 0.25$ is used.

increases, the instability transits from modified two-stream instability to ion-acoustic instability. In the frequency figure, the curves that have the same value for $k_y\rho_e$ merge to the same value of frequency that corresponds to the ion-acoustic frequency given by Eq. (2.7) as k_z/k_y increases. The numerical results of Figs. (2.1 and 2.2) have a good consistency with the results of Ref. [13].

2.2.3 Electron cyclotron drift instabilities (ECDI)

The electron cyclotron drift instability occurs as k_z/k_y is reduced more. The numeric solution of dispersion relation (2.1) in Fig. (6) of Ref. [13] shows that the maximum growth rate happens when the wave vector is entirely perpendicular to the magnetic field and the $k_z = 0$.

Here I focus on investigating the growth rate and frequency of this instability for several fixed values of the k_z for two cases of the electron temperature $T_e = 10$ eV and $T_e = 25$ eV. The other parameters used for numerical solutions are mentioned in Table (2.1):

Table 2.1: Typical parameters used to find the roots of ECDI dispersion relation for $T_e = 10$ eV.

Variable	B_0	E_0	n	T_e	T_i	$k_0\lambda_D$	m_i
Value	0.02 T	2 kV/m	$10^{17}\mathrm{m}^{-3}$	10 eV	0.0 eV	0.261	xenon

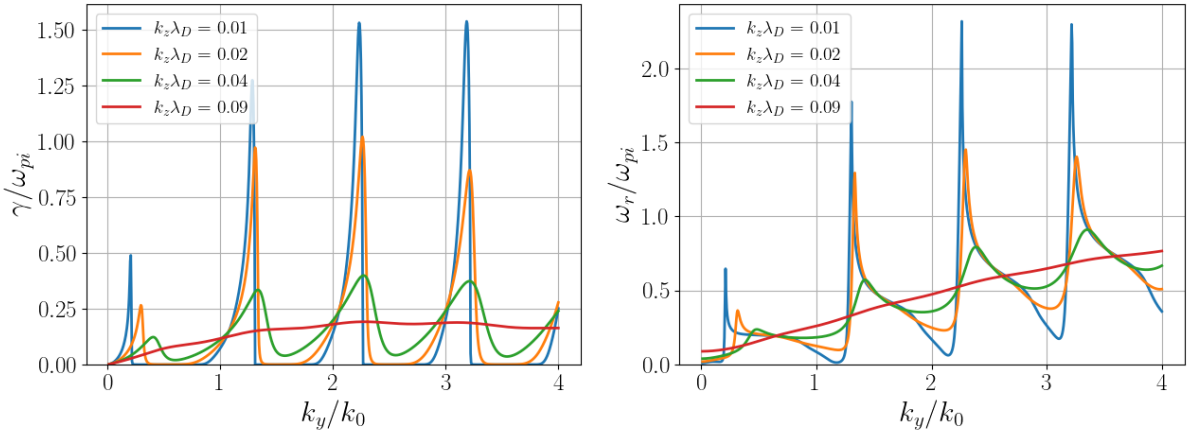

(a) **(b)**

Figure 2.3: (a) Growth rate and (b) frequency of instability of four roots for various $k_z\lambda_D = 0.01,\ 0.02,\ 0.04,\ 0.09$ respectively, found from the full dispersion equation of ECDI, Eq.(2.1). Parameters for these figures are: $T_e = 10$ eV, $k_0\lambda_D = 0.261$, $v_E = -370c_s$, $v_{te} = 960c_s$, $\Omega_{ce} = 96.5\omega_{pi}$, $k_0 = \Omega_{ce}/v_E$.

As can be seen from Fig. (2.3), the first root on the left corresponds to the modified two-stream instability MTSI ($m = 0$), and subsequent roots which are from $m = 1, 2, 3, ...$ are ECDI resonances. For investigating the effect of temperature, I increase the temperature from $T_e = 10$ eV to $T_e = 25$ eV in Fig. (2.4).

For small values of the k_z, one can see in Figs. (2.3 and 2.4) the instability peaks near the resonant values of $k_y = mk_0$. For larger values of k_z, as shown in Fig. (2.1) and based on the result of some studies like Ref. [14], the resonance is broadened, resulting in the smooth curve corresponding to the kinetic resonance instability of the ion-acoustic in unmagnetized plasma.

Comparing the growth rate results of Fig. (2.3) with Fig. (2.4) shows that for $T_e = 10$ eV by increasing k_y, the instabilities increase and peak at mode $m = 3$ with maximum growth rate $\gamma = 1.52\ \omega_{pi}$, while by increasing temperature to $T_e = 25$ eV in Fig. (2.4) instabilities reduce by increasing k_y and maximum growth rate occurs at mode $m = 1$ with maximum growth rate $\gamma = 1.175\ \omega_{pi}$.

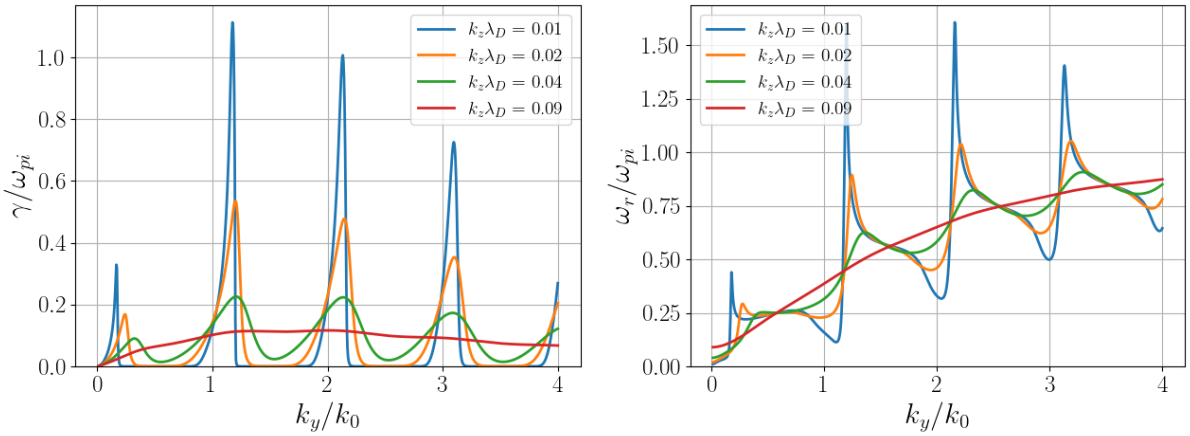

(a) **(b)**

Figure 2.4: (a) Growth rate and (b) frequency of instability of four roots for various $k_z\lambda_D = 0.01,\ 0.02,\ 0.04,\ 0.09$ respectively, found from the full dispersion equation of ECDI. Parameters for these figures are: $T_e = 25$ eV, $k_0\lambda_D = 0.261$, $v_E = -370c_s$, $v_{te} = 960c_s$, $\Omega_{ce} = 96.5\omega_{pi}$, $k_0 = \Omega_{ce}/v_E$.

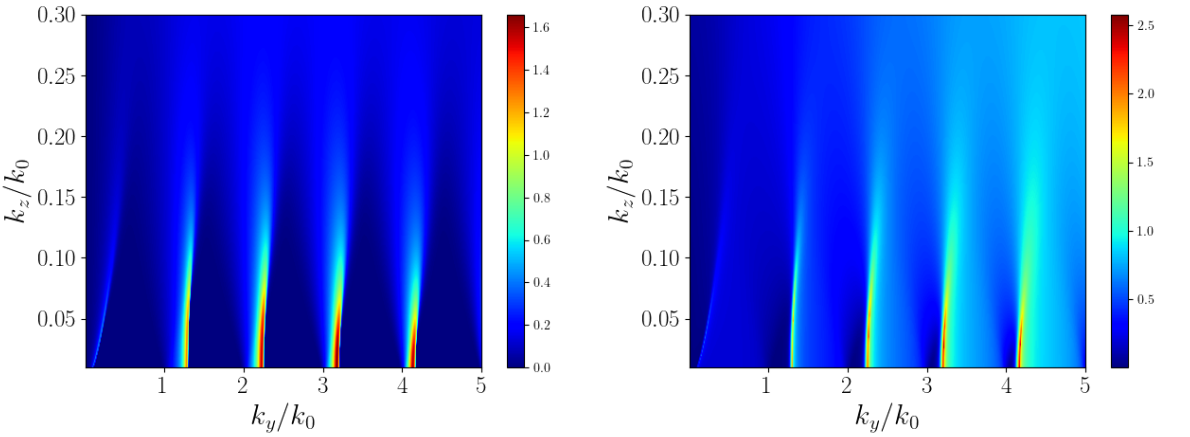

(a) **(b)**

Figure 2.5: Color plot of (a) growth rate $\gamma(k_z, k_y)/\omega_{pi}$ and (b) frequency $\omega(k_z, k_y)/\omega_{pi}$ for the general form of dispersion relation. Parameters for these figures are: $T_e = 10$ eV, $k_0\lambda_D = 0.261$, $v_E = 370c_s$, $v_{te} = 960c_s$, $\Omega_{ce} = 96.5\omega_{pi}$, $k_0 = \Omega_{ce}/v_E$.

A notable point from Fig. (2.5) is the existence of modified two-stream instability (MTSI) in the sub cyclotron low-k region. Increasing k_z changes the instability to the ion-acoustic regime, since the values of eigenfrequencies of the ion-acoustic modes are much smaller; they are not visible on this color graph.

Figure (2.6) highlights that for the large magnitude of absolute k, the growth rate disappears. Furthermore, the maximum growth rate occurs when the angle α that is the

angle between k and k_y, is less than $\pi/4$.

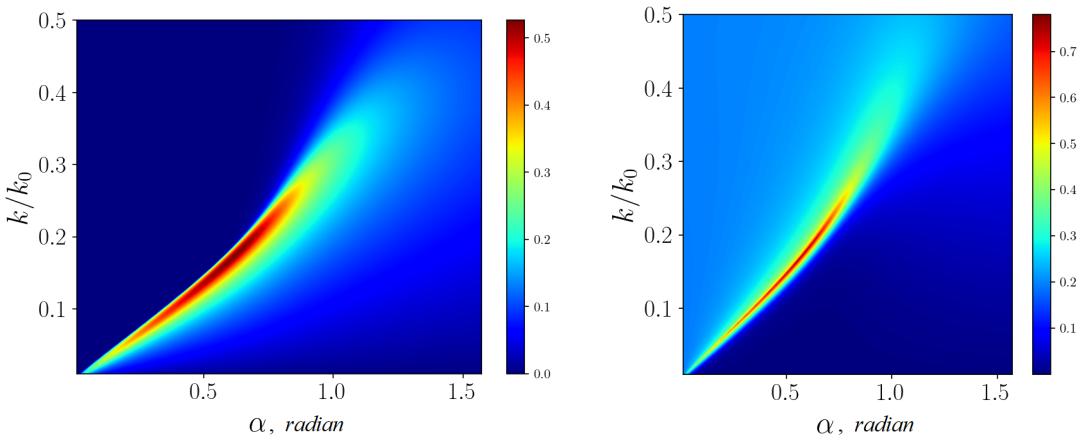

(a) **(b)**

Figure 2.6: (a) Close-up of the full dispersion relation growth rate γ/ω_{pi} and (b) frequency ω/ω_{pi} given as a function of α and k/k_0. α changes from 0.01 to $\pi/2$ radians. Parameters for these figures are: $T_e = 10$ eV, $k_0\lambda_D = 0.261$, $v_E = 370c_s$, $v_{te} = 960c_s$, $\Omega_{ce} = 96.5\omega_{pi}$, $k_0 = \Omega_{ce}/v_E$.

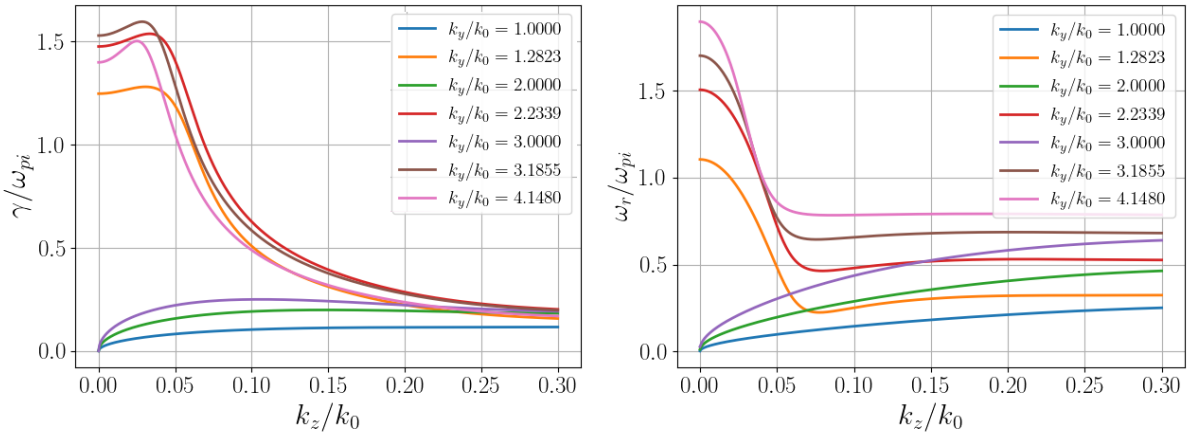

(a) **(b)**

Figure 2.7: (a) Growth rate and (b) frequency of instability for various k_y. Parameters for these figures are: $T_e = 10$ eV, $k_0\lambda_D = 0.261$, $v_E = 370c_s$, $v_{te} = 960c_s$, $\Omega_{ce} = 96.5\omega_{pi}$, $k_0 = \Omega_{ce}/v_E$.

Figure (2.7) illustrates the growth rate and frequency of instability as a function of k_z for a various fixed values of k_y. Here, I select two groups of azimuthal wavevector which correspond to the original high and low growth rate of Fig. (2.5). As can be seen, both groups show a similar pattern with the original case in the color plot. They also show

different behavior because of localized value. In addition, it can be seen that by increasing k_z, the instability changes to ion-acoustic.

2.3 General dispersion relation with density gradient

The gradient in the equilibrium parameters leads to diamagnetic drifts that allows the propagation of drift waves. Other instabilities may arise from gradients and may interact with ECDI. In this section I study the general case of the electrostatic waves and instabilities propagating perpendicularly to the magnetic field (including ECDI) and excited due to the gradients of density, magnetic field, or temperature. The more general form of Eq. (2.1) with considering the effect of temperature, density, and magnetic field gradients is as follows [15]:

$$1 + K_i + K_e = 0, \tag{2.8}$$

$$K_i(\mathbf{k}, \omega) = -\frac{\omega_{pi}^2}{2k^2 v_{ti}^2} Z' \left(\frac{\omega}{\sqrt{2} k v_{ti}} \right), \tag{2.9}$$

$$K_e(\mathbf{k}, \omega) = \frac{k_e^2}{k^2} \left[1 + \frac{i(\omega - k_y v_d + 2k_y v_T)}{\Omega_{ce}} G(\mu, \lambda) - \frac{i k_y v_T}{\Omega_{ce}} \left(\frac{\partial G}{\partial \mu} - \frac{\partial G}{\partial \lambda} \right) \right]_{\mu,\lambda=1}, \tag{2.10}$$

where

$$G(\mu, \lambda) = \int_0^\infty \frac{d\tau \exp\{i\omega' \tau - \frac{1}{2}\mu k_z^2 \rho_e^2 \tau^2 + (k_y^2 + k_x^2)\rho_e^2 (\cos\tau - 1)/(\lambda + i k_y \bar{v}_B \tau/\omega_{ce})\}}{\lambda + i k_y \bar{v}_B \tau / \Omega_{ce}}. \tag{2.11}$$

The integral $G(1,1)$ is the Gordeyev integral (Gordeyev, 1952), and $\omega' = (\omega - k_y v_E)/\Omega_{ce}$, $v_n = -v_{te}^2/\Omega_{ce} L_n$, $v_T = -v_{te}^2/\Omega_{ce} L_T$ are drift velocities caused by density and temperature gradient respectively. The average ∇B drift velocity is $\bar{v}_B = -v_e^2/\Omega_{ce} L_B$, and $v_d = v_E + v_n + v_T$ is the net drift velocity, here $L_{(n,T,B)}$ are the gradient lengths defined by $L_{(n,T,B)} = (d(n,T,B)/(n,T,B)_0 dx)^{-1}$. Now, we let $v_B = 0$ or $v_T = 0$ and see the influence of ∇n drift velocity on the characteristics of the instability.

2.4 Density gradient effect

Considering the density gradient effect only in dispersion relation in the limit of cold ions yields:

$$1 - \frac{\omega_{pi}^2}{\omega^2} + \frac{k_e^2}{k^2} \left[1 + \frac{i(\omega - k_y v_E - k_y v_n)}{\Omega_{ce}} G(1,1) \right] = 0. \tag{2.12}$$

Here $G(1,1)$ is Gordeyev integral,

$$G(1,1) = \int_0^\infty d\tau \exp\left[i\frac{\omega - k_y v_E}{\Omega_{ce}}\tau - \frac{1}{2}(k_z^2\rho_e^2)\tau^2 + ((k_x^2+k_y^2)\rho_e^2)(\cos\tau - 1)\right]$$
$$= \frac{-i}{\sqrt{2(k_z^2\rho_e^2)}} e^{-(k_x^2+k_y^2)\rho_e^2} \sum_{m=-\infty}^{+\infty} Z\left(\frac{\frac{\omega - k_y v_E}{\Omega_{ce}} - m}{\sqrt{2(k_z^2\rho_e^2)}}\right) I_m((k_x^2+k_y^2)\rho_e^2). \tag{2.13}$$

An alternative way of writing this dispersion equation based on the Gordeyev function, which is used in the solver, can be:

$$1 + k^2\lambda_D^2 + g_{\nabla n}\left(\frac{\omega - k_y v_E}{\Omega_{ce}}, \frac{k_y v_n}{\Omega_{ce}}, (k_x^2+k_y^2)\rho_e^2, k_z^2\rho_e^2\right) - \frac{k^2\lambda_D^2\omega_{pi}^2}{\omega^2} = 0, \tag{2.14}$$

where Gordeyev function is related to Gordeyev integral as follows:

$$g_{\nabla n}\left(\frac{\omega - k_y v_E}{\Omega_{ce}}, \frac{k_y v_n}{\Omega_{ce}}, (k_x^2+k_y^2)\rho_e^2, k_z^2\rho_e^2\right) = i\left(\frac{\omega - k_y v_E}{\Omega_{ce}} - \frac{k_y v_n}{\Omega_{ce}}\right) G(1,1)$$
$$= \left(\frac{\omega - k_y v_E - k_y v_n}{\Omega_{ce}}\right) \frac{1}{\sqrt{2(k_z^2\rho_e^2)}} e^{-(k_x^2+k_y^2)\rho_e^2} \sum_{m=-\infty}^{+\infty} Z\left(\frac{\frac{\omega - k_y v_E}{\Omega_{ce}} - m}{\sqrt{2(k_z^2\rho_e^2)}}\right) I_m((k_x^2+k_y^2)\rho_e^2). \tag{2.15}$$

2.4.1 Numerical solution of dispersion relation with density gradient

The typical numerical solution of Eq. (2.14) in the case of the cold ions with $k_x = 0$ is shown in Figs. (2.8-2.10) which displays the growth rates and frequencies as a function of $k_y v_E/\Omega_{ce}$ for different characteristic lengths of the density gradient. These numerical solutions are done using Python solver that is used in Ref. [12] and I modify its Gordeyev function to include gradient effect. Since the maximum growth rate occurs in lower k_z, I focus on investigating the effect of different density gradient lengths on instability in the low k_z region. The parameters used for these numerical solutions are given in Table (2.2).

Table 2.2: Typical Hall thruster parameters used in the solver to find roots of ECDI dispersion relation with the effect of density gradient.

Variable	B_0	E_0	n	T_e	T_i	m_i
Value	0.02 T	20 kV/m	10^{17} m^{-3}	10 eV	0.0 eV	xenon

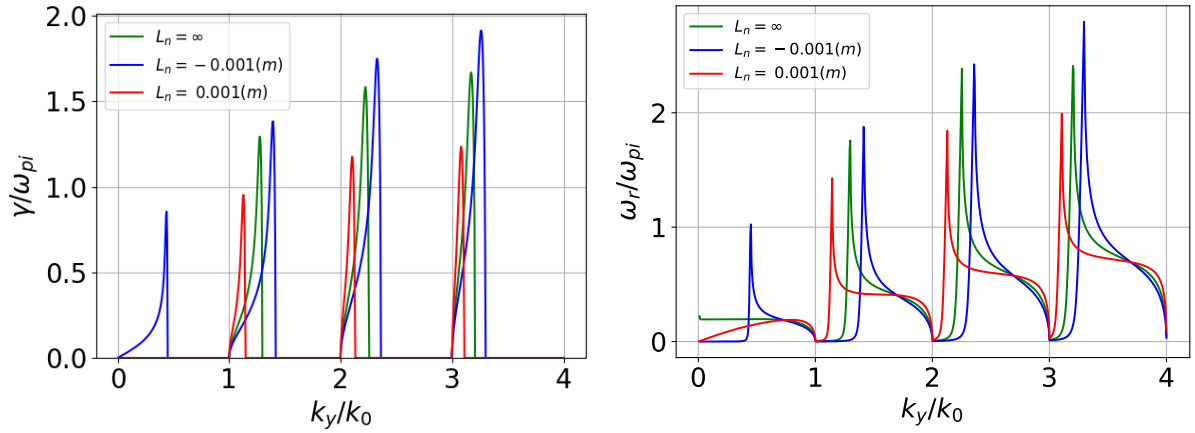

(a) **(b)**

Figure 2.8: (a) Growth rate and (b) frequency of instabilities with considering the effect of the density gradient drift on the dispersion relation ($k_z\lambda_D = 0.00001$), blue line represents growth rate for $L_n = -0.001$ m and red line is the growth rate for $L_n = 0.001$ m and green line is growth rate without density gradient drift, here $k_0 = \Omega_{ce}/v_E$ and $v_E = E_0/B_0$.

Figure (2.8) shows that density gradient drift in a negative direction causes the growth rate in the lowest mode. For the higher subsequent roots, negative gradient length increases the peak of growth rate compared to the case without gradient effect (green line), while positive gradient length decreases growth rate. Also, the lobes of negative gradient length are slightly thicker than the curves without the density gradient and positive gradient length.

According to the data from different thrusters studies of thrusters [16, 17, 18] the plasma density profile can be approximated by the exponential, and the characteristic gradient length should be varied between $0.01 - 0.0005$ m, therefore in this part, I compare the effect of different gradient lengths on the instability.

As we can see from Fig. (2.9), the lobes corresponding to the typical density gradient in the thruster $L_n = -0.01$ m superimpose perfectly on those obtained without any gradient. In addition, with increasing subsequent roots, the value of the growth rate increases. For the forth cyclotron mode, strong gradient length $L_n = -0.0005$ m shows maximum growth rate at $2\omega_{pi}$ and its lobes are slightly thicker than the others and expands unstable region to the lower azimuthal wavelength. It is worth mentioning that gradient length with different values has a significant effect on the lowest mode compare with the case without it, and the highest growth rate in lowest roots belongs to the gradient length $L_n = -0.001$ m.

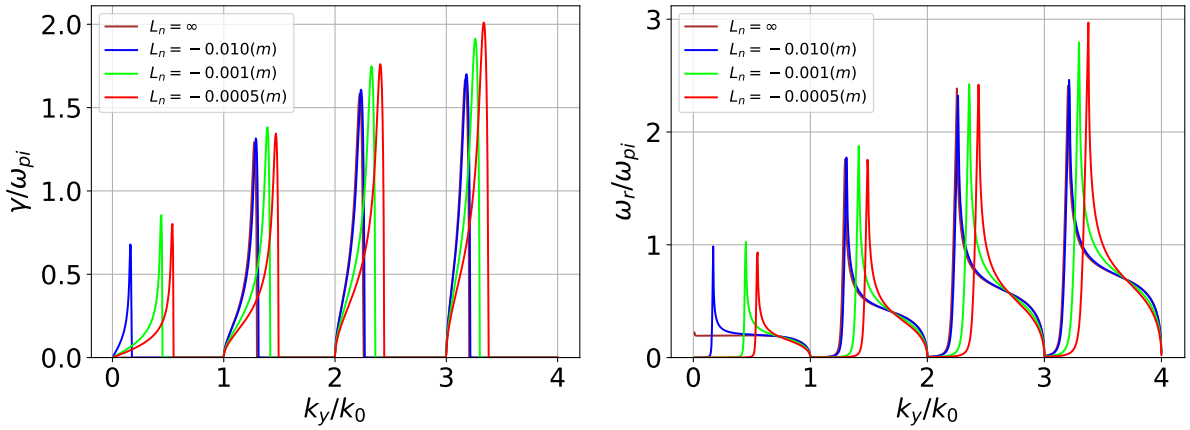

(a) **(b)**

Figure 2.9: (a) Growth rate and (b) frequency of instabilities with considering the effect of the density gradient drift with different gradient lengths. ($k_z\lambda_D = 0.00001$) and gradient length are $L_n = -0.0005,\ -0.001,\ -0.01$ m, here $k_0 = \Omega_{ce}/v_E$.

For investigating the effect of electric field on growth rate and frequency of instability, I double the value of electric field strength.

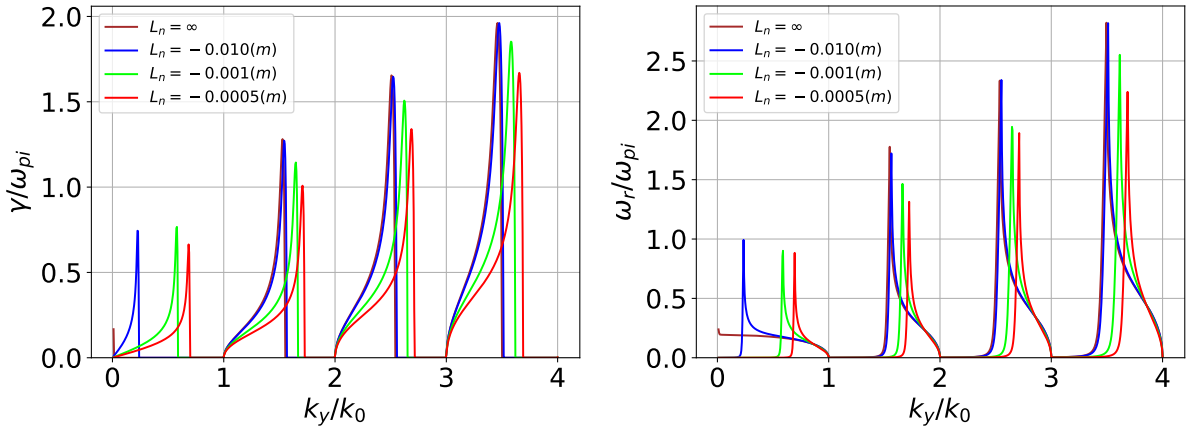

(a) **(b)**

Figure 2.10: (a) Growth rate and (b) frequency of instabilities with considering the effect of the density gradient drift with different gradient lengths. ($k_z\lambda_D = 0.00001$) and gradient length are $L_n = -0.0005,\ -0.001,\ -0.01$ m, here $k_0 = \Omega_{ce}/v_E$ and electric field $E_0 = 40000$ V/m.

Figure (2.10) shows that increasing the value of the electric field twice decreases the growth rate of gradient length of $L_n = -0.001, -0.0005$ m while increases the growth rate of $L_n = -0.01$ m and the ones obtained without any gradient. In general, it broadens all lobes and expands the unstable region to the lower wavelength. Moreover, based on

our observation, by increasing the electric field from 100 V/m to 40000 V/m in the same domain of k_y, the number of cyclotron modes increases.

In this part I restore k_z to study the effects of the wavevector parallel to the magnetic field. Therefore I focus on investigating the behavior of the growth rate and frequency of this instability for several fixed values of the k_z with a fixed gradient length of $L_n = -0.001$ m.

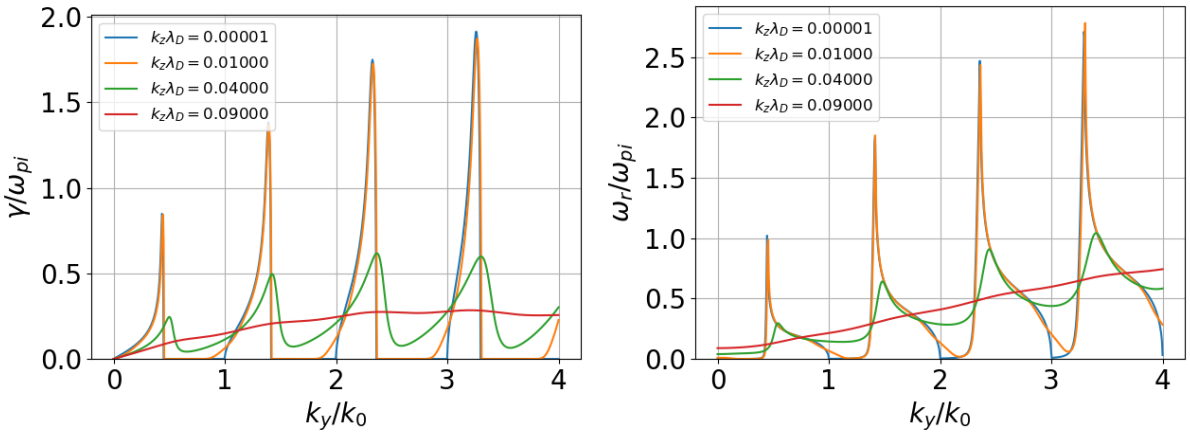

(a) **(b)**

Figure 2.11: (a) Growth rate and (b) frequency of instabilities with considering the effect of the density gradient drift with various $k_z\lambda_D = 0.00001, 0.01, 0.04, 0.09$. Gradient length is $L_n = -0.001$ m, here $k_0 = \Omega_{ce}/v_E$, other parameters for these figures are mentioned in Table (2.2).

Figure (2.11) displays that for small values of the k_z, unstable wavenumbers form in azimuthal direction y and growth rate peaks near the resonant values of $k_y = mk_0$. Moreover, The first root from the left is the lower-hybrid drift instability ($m = 0$), and subsequent roots from $m = 1, 2, 3, ...$ are ECDI resonances with the effect of density gradient. It is clear that by increasing the value of k_z, resonances are broadened and result in a smooth curve corresponding to the ion-acoustic instability.

In this part I solve three-dimensional dispersion relation (2.14) for variety fixed values of k_z and show eigenfrequencies in the $k_x - k_y$ plane. Parameters for the following plots are shown in Table (2.2).

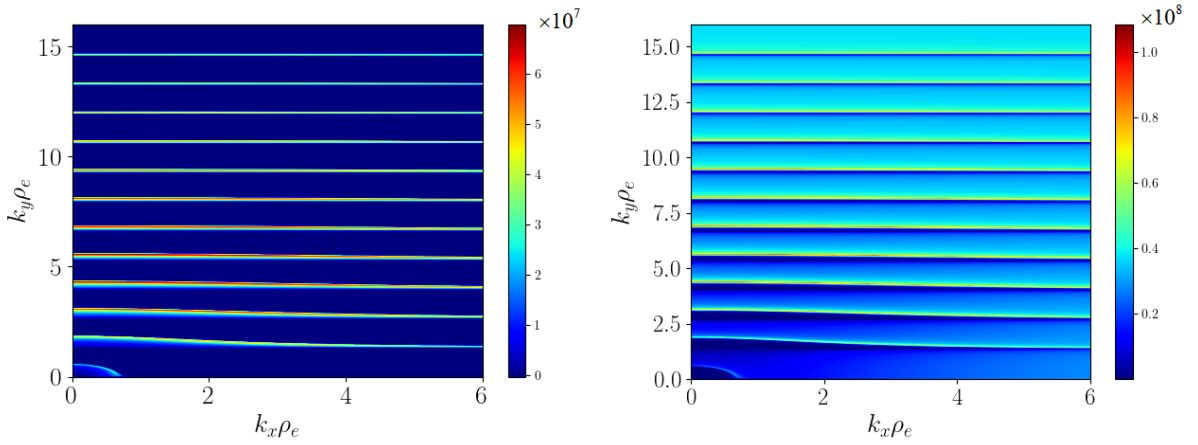

(a) **(b)**

Figure 2.12: Color plot of (a) growth rate $\gamma(k_x, k_y)$ and (b) frequency $\omega(k_x, k_y)$ for the general form of dispersion relation of ECDI with the effect of gradient of density. Here $L_n = -0.001$ m, $k_z\lambda_D = 0.00001$.

Solving this three dimensional dispersion relation for fixed k_z shows a succession of unstable modes extending over a large range of $k_y\rho_e$. The first lobe ($m = 0$) in the lower left corner of Fig. (2.12), depicts lower-hybrid drift instability and others subsequent roots are for $m = 1, 2, 3, .., 11$ of ECDI with density gradient effect.

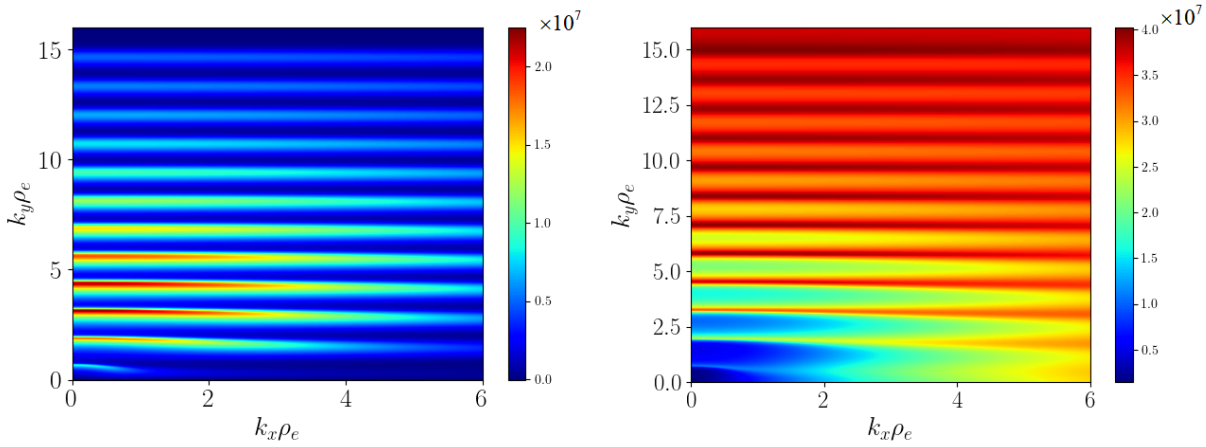

(a) **(b)**

Figure 2.13: Color plot of (a) growth rate $\gamma(k_x, k_y)$ and (b) frequency $\omega(k_x, k_y)$ for the general form of dispersion relation. Here $L_n = -0.001$ m, $k_z\lambda_D = 0.04$.

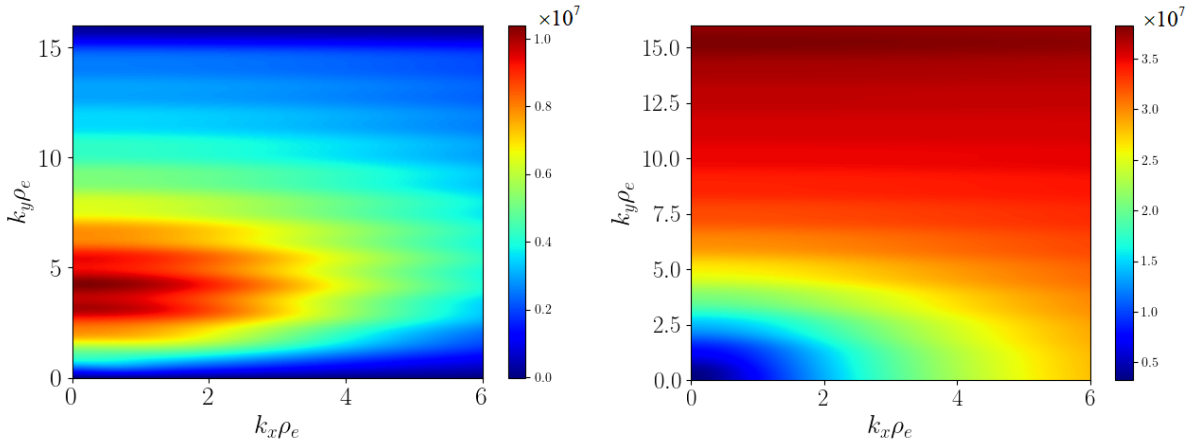

Figure 2.14: Color plot of (a) growth rate $\gamma(k_x, k_y)$ and (b) frequency $\omega(k_x, k_y)$ for the general form of dispersion relation. Here $L_n = -0.001$ m, $k_z\lambda_D = 0.09$.

Figures (2.13, 2.14) show that the presence and increase of a wave vector component parallel to the magnetic field suggests less unstable modes. Hereof, the instability disappears as soon as the component k_z increases; those remaining unstable modes merge and result in a wide area of ion-acoustic instability.

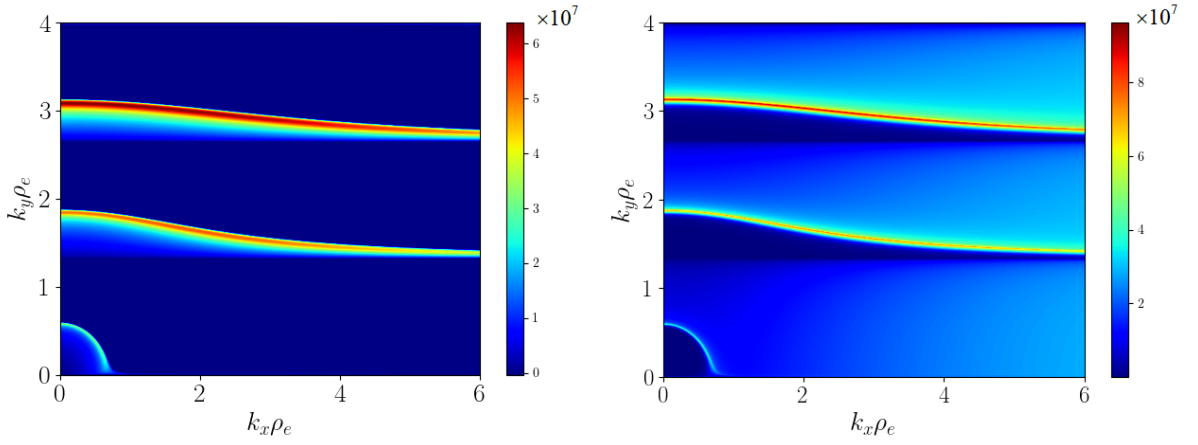

Figure 2.15: Color plot of (a) growth rate $\gamma(k_x, k_y)$ and (b) frequency $\omega(k_x, k_y)$ for the general form of dispersion relation. Here $L_n = -0.001$ m, $k_z\lambda_D = 0.00001$.

For the sake of clarity, I show three only first modes of instability. From Fig. (2.15), the evolution of the unstable modes as a function of k_x is similar for different value of k_y. Apart from the first mode, the width of the unstable region decreases very slowly for high values of k_x, and the instability persists with large growth rates for k_x close to k_y.

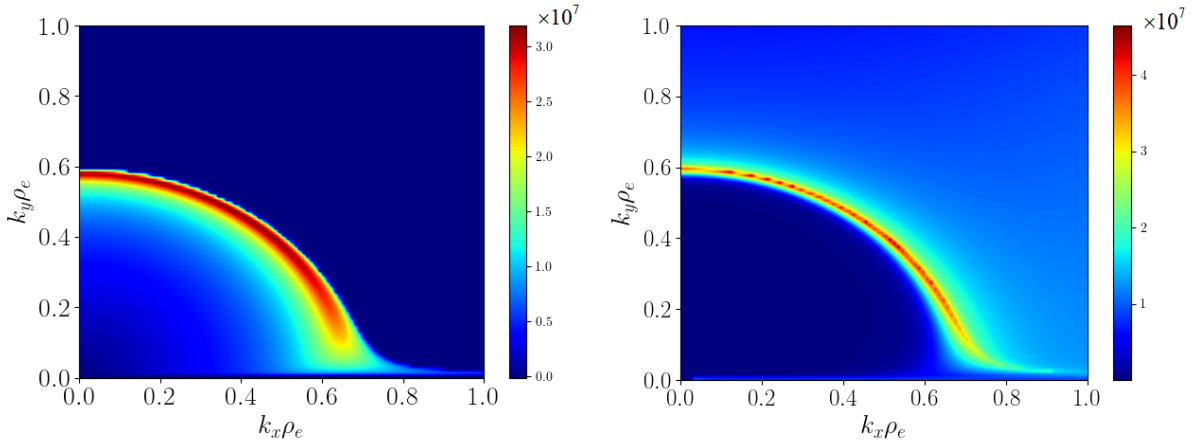

(a) **(b)**

Figure 2.16: Color plot of (a) growth rate $\gamma(k_x, k_y)$ and (b) frequency $\omega(k_x, k_y)$ for the general form of dispersion relation. Here $L_n = -0.001$ m, and $k_z\lambda_D = 0.00001$.

Previous figures show the higher modes, while in this Fig. (2.16) I focus on the first lobe of long-wavelength related to $m = 0$. We can see that the width of this unstable region decreases very fast and the darkest red area corresponding to the growth rate peak range from $k_x\rho_e = 0$ purely azimuthal unstable modes up to $k_x\rho_e = 0.6$. This value is the lowest range among others lobes.

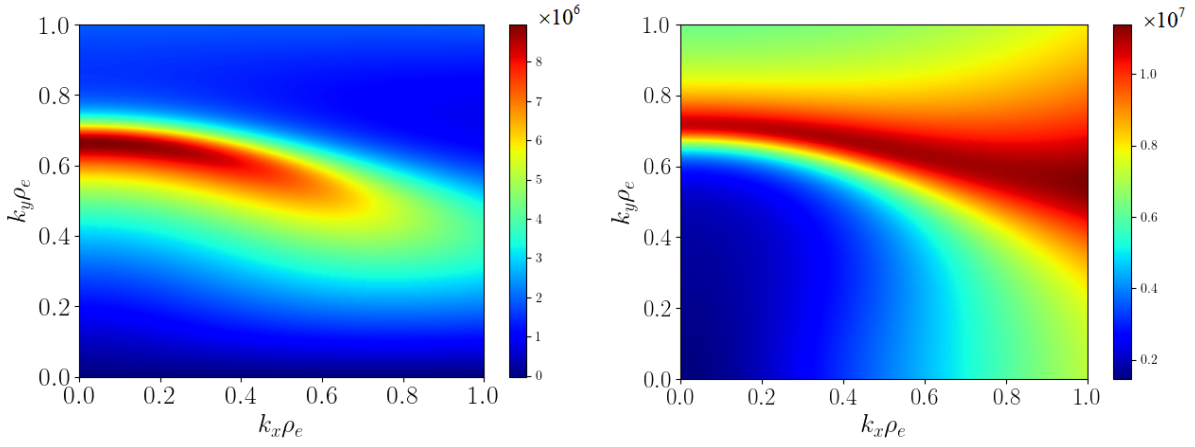

(a) **(b)**

Figure 2.17: Color plot of (a) growth rate $\gamma(k_x, k_y)$ and (b) frequency $\omega(k_x, k_y)$ for the general form of dispersion relation. Here $L_n = -0.001$ m, and $k_z\lambda_D = 0.04$.

Figure (2.17) shows that increasing wave vector along magnetic field makes the first mode becomes wider, and overlaps with higher modes.

2.5 Summary

The linear stability analysis of plasma with the system of drifting electrons in crossed electric **E** and magnetic **B** field without the effect of gradients,for the case of $T_e >> T_i$ is considered. This analysis verifies the existence of three possible instabilities: ion-acoustic, modified two-stream and electron cyclotron drift instability, that among them, for $v_E/v_{te} < 0.5$ the electron cyclotron drift modes, has the largest growth rate. For a small value of wave vector along the magnetic field, it is shown that instabilities peaks near the ECDI resonances $k_y = mk_0$ and by increasing k_z, resonances are broadened toward ion-acoustic mode.

Studying the influence of density gradient on ECDI shows that for purely azimuthal modes, instabilities grow for negative density gradient length, while the positive density gradient lengths reduce growth rates at ECDI resonances. This study also reveals that the long-wavelength mode is most strongly affected by the density gradient. Though the growth rate of this branch is weaker than higher modes, the long-wavelength mode is more difficult to stabilize and therefore is expected to be more important for transport [19]. This long-wavelength branch is related to the lower-hybrid mode and will be studied separately in the next chapter.

Chapter 3

Lower-hybrid drift instability (LHDI)

The numerical solutions of Eq. (2.14) in Figs. (2.8, 2.10) reveals that density gradient has a distinct effect on the first mode of cyclotron harmonics of ECDI dispersion relation, and it causes instability in this mode. Therefore, because the existence of lower-hybrid instability depends on the density gradient, in this chapter, I focus on the study of lower-hybrid drift instability as a particular case of more general beam cyclotron instabilities.

In this regard, as one of the main goals of this thesis, I compare the stability of lower-hybrid density gradient-driven modes as predicted by the kinetic and fluid models. Therefore, in section (3.1) I review the theoretical description of LHDI and re-drive the dispersion relation of LHDI that is mentioned in Appendix B. In section (3.2) I start the stability analysis by comparing the eigenfrequency of Simon-Hoh instability with the kinetic model. I use the advanced fluid model [20] which includes the effects of the equilibrium electron current, finite ion flow velocity, electron inertia, electron temperature, plasma density gradients, and the Debye length effects. This model is, in general, nonlinear and can be used for nonlinear fluid simulations [21]. The eventual goal is that to understand in what limits we can use fluid model for nonlinear simulations. Because fluid simulations are cheaper in computational resources compare to nonlinear kinetic simulations. In section (3.3), I do my analysis with typical Hall thruster parameters along the thruster channel, and the last section of this chapter (3.4) is allocated to study a new regime between LHDI and Simon-Hoh instability.

3.1 Plasma equilibrium and theoretical description of LHDI

The density gradient modified long-wavelength mode actually belongs to the lower-hybrid drift branch. As all other modes, it is driven by the relative cross-field drift

between electrons and ions in the presence of inhomogeneities in plasma. With magnetized electrons and unmagnetized ions, the lower-hybrid drift instability is characterized as follows:

$$\Omega_{ci} < \omega < \Omega_{ce},\ b = k_y^2\rho_e^2 \leq 1,\ k_y^2\rho_i^2 \geq 1,\ \rho_e/L_n \leq 1, \tag{3.1}$$

here for simplicity, we do not consider the component of the wave vector in the direction of magnetic field ($\mathbf{k}\cdot\mathbf{B} = 0$). According to Ref. [22], in the limit of low-frequency and long wave length $(k_y\rho_e)^2 < 1,\ \Omega_{ci} < \omega < \Omega_{ce}$, two branches of plasma instabilities appear. One of them is MTSI (modified two stream instability) that occur for $(k_y\rho_e)^2 << 1,\ k_z \neq 0$, and $\omega - k_y v_E << \Omega_{ce}$ and the other one is lower-hybrid drift instability when $(k_y\rho_e)^2 < 1$, for any temperature ratio T_e/T_i and $k_z = 0$.

In order to gain a better understanding of the LHDI, I re-derive its dispersion relation according to the suggested method of Ref. [23] taking into account the equilibrium with a density gradient. We consider a plasma with exponential density profile for both species,

$$n_{0\alpha}(x) = n_A \exp\left(\frac{-x}{d}\right), \tag{3.2}$$

where d represents plasma thickness, in slab geometry, the magnetic field is uniform and in the z direction, and the external electric field is in the x direction. Therefore there are three single-particle constants of motions: velocity along the magnetic field v_z, the perpendicular energy $H_\perp$, and the canonical momentum p_y

$$\begin{aligned} H_\perp =& \frac{m_\alpha(v_x^2 + v_y^2)}{2} + q_\alpha\phi_0(x), \\ p_y =& m_\alpha(v_y + \epsilon_\alpha\Omega_{c\alpha}x), \end{aligned} \tag{3.3}$$

here $\epsilon_\alpha = \operatorname{sgn} q_\alpha$. In inhomogeneous plasma and under the influence of the electric field, the equilibrium distribution function is the local Maxwellian and the function of the constants of motion

$$f_{0\alpha}(\mathbf{x},\mathbf{v}) = f_{0\alpha}(H_\perp, p_y)G_\alpha(v_z) = \left(\frac{m_\alpha n_A}{2\pi T_{\perp_\alpha}}\right)\exp\left(-\frac{m_\alpha v_{y\alpha}^2}{2T_{\perp\alpha}}\right)\exp\left(-\frac{H_\perp - v_{y\alpha}p_y}{T_{\perp\alpha}}\right)G_\alpha(v_z), \tag{3.4}$$

where $T_{\perp\alpha}$ as the perpendicular temperature of particle type α, $v_{y\alpha}$ as the uniform flow velocity of particle type α and n_A, are all constant and the last part Eq. (3.4) satisfies the normalization condition $\int_{-\infty}^{\infty} dv_z G_\alpha(v_z) = 1$.

By linearizing the Vlasov equation, using the method of integration over the unperturbed orbit, and substituting the electron and ion charge density in Poisson's equation, we get the following dispersion relation of LHDI in the limit of the cold ion regime for this partially magnetized plasma. Details of this re-derivation that I have done, are given

in Appendix B, and hereinafter in this chapter, I will call this equation K1:

$$k^2\lambda_D^2 + 1 - I_0(\zeta)e^{-\zeta} + \frac{k_y v_n}{(\omega - k_y v_E)} I_0(\zeta)e^{-\zeta} - \frac{k^2\lambda_D^2\omega_{pi}^2}{\omega^2} = 0. \tag{3.5}$$

Since in my work I use the following Fig. (3.1) configuration and coordinate system, the notations are different, and I use the negative value for gradient length density L_n. For

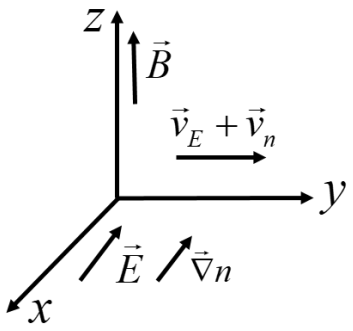

Figure 3.1: Initial configuration and coordinate system.

this reason, in Eq. (3.5) we define $\zeta = k^2\rho_e^2$, $v_n = -T_e dn_{0e}/(m\Omega_{ce} n_{0e} dx) = -T_e/eB_0 L_n$, $k^2 = (k_x^2 + k_y^2)$, $v_E = E_0/B_0$, and $\rho_e^2 = T_e/m_e\Omega_{ce}^2$.

Another alternative that results in lower-hybrid dispersion relation is to consider only $m = 0$ term in sum Eq. (2.14) of electron susceptibility in the presence of gradient density as follows:

$$K_e = \frac{k_e^2}{k^2}\left[1 + \frac{(\omega - k_y v_E + k_y v_n)}{\Omega_{ce}} \frac{1}{\sqrt{2(k_z^2\rho_e^2)}} \exp(-\zeta) I_0(\zeta) Z\left(\frac{\frac{\omega - k_y v_E}{\Omega_{ce}}}{\sqrt{2(k_z^2\rho_e^2)}}\right)\right]. \tag{3.6}$$

Assuming $k_z^2\rho_e^2 \to 0$ and using the characteristic of plasma dispersion function for $\xi >> 1$,

$$Z(\xi) = i\sqrt{\pi}\exp(-\xi^2) - \frac{1}{\xi}\left(1 + \frac{1}{2\xi^2}\right) \approx -\frac{1}{\xi}, \tag{3.7}$$

Eq. (3.6) yields:

$$K_e = \frac{k_e^2}{k^2}\left[1 - \exp(-\zeta) I_0(\zeta) + \frac{k_y v_n}{\omega - k_y v_E}\exp(-\zeta) I_0(\zeta)\right]. \tag{3.8}$$

Considering the cold ion, we will get the familiar form of dispersion as Eq. (3.5),

$$1 + K_i + K_e = 0,$$

$$k^2\lambda_D^2 + 1 - \frac{k^2\lambda_D^2\omega_{pi}^2}{\omega^2} - I_0(\zeta)e^{-\zeta} + k_y v_n \frac{I_0(b)e^{-b}}{(\omega - k_y v_E)} = 0. \tag{3.9}$$

3.1.1 Lower-hybrid drift instability for different values of the density gradient length

Here I have selected only $m = 0$ term in sum of Eq. (2.14) and modified the solver proposed in Ref. [12] to involve the effect of gradients density. I compare the impact of different density gradient lengths.

Table 3.1: Typical plasma parameters used for numerical solutions.

Variable	E_0	B_0	n	T_e	T_i	m_i	$k_z\lambda_D$
Value	10 kV/m	0.01 T	1×10^{18} m^{-3}	10 eV	0.0 eV	xenon	0.00001

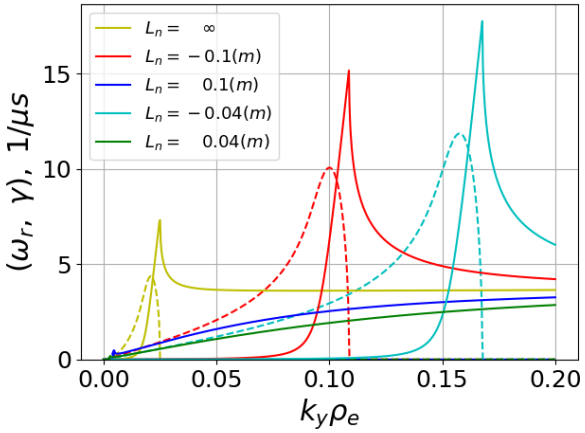

Figure 3.2: Effect of the density gradient drift to the dispersion relation ($k_z\lambda_D = 0.00001$), dashed lines represent growth rate and solid lines show frequency for $L_n = \infty, -0.1, +0.1, -0.04$, and $+0.04$ m. Parameters for this figure are mentioned in Table (3.1).

Figure (3.2) shows that negative density gradient lengths increase growth rate compare to the yellow line that is growth rate without gradient density drift. By contrast the positive density gradient lengths decrease instability considerably. Moreover, as before, the stronger density gradient length $L_n = -0.04$ m leads to the increase in the peak of growth rate and expansion of the unstable region into the lower azimuthal wavelength.

3.2 Comparison of the results from the kinetic and fluid theories

In the long-wavelength limit, the lower-hybrid mode becomes the Simon-Hoh instability which can be simply obtained from the anti-drift mode dispersion relation. In the presence of an external electric field $\mathbf{E} = -E_0\hat{x}$, the electron response in Eq. (1.49) modifies from

$\omega \to \omega - k_y v_E$, as a Doppler shift. This modification destabilizes gradient drift mode and leads to collisionless Simon-Hoh instability as follows:

$$\frac{k^2 c_s^2}{\omega^2} = \frac{k_y v_n}{\omega - k_y v_E}, \tag{3.10}$$

Equation (3.10) that I will call F1 in the remainder of this section can be achieved in the limit of long wavelength $k^2\rho_e^2 < 1$ of Eq. (3.5) of kinetic theory. In this limit, the first term of the Bessel function leads to $I_0(b)e^{-b} \approx 1 - b \approx 1$, therefore we will get the following dispersion equation:

$$-(k_x^2 + k_y^2)\lambda_D^2 - \frac{k_y v_n}{(\omega - k_y v_E)} + \frac{(k_x^2 + k_y^2)c_s^2}{\omega^2} = 0. \tag{3.11}$$

Without considering the first term that comes from the Poisson equation, we get a promising result.

According to the Ref. [20], this wave can be unstable with the following condition:

$$(\mathbf{k}\cdot\mathbf{B} \times \frac{\nabla n_{0e}}{n_{0e}})(\mathbf{k}\cdot\mathbf{B} \times \mathbf{E}) > 0. \tag{3.12}$$

For a simple case when magnetic field is in the z direction, wave vector has the only one component in the y direction and density is the function of x, the condition of instability Eq. (3.12) is written as $\mathbf{E}\cdot\nabla n_{0e} > 0$. Figure (3.3) illustrates this condition, where $\mathbf{E}$ is the applied external electric field that can be calculated from the electric potential between cathode and anode over the length of the system l.

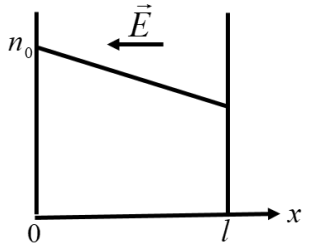

Figure 3.3: Necessary condition for instability $\mathbf{E}\cdot\nabla n_{0e} > 0$, vertical axis shows density profile and $\mathbf{E}$ is the applied external electric field. The figure is adopted from [24].

Figure (3.4) shows how the applied electric field causes $\mathbf{E}\times\mathbf{B}$ drift and moves the particles in the positive y direction. The electrons drift more rapidly than ions, thus produce an induced field $\mathbf{E}'$ as shown and a subsequent drift $\mathbf{v}'_{\mathbf{E}'\times\mathbf{B}}$ in the x direction.

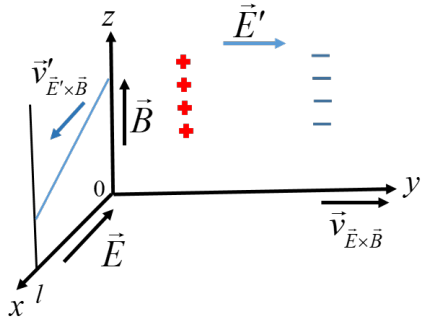

Figure 3.4: Induced electric field $\mathbf{E}'$ causes subsequent drift $\mathbf{v}'_{\mathbf{E}'\times\mathbf{B}}$ which is in the direction of decreasing density. The figure is adopted from [24].

Instability results when this drift is in the direction of decreasing density [24] that is provided by considering negative value of $L_n = (dn_{0e}/n_{0e}dx)^{-1} < 0$. Therefore, the diamagnetic drift $\mathbf{v}_n$ is in the $+y$ direction, so the wave with $\omega_r > 0$ travels in the same direction as electron (ion) drift.

If the direction of the applied electric field is reversed, it caused a drift of particles in the negative y direction, and as a consequence, produces an induced field $\mathbf{E}'$ and a subsequent drift $\mathbf{v}'_{\mathbf{E}'\times\mathbf{B}}$ is in the $-x$ direction, since instability results when this drift is in the direction of decreasing density, we need to consider $L_n = (dn_{0e}/n_{0e}dx)^{-1} > 0$. In this regard, the diamagnetic drift $\mathbf{v}_n$ is in the $-y$ direction, so the wave with $\omega_r < 0$ travels in the same direction as electron (ion) drift.

In the following, I will investigate how, where and in what approximations the numerical result of lower-hybrid drift dispersion from the kinetic theory transforms into the similar numerical result of the fluid theory, which is one of the goals of this chapter. In this regard, I have developed solvers in Matlab and Python to evaluate the real frequency and growth rate of the kinetic and fluid dispersion relations as a function of k_y for fixed k_x and vice versa. I categorize the results into three different regions of k_x from small to large, $k_x\rho_e < 1$, $k_x\rho_e \simeq 1$, and $k_x\rho_e > 1$.

For the first step, I compare the roots of the collisionless Simon-Hoh instability F1 with a dispersion equation that comes from the kinetic model K1 as a function of k_x and k_y. Next, I compare the result of the kinetic model K1 with numerical results of a general fluid dispersion equation F2 and F3 without and with a non-neutrality term respectively. These two fluid models consist of the effect of the electron inertia and the electron gyroviscosity. Table (3.2) shows a list of equations that I use in my comparison with a specific name that I assign for each of them. In these equations, I add the term of equilibrium ion flow in the axial direction, which introduces the Doppler shift in the ion response, $\omega \to \omega - k_x v_{0i}$. In some parts of my analysis, I compare the effect of ion flow on frequency and growth rate.

Table 3.2: List of equations used in the solver for comparison.

Equation	Equation code
$k_\perp^2\lambda_D^2 + 1 - \frac{k_\perp^2\lambda_D^2\omega_{pi}^2}{(\omega - k_x v_{0i})^2} - I_0(b)e^{-b} - k_y v_n \frac{I_0(b)e^{-b}}{(\omega - k_y v_E)} = 0$	K1
$\frac{k_y v_n}{\omega - k_y v_E} + \frac{k_\perp^2 c_s^2}{(\omega - k_x v_{0i})^2} = 0$	F1
$\frac{-k_y v_n + k_\perp^2 \rho_e^2(\omega - k_y v_E)}{(\omega - k_y v_E)(1 + k_\perp^2\rho_e^2)} - \frac{k_\perp^2 c_s^2}{(\omega - k_x v_{0i})^2} = 0$	F2
$k_\perp^2\lambda_D^2 + \frac{-k_y v_n + k_\perp^2 \rho_e^2(\omega - k_y v_E)}{(\omega - k_y v_E)(1 + k_\perp^2\rho_e^2)} - \frac{k_\perp^2 c_s^2}{(\omega - k_x v_{0i})^2} = 0$	F3

3.2.1 Comparing eigen frequency of kinetic model of lower-hybrid drift with Simon-Hoh modes

This section provides the analytical comparison between the roots of collisionless Simon-Hoh instability with the kinetic model K1 of LHDI.

It can be seen from Fig. (3.5) in $k_x^2\rho_e^2 < 1$ that except for a bit of difference, the roots of the fluid model of dispersion equation F1 as a function of $k_x\rho_e$ agree with the ones in the kinetic model K1. Since the order of magnitude non-neutrality term is low, $k^2\lambda_D^2 \approx 10^{-4}$ adding this term to the Eq. F1 doesn't have any considerable effect on final results. The parameters used in the analysis of this and the next section are mentioned in Table (3.3).

Table 3.3: Typical Hall thruster parameters used in the solver to compare eigenfrequencies of the kinetic and fluid models.

Variable	E_0	B_0	n	T_e	T_i	m_i	L_n	v_{0i}
Value	10 kV/m	0.01 T	1×10^{18} m^{-3}	10 eV	0.0 eV	xenon	-0.05 m	0.0 m/s

Figure (3.5) shows the stronger density gradient length $L_n = -0.005$ m expands the unstable region into the lower wavelength and decreases discrepancy between F1 and K1. In the following part, I compare the behavior of eigenfrequency from the kinetic approach with the fluid model at shorter azimuthal wavelengths.

We can see from the Fig. (3.5), as is shown in Ref. [25] that the growth rate of unstable gradient drift modes from Eq. F1 increases with k_x and reaches the maximum at $\omega_0 = k_y v_E$ for different azimuthal wave vectors k_y. As it is clear, at this point, the real part of frequency becomes equal to the growth rate, and for the higher values of k_x, the growth rate decreases, and finally, the mode becomes stable. By contrast, the roots of the kinetic model do not show a similar pattern.

Figure (3.6) reveals that for higher azimuthal wave vector k_y, eigenfrequencies of two approaches lose their consistency. Although by increasing k_y, the maximum growth rate of

Eq. F1 rises, and its unstable region expands into lower wavelengths, the roots of Eq. K1 represent the movement toward a situation in which there are two distinct regimes. The long-wavelength regime has a growth rate in the long-wavelength limit and becomes stable at $k_x\rho_e$ of order unity. The second, short-wavelength regime emerges at $k_x\rho_e > 1$ and shows an unstable island region with a growth rate lower than that of its fluid counterpart [8]. In Fig. (3.7) I investigate the behavior of the eigenmodes of Eqs. F1 and K1 as a function of azimuthal wave vector k_y in different fixed values of the k_x.

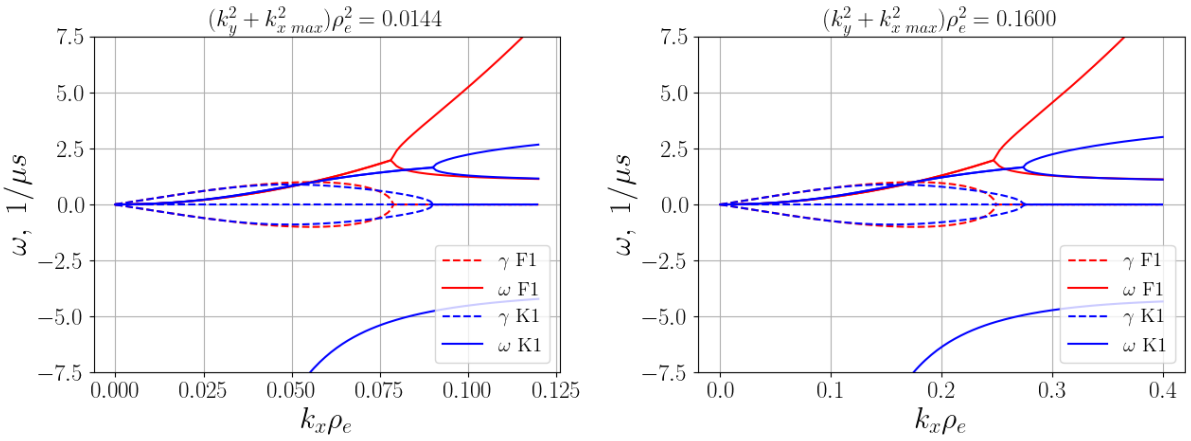

(a) **(b)**

Figure 3.5: Frequency and growth rate of the anti-drift mode in equations K1 and F1, destabilized by electron flow as a function of the axial wave-vector $k_x\rho_e$ with $k_y = 1$ m^{-1} and $v_{0i} = 0$ m/s (a) $L_n = -0.05$ m and (b) $L_n = -0.005$ m.

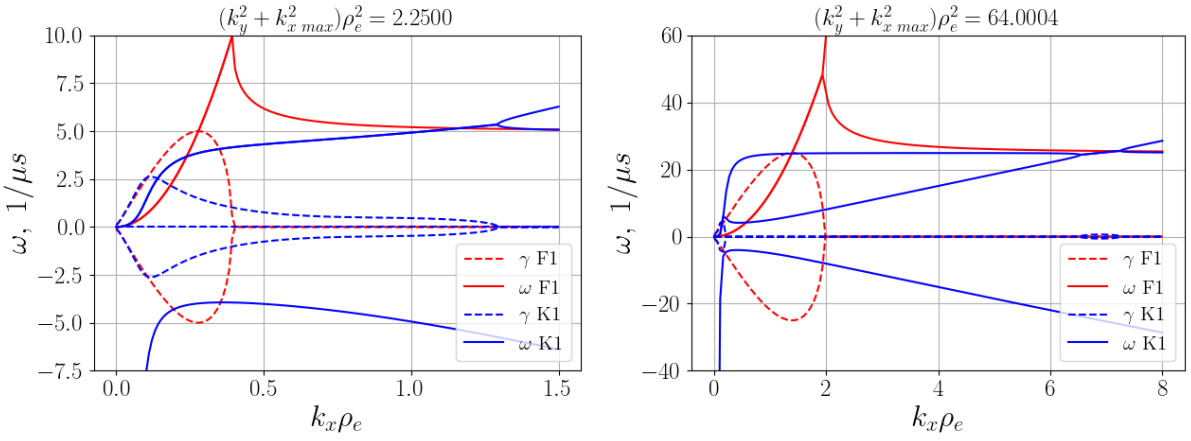

(a) **(b)**

Figure 3.6: Frequency and growth rate of the anti-drift mode in equation K1 and F1, destabilized by electron flow as a function of axial wave-vector $k_x\rho_e$ for (a) fixed $k_y = 5$ m^{-1} and (b) fixed $k_y = 25$ m^{-1} with $L_n = -0.05$ m.

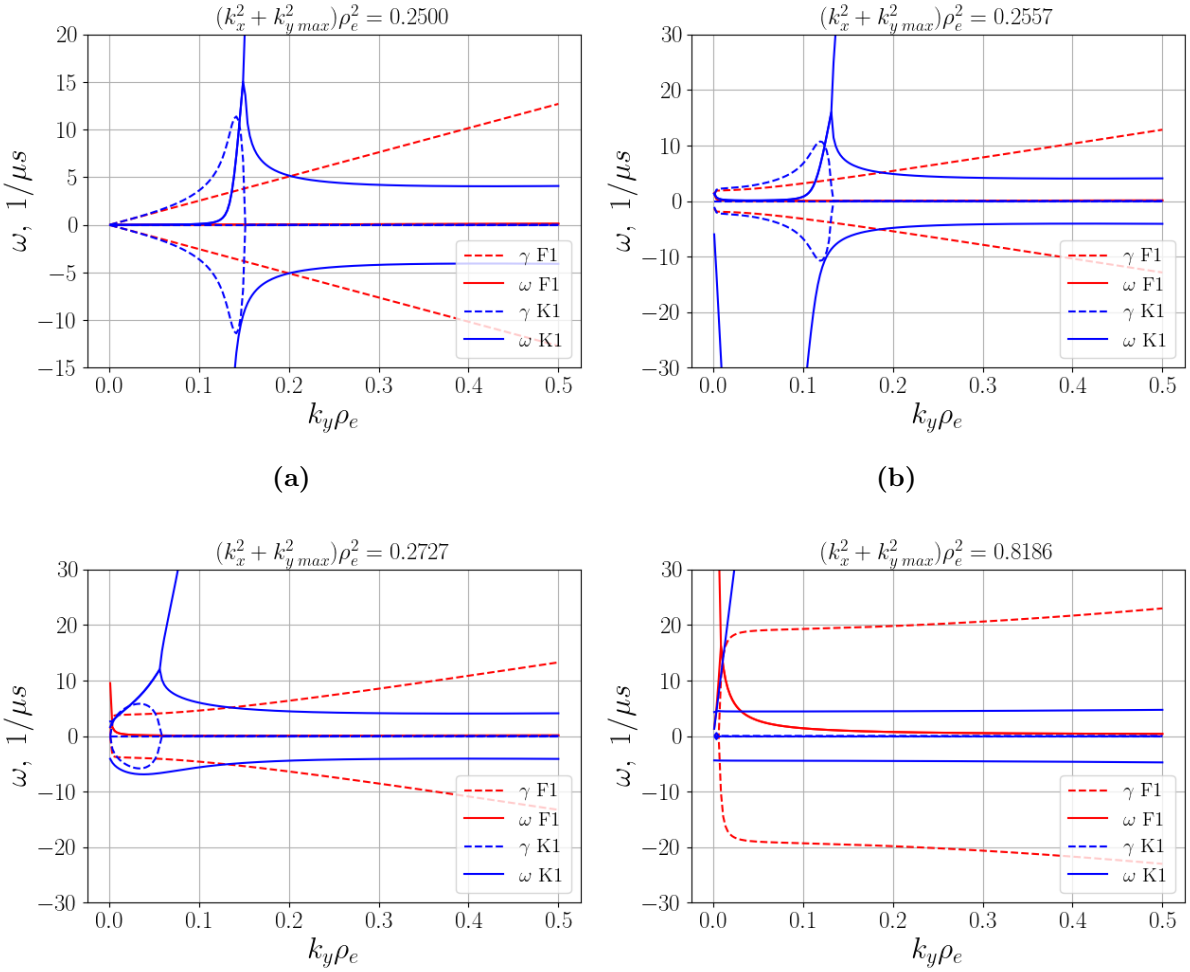

Figure 3.7: Frequency and growth rate of the Eqs. F1 and K1 destabilized by electron flow as a function of azimuthal wave vector $k_y\rho_e$ for fixed (a) $k_x = 0$ m^{-1}, (b) $k_x = 100$ m^{-1}, (c) $k_x = 200$ m^{-1}, and (d) $k_x = 1000$ m^{-1} which varies from $k_x\rho_e = 0.0$ till $k_x\rho_e = 0.754$.

As it is clear from Fig. (3.7), for given parameters, Simon-Hoh instability shows the monotonous dependency of growth rate to $k_y\rho_e$ with no threshold while the kinetic model represents the growth rate that its peak shrinks by increasing axial wave vector and disappears entirely when axial wave vector becomes $k_x = 1000$ m^{-1}.

3.2.2 Comparing eigen mode of kinetic model of LHDI with general fluid dispersion

As can be seen from the figures of the previous section, for $k_\perp^2\rho_e^2 > 1$ the consistency between the resulted eigenfrequency of Simon-Hoh instability and the kinetic model of lower-hybrid drift instability is lost. For this reason, in general, the kinetic approach

is more recommended for the high value of $k_\perp^2\rho_e^2 >> 1$. In this subsection I will show that the contributing electron inertia effect and electron gyroviscosity in Eq. F2, which describes the finite electron Larmor radius (FLR) effect, can compensate for the deficiency in the fluid model F1. Practically, the gyroviscosity, in the limit of large, $k_\perp^2\rho_e^2 >> 1$, provides equivalent behavior of Pade type approximation of Bessel functions appearing in the kinetic equation K1 [20].

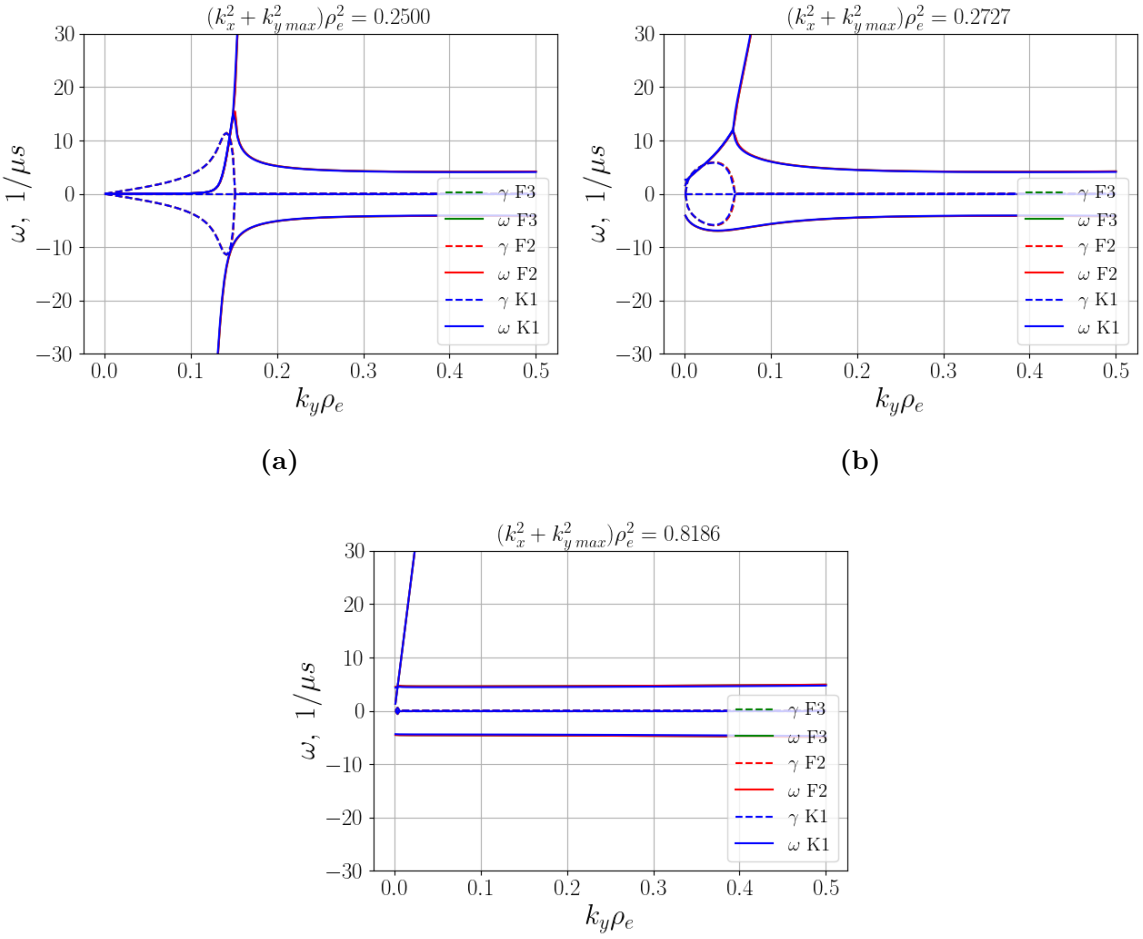

(a) **(b)**

(c)

Figure 3.8: Frequency and growth rate of the Eq. F2, F3 and K1 destabilized by electron flow as a function of azimuthal wave vector $k_y\rho_e$ for fixed (a) $k_x = 0$ m^{-1}, (b) $k_x = 200$ m^{-1}, and (c) $k_x = 1000$ m^{-1}, which varies from $k_x\rho_e = 0.0$ till $k_x\rho_e = 0.754$.

It can be seen from Fig. (3.8) that the roots of the fluid model of dispersion equations F2, F3, and kinetic dispersion K1 overlap completely. Furthermore, increasing $k_x\rho_e$ from 0 to almost 1 couples eigenfrequency of F2 and K1 to short azimuthal wavelength while shrinks unstable regime to the lower growth rate.

In this part, I examine the effect of ion flow v_{0i} on the instability. According to Ref. [26], the experimental measurement of instability frequency γ and ion drift frequency

$k_x v_{0i}$ reveals that ion flow is in the range of maximum growth rate over axial wave vector, $v_{0i} \approx -\gamma_{max}/k_x$.

Figure (3.9) shows that the presence of the finite axial ion drift frequency $k_x v_{0i}$ in dispersion relations, modifies real part of the eigen-frequency and decrease y-intercept of that at the order of $k_x v_{0i}$ [27]. Moreover selecting ion flow in the range of $-\gamma_{max}/k_x$ decreases the maximum growth rate from $k_y v_E$ slightly and shortens the unstable region.

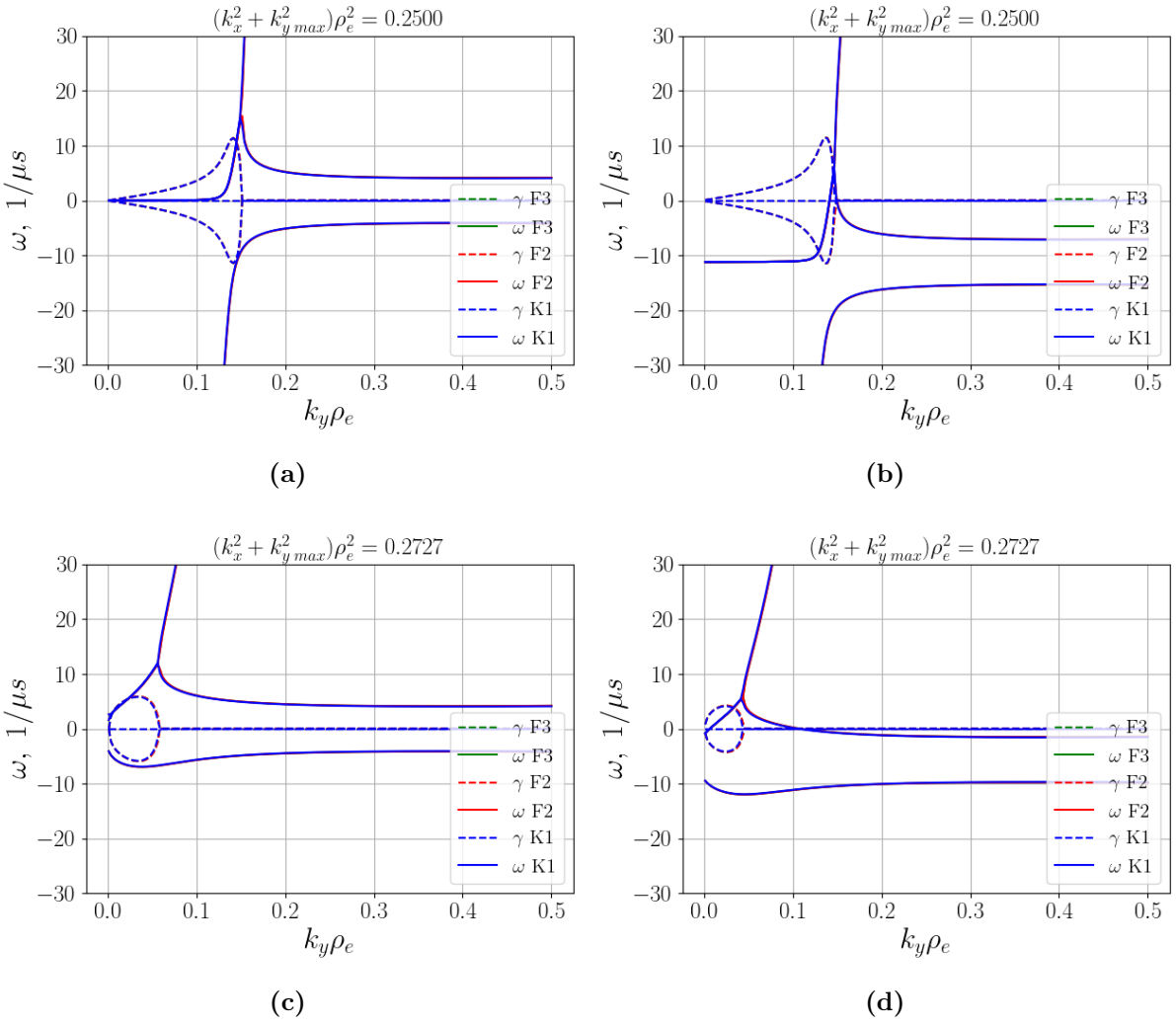

Figure 3.9: Frequency and growth rate of the Eqs. F2, F3 and K1 destabilized by electron flow in (a) $k_x = 1\ \mathrm{m}^{-1}, v_{0i} = 0$ m/s, and (c) $k_x = 200\ \mathrm{m}^{-1}, v_{0i} = 0.0$ m/s and by both electron and ion flow in (b) $k_x = 1\ \mathrm{m}^{-1}, v_{0i} = -11.2e6$ m/s, and (d) $k_x = 200\ \mathrm{m}^{-1}, v_{0i} = -2.81e4$ m/s as a function of azimuthal wave vector $k_y\rho_e$.

To investigate and compare the effect of electric field on the growth rate of LHDI in both kinetic and fluid models, I use the Color plot, which provides deep insight into changes. Therefore I solve dispersion relations in the $k_x - k_y$ plane. Figure (3.10) shows the results of the kinetic model K1 and Fig. (3.11) shows growth rate of the fluid model

F2. Excluding the electric field, all other parameters used in this analysis are shown in Table (3.3).

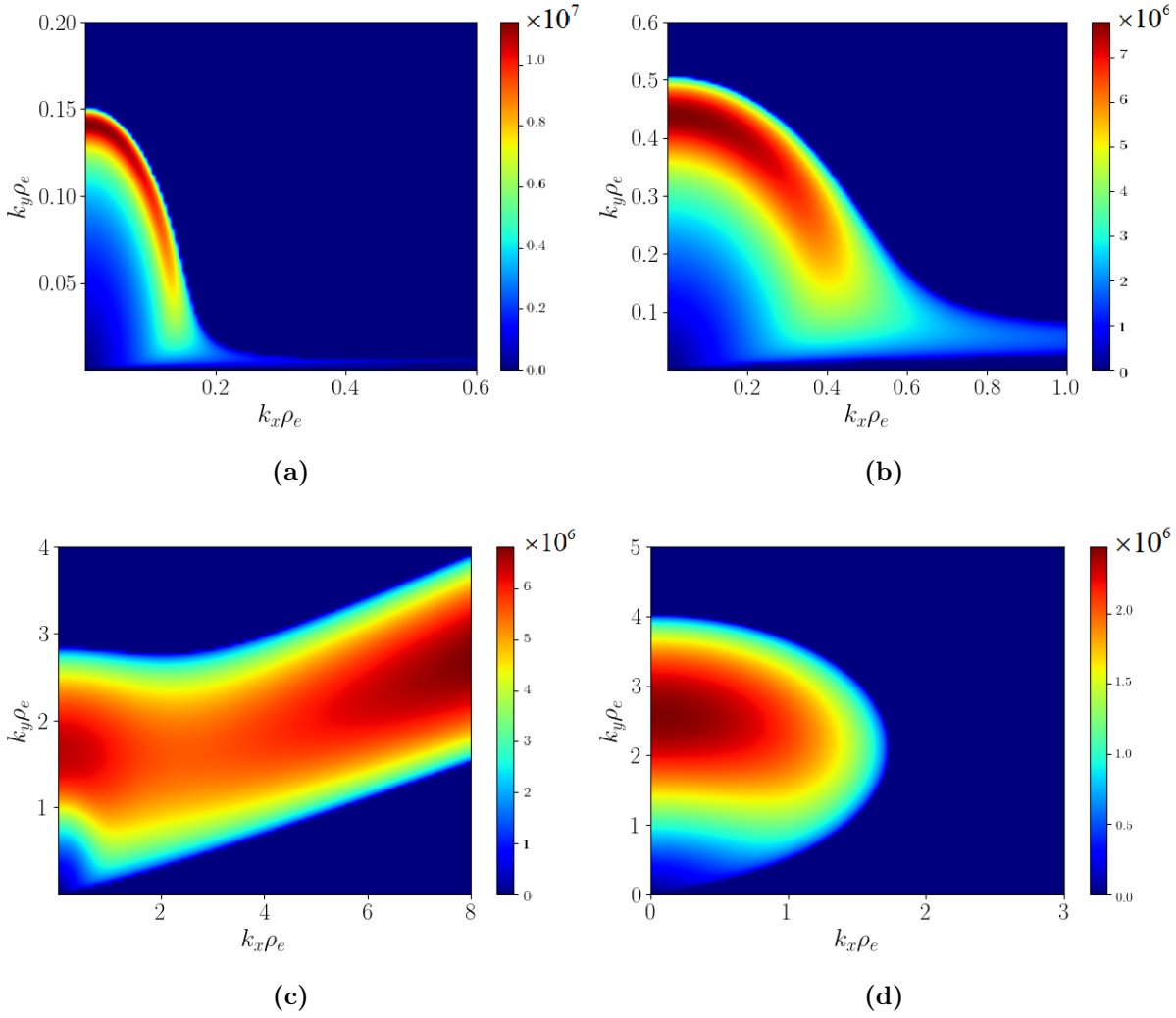

Figure 3.10: Color plot of growth rate of the kinetic approach of LHDI in 2D plane of $k_x - k_y$ with different electric fields. (a) $E_0 = 10000$ V/m, (b) $E_0 = 1000$ V/m, (c) $E_0 = 100$ V/m, (d) $E_0 = 10$ V/m. Color bar indicates the values of growth rate in different color regions.

It can be concluded from Fig. (3.10a) that the most unstable modes occur in lower k_x around $k_y\rho_e$ between 0.1 to 0.15. By increasing the axial wave vector, the instability region disappears sharply. In this lobe of instability, the maximum growth rate occurs at $\gamma \approx 1.2 \times 10^7$ Hz.

As it is clear from Fig. (3.10b), decreasing the electric field from 10 kV/m to 1 kV/m, broadens the lobe of the unstable region into higher axial and azimuthal wave vector. Also, the maximum growth rate occurs at $\gamma \approx 0.8 \times 10^7$ Hz with $\approx 30\%$ reduction compare to the part (a).

Figure (3.10c) reveals the existence of two branches of the instability. The larger peak occurs in the shorter axial wavelength at the maximum growth rate of $\gamma \approx 0.7 \times 10^7$ Hz, whereas the smaller peak occurs at the large axial wavelength. It can be seen by increasing the axial wave vector; the unstable region impels into the larger azimuthal wave vector and produces an island-type unstable region.

Figure (3.10d) illustrates that for the low electric field $E_0 = 10$ V/m, unstable modes impel from axial wave vector toward azimuthal ones. Here, we observe the island type unstable region by increasing k_x also the maximum growth rate occurs at $\gamma \approx 0.3 \times 10^7$ Hz.

In general, lowering the electric field makes the unstable region from the axial wave vector toward the larger azimuthal wave vector.

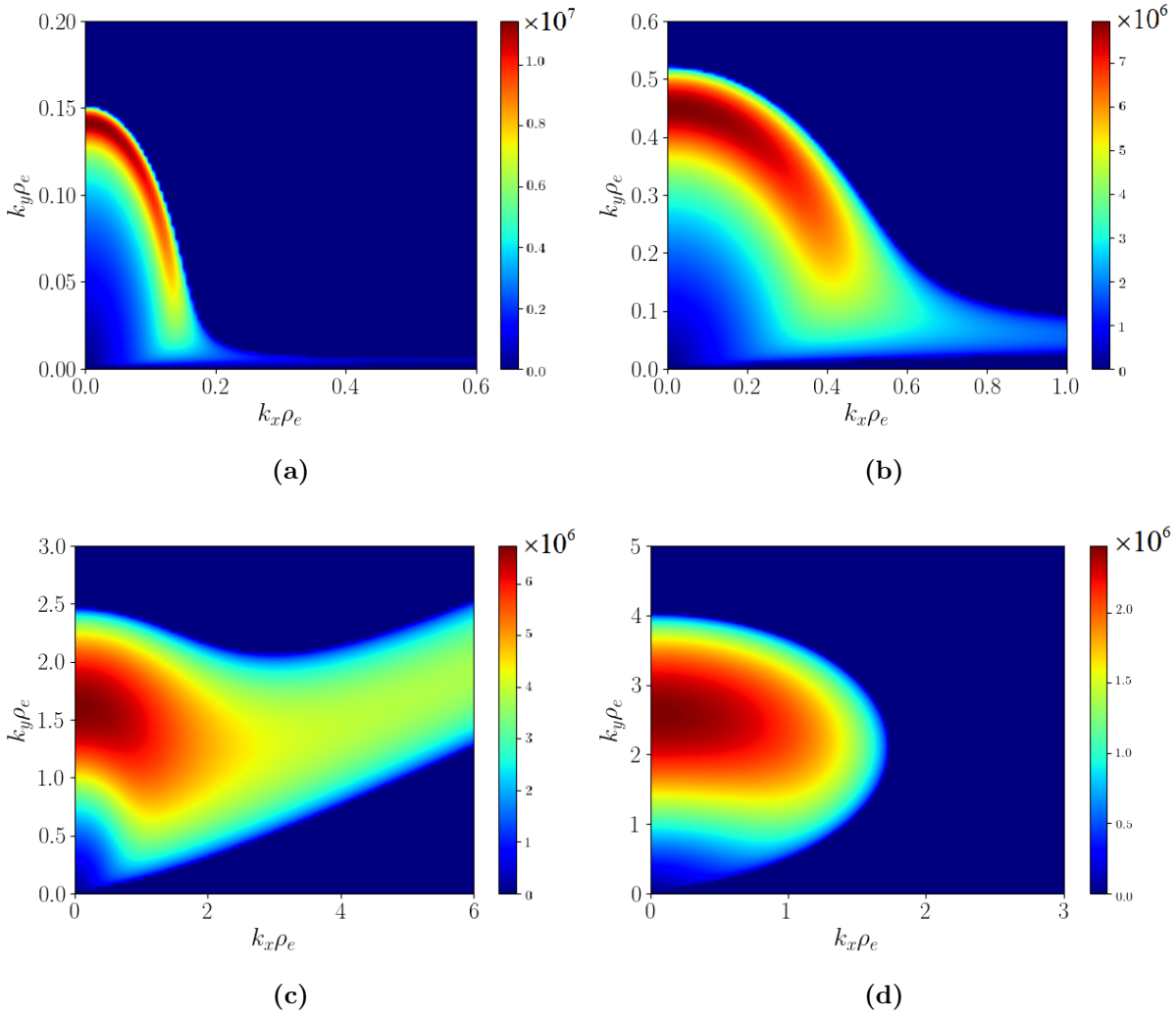

Figure 3.11: Color plot of growth rate of fluid approach Eq. F2 in 2D plane of $k_x - k_y$ with various electric fields. (a) $E_0 = 10000$ V/m, (b) $E_0 = 1000$ V/m, (c) $E_0 = 100$ V/m, (d) $E_0 = 10$ V/m. color bar indicates the values of growth rate in different color regions.

Color plots of the advance fluid dispersion relation Fig. (3.11) that consists of the

effect of the electron inertia and the electron gyroviscosity show good consistency with corresponding the kinetic dispersion relation of lower-hybrid drift instability. The most considerable difference is, for the lower electric field case, $E_0 = 100$ V/m and $E_0 = 10$ V/m where the fluid approach depicts less domain of instability with the lower growth rate compared with the kinetic method. Moreover, the second branch of instability for $E_0 = 100$ V/m that occurs for the large axial wave vector disappears completely in this model.

3.3 Kinetic and fluid stability analysis of LHDI applied to some specific plasma parameters profiles in Hall thrusters

This section analyzes and compares the stability of density gradient drift waves with typical Hall thruster parameters in the framework of the kinetic and fluid based on solving their dispersion relations. In this regard, the properties of unstable modes from the kinetic and the fluid models are calculated along the thruster channel.

According to the data from different thrusters studies [16, 18, 28], the axial profiles for equilibrium plasma parameters change widely between different regions of the Hall thruster. The radial magnetic field of the classical coaxial SPT has an axial profile that increases from the anode region, peaks at the edge of the channel exit, and decreases in the plume region. The axial profile of plasma density and the electric field is similar to the magnetic field profile with different coefficients that characterize each function's rate of change based on SPT-100 thruster data. Figure (3.12) illustrates the dependencies of $B(x), n(x), E(x)$ on the axial position x/d calculated from profiles (3.13), (3.14), and (3.15) respectively as they are suggested in Ref. [28].

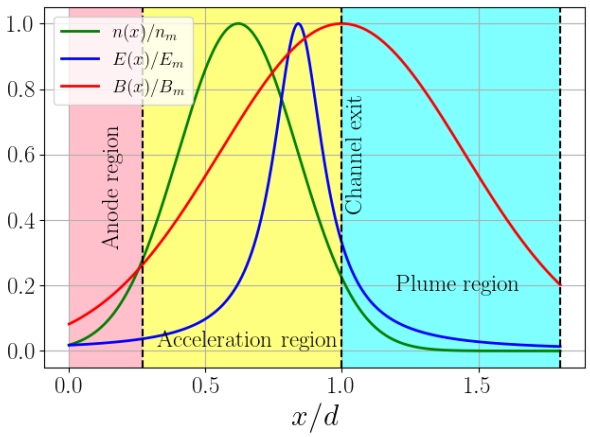

Figure 3.12: Variation of density, electric field, and magnetic field along the channel of the plasma thruster.

$$B(x) = B_m \exp\left[-\nu_1(\frac{x}{d} - 1)^2\right], \tag{3.13}$$

$$n(x) = n_m \exp\left[-\nu_2(\frac{x}{l_1} - 1)^2\right], \tag{3.14}$$

$$E(x) = E_m / \left[1 + \nu_3^2(\frac{x}{l_2} - 1)^2\right], \tag{3.15}$$

where $d = 25$ mm is the length of acceleration channel of SPT 100, $\nu_1 = 2.5$, $\nu_2 = 4$, $\nu_3 = 7.5$ are coefficients characterizing the rate of change of functions $B(x)$, $n(x)$, $E(x)$ respectively and $l_1 = 0.62d$, $l_2 = 0.84d$ corresponds to some point inside the acceleration channel where respectively the density and electric field reach their maximal value. For comparing the instability from the kinetic and fluid approaches, the xenon plasma with following the absolute values of parameters are used $E_m = 33147$ V/m, $B_m = 180$ G, $n_m = 0.5 \times 10^{18}$ m^{-3}. Thus, from the plasma density profile, I calculate the inverse of density gradient length as follows:

$$\frac{1}{L_n} = \frac{1}{n(x)}\frac{\mathrm{d}n(x)}{\mathrm{d}x} = -\frac{2\nu_2}{l_1}\left(\frac{x}{l_1} - 1\right) \tag{3.16}$$

Here we consider only the effect of gradient density; therefore, the necessary instability condition $\mathbf{E} \cdot \nabla n > 0$ for gradient-drift waves determines the instability region of the thruster channel. It is worth noting that since the electric field in this setup is in the $+x$ direction, the positive density gradient length verifies instability criteria. For comparing

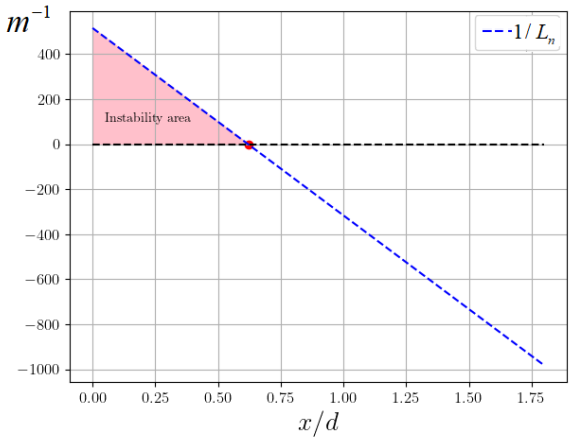

Figure 3.13: Variation of $1/L_n$ as function of x/d, pink color area shows the instability region which is expand till the middle of acceleration region $x/d = 0.62$.

the eigenfrequency of the dispersion relation of the kinetic model K1 for LHDI with the fluid models F2 and F3, I select five positions (Table (3.4)) in instability region $x/d < 0.62$ Fig. (3.13) and calculate the value of density, electric field, magnetic field,

and density gradient length from the recommended profiles Fig. (3.12) to put in the dispersion equations. In this comparison plasma is xenon with hot electron temperature $T_e = 10$ eV.

Table 3.4: Typical parameters along the channel of the plasma thruster used for numerical solutions.

	Units	Anode region ($x/d = 0.0$)	Anode region ($x/d = 0.17$)	Anode region ($x/d = 0.28$)	Acceleration region ($x/d = 0.5$)	Acceleration region ($x/d = 0.60$)
L_n	m	0.00194	0.00272	0.00359	0.01001	0.0934
n	m^{-3}	$0.00916e18$	$0.0678e18$	$0.1620e18$	$0.4399e18$	$0.4979e18$
E	V/m	578.98	932.75	1323.89	3406.84	5927.67
B	G	14.77	33.76	51.21	98.54	120.67

Figure (3.14a) shows that near the anode, the instability is localized in large $k_y\rho_e$ and there is a discrepancy between the eigenfrequency of the kinetic model with the fluid model. Meanwhile, the growth rate and frequency of two fluid dispersion relations F2 and F3, have a good consistency due to the small value of non-neutrality term at the order of $k_y\lambda_D \approx 10^{-4}$. As can be seen from the figure, the maximum growth rate of the K1 equation occurs at $\gamma_{max} = 9.4$ MHz whereas F2 and F3's maximum growth rate stands at $\gamma_{max} = 7.2$ MHz. The unstable region of the kinetic model extends till $k_y\rho_e = 4$ while the fluid model shows a shorter azimuthal unstable region.

Figure (3.14b) displays that at the middle of the anode region, the growth rate of the kinetic model overlaps with the growth rate of the fluid model, while the frequency of both graphs of K1 and F2 shows a slight difference.

By moving toward the acceleration region, the rate of shrinking the unstable area of the kinetic model becomes more than the fluid model. In acceleration region, since the instability is localized in small $k_y\rho_e$, the difference between considering electron FLR effect in Bessel function of kinetic model with Pade approximation of this function in fluid model becomes negligible. Therefore, the growth rate and frequency of the kinetic and the fluid dispersion relations show good consistency, the maximum growth rate at $x/d = 0.60$ stays at the level of $\gamma_{max} = 10$ MHz with shorter azimuthal unstable region compare to the four previous positions.

Since the most considerable difference in eigenfrequency of the kinetic with the fluid dispersion relation occurs at the anode region, I use the Color plot of the growth rate of dispersion relations in the $k_x - k_y$ plane for three positions in anode region in Figs. (3.15-3.17).

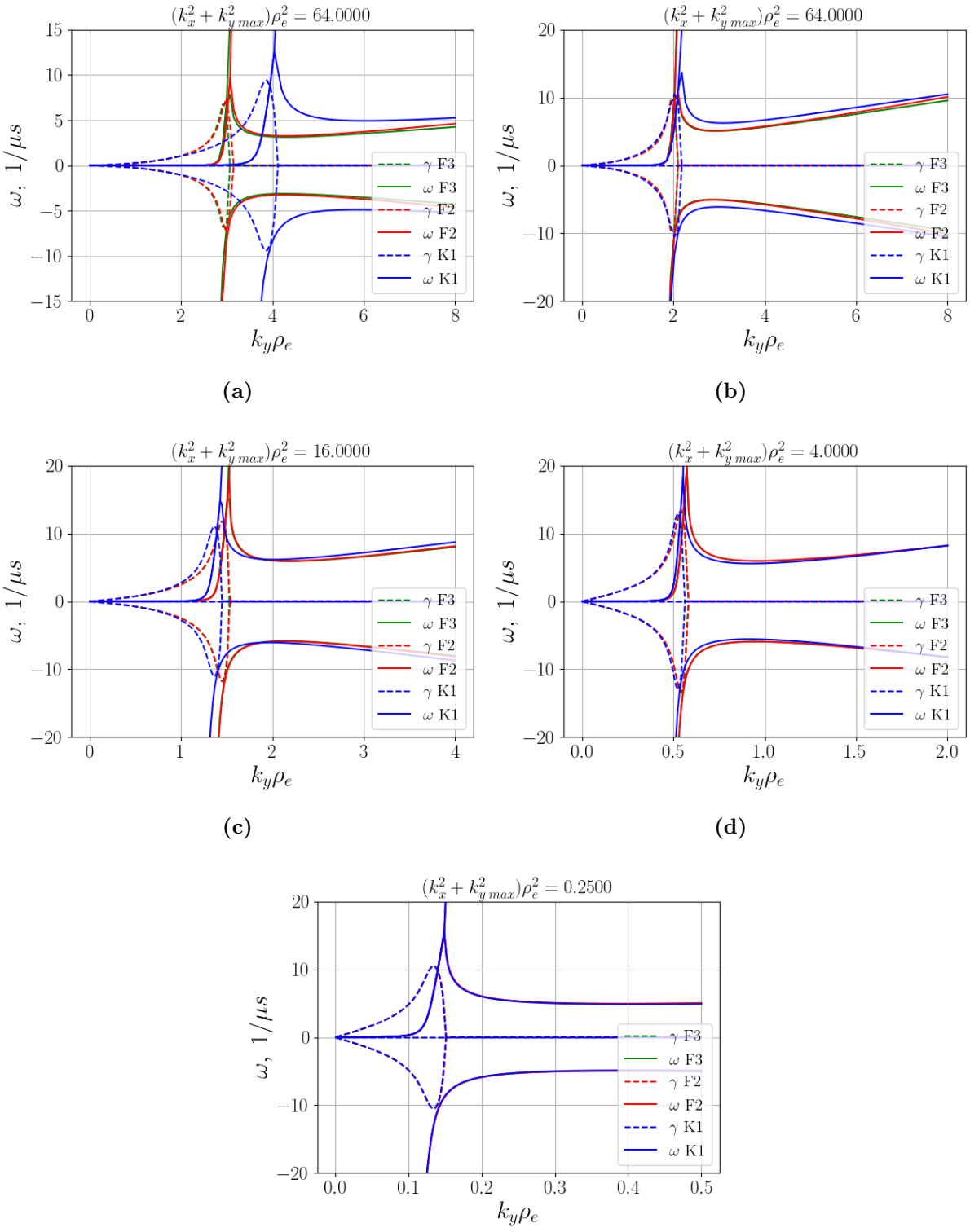

Figure 3.14: Frequency and growth rate of the lower-hybrid drift mode in equations K1 and F2, and F3 destabilized by electron flow as a function of the azimuthal wave-vector $k_y\rho_e$ in five different position in thruster channel. Here $k_x = 0.0$ and (a) $x/d = 0.0$, (b) $x/d = 0.17$, (c) $x/d = 0.28$, (d) $x/d = 0.5$, (e) $x/d = 0.60$.

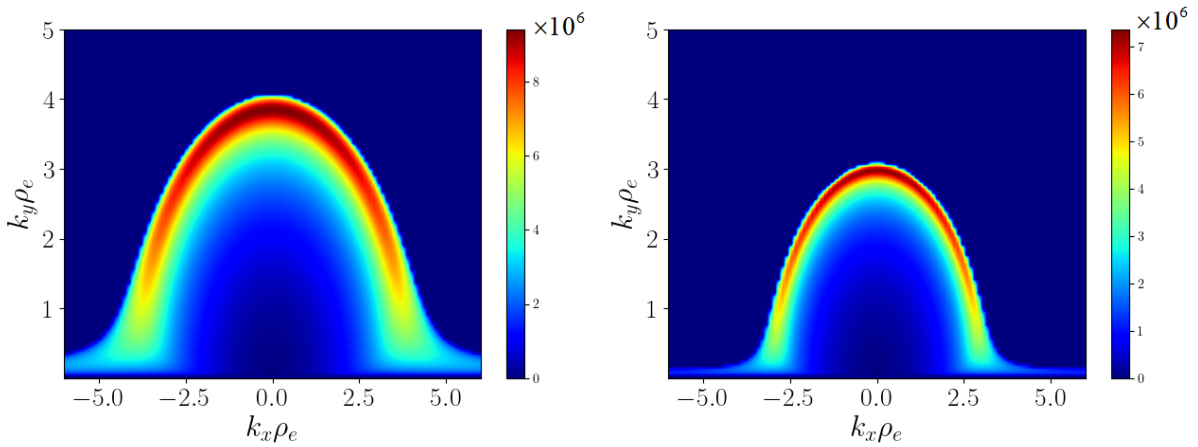

Figure 3.15: Color plot of growth rate of LHDI from solving (a) Eq. K1, (b) Eq. F2 in 2D plane of $k_x - k_y$ with $k_z = 0$ near the anode at position $x/d = 0.0$, the parameter of this graph is shown in Table (3.4). Color bar indicates the values of growth rate in different color regions.

Figure (3.15) clearly shows that near the anode, the unstable region of the kinetic model is twice wider than the fluid model. In addition, for the kinetic model, the most unstable modes (dark red area) occur in the lower axial wave vector around $k_y\rho_e = 3.155$ till $k_y\rho_e = 3.925$, and the maximum growth rate can be seen at $\gamma_{max} = 9.37$ MHz in purely azimuthal wave vector. While for Eq. F2 the most unstable modes are around $k_y\rho_e = 2.643$ till $k_y\rho_e = 3.035$ is $\gamma_{max} = 7.36$ MHz. We can see that the instability occurs for the long wavenumber and the width of the unstable region decreases very fast by increasing the axial wave vector for both models.

It can be concluded from Fig. (3.16) that by moving away from the anode, the consistency between kinetic model and fluid has increased. The most unstable modes, for Eq. K1 occur around $k_y\rho_e = 1.68$ till $k_y\rho_e = 2.105$ and the maximum growth rate is $\gamma_{max} = 10.5$ MHz in purely azimuthal wave vector. For Eq. F2, the most unstable area is between $k_y\rho_e = 1.813$ till $k_y\rho_e = 2.052$ with maximum growth rate $\gamma_{max} = 10.2$ MHz.

Figure (3.17) displays that at the end of the anode region, the unstable region in axial direction becomes similar for both models. The maximum growth rate of Eq. K1 is at $\gamma_{max} = 11.08$ MHz in purely azimuthal wave vector while For Eq. F2, the maximum growth rate is $\gamma_{max} = 11.64$ MHz.

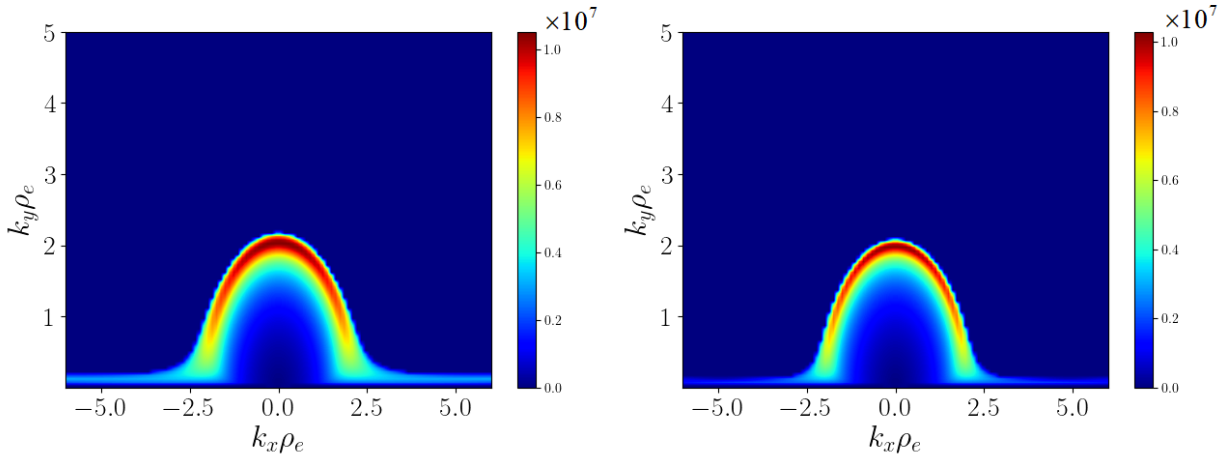

(a) **(b)**

Figure 3.16: Color plot of growth rate of LHDI from solving (a) Eq. K1, (b) Eq. F2 in 2D plane of $k_x - k_y$ with $k_z = 0$ near the anode at position $x/d = 0.17$, the parameter of this graph is shown in Table (3.4). color bar indicates the values of growth rate in different color regions.

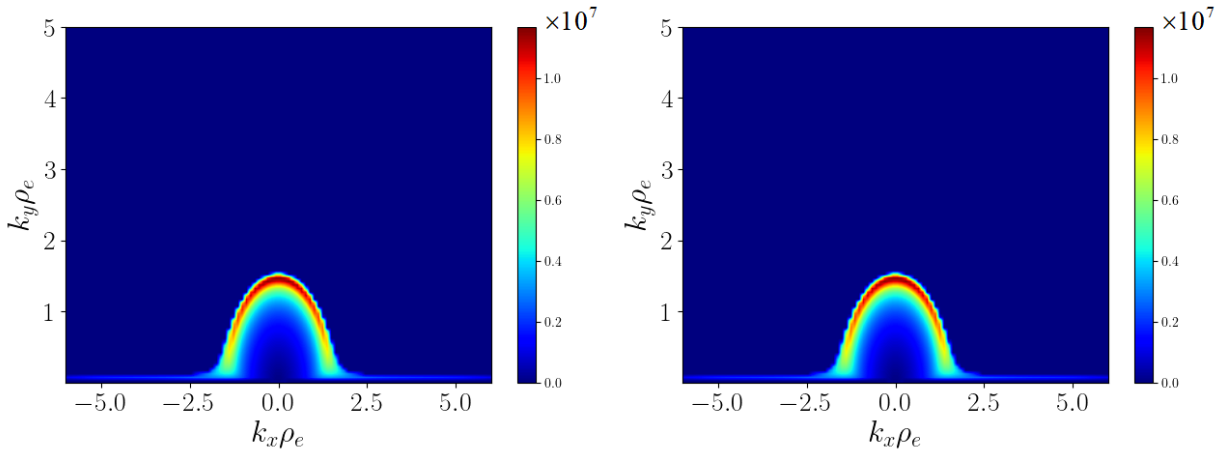

(a) **(b)**

Figure 3.17: Color plot of growth rate of LHDI from solving (a) Eq. K1, (b) Eq. F2 in 2D plane of $k_x - k_y$ with $k_z = 0$ near the anode at position $x/d = 0.28$, the parameter of this graph is shown in Table (3.4). color bar indicates the values of growth rate in different color regions.

3.4 Relation between the LHDI mode and Simon-Hoh instability

In the cold electron approximation ($T_e \to 0$) where the electron gyroviscosity is omitted, the dispersion relation F3 in Table (3.2) can be written as:

$$1 - \frac{\omega_{pi}^2}{\omega^2} + \frac{\omega_{pe}^2}{\Omega_{ce}^2} - \frac{k_y \omega_{pe}^2}{L_n \Omega_{ce} k_\perp^2 (\omega - k_y v_E)} = 0. \tag{3.17}$$

This equation describes a relation between dispersion equation F1 with non-neutrality term as inertia-less Simon-Hoh instability and the lower-hybrid instability F3.

Dispersion relation (3.17) can be concluded from the kinetic dispersion relation (3.5), by considering the first coefficient of $I_0(b)e^{-b} \approx 1 - b$ and the second $I_0(b)e^{-b} \approx 1$ for the long wave length limit $k^2\rho_e^2 < 1$.

Here I solve the above cold plasma dispersion relation for xenon plasma and investigate a new regime that has not be studied in applications to Hall thrusters. Unlike the paper [29] that focuses on the strong magnetic and electric fields, we report also this instability for low electric and magnetic fields. Figure (3.18) shows the dispersion diagram of Eq. (3.17) for different ranges of the electric and magnetic field. In this figure, the maximum growth rates γ_{max} can be found at [29],

$$\gamma_{max} = \sqrt{\frac{-v_E}{2L_n\Omega_{ci}}}\omega_r. \tag{3.18}$$

The critical value for investigating this island regime is keeping the value of $v_E/(|L_n|\Omega_{ci})$ in the order of 0.1.

To understand the stability of this new regime, I solve dispersion relation analytically to obtain the stability criterion and present the stability diagram. Since the dispersion relation of (3.17) is cubic with respect to frequency ω, the direct analysis of that, is not very easy. Here I use the method of Ref. [30] for studying this equation analytically.

For the analysis of stability, I rewrite the dispersion relation (3.17) in the normalized form as follows:

$$1 - \frac{1}{L_n k_y}\frac{\Omega_{ce}}{\omega_{LH}}\left(\frac{1}{\Omega + k_y\sigma}\right) - \frac{1}{\Omega^2} = 0, \tag{3.19}$$

where $\Omega = \omega/\omega_{LH}$, $\sigma = -v_E/\omega_{LH}$, and $\omega_{LH} = \omega_{pi}(1 + \omega_{pe}^2/\Omega_{ce}^2)^{-1/2}$ is lower-hybrid frequency. We can write $\Omega_{ce}/\omega_{LH} = (m_i/m_e)^{1/2}$ and then rewrite it in following form,

$$\Omega^3 + \Omega^2\bar{\sigma}\lambda - \Omega - \bar{\sigma} = 0, \tag{3.20}$$

where $\lambda = 1 - (m_i/m_e)^{1/2}/(k_y^2 L_n \sigma) = 1 - \alpha\sigma/\bar{\sigma}^2$, $\bar{\sigma} = k_y\sigma$, and $\alpha = \omega_{LH}/(L_n\Omega_{ci})$. The roots of this cubic equation are stable if and only if all of them are real and confirm the

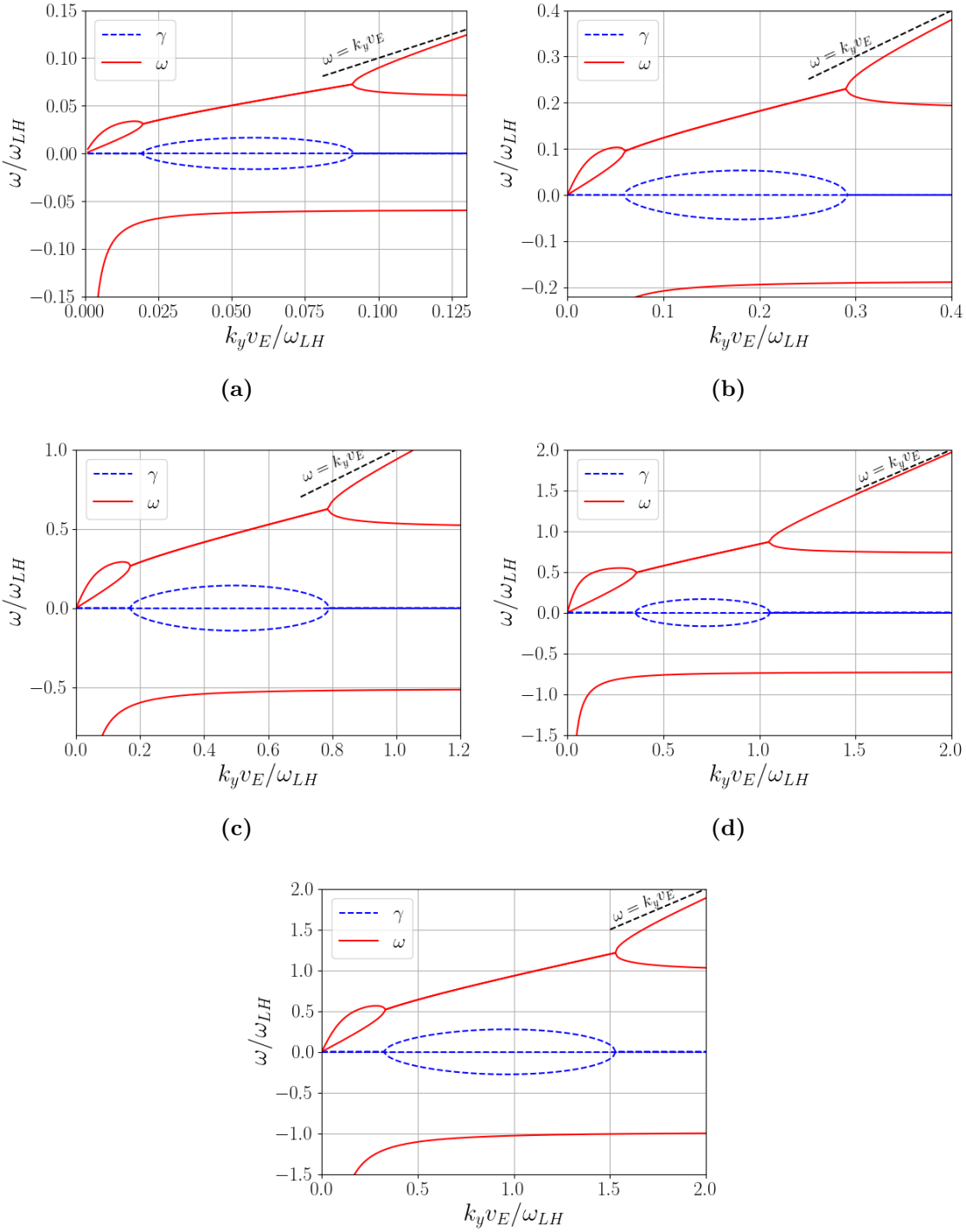

Figure 3.18: Frequency and growth rate of purely azimuthal lower-hybrid instability in the cold plasma for different electric and magnetic field,(a) $B_0 = 18000$ G, $E_0 = 20$ kV/m, $v_E/(|L_n|\Omega_{ci}) = 0.168$ (b) $B_0 = 5600$ G, $E_0 = 2$ kV/m, $v_E/(|L_n|\Omega_{ci}) = 0.174$ (c) $B_0 = 1800$ G, $E_0 = 200$ V/m, $v_E/(|L_n|\Omega_{ci}) = 0.168$ (d) $B_0 = 1000$ G, $E_0 = 40$ V/m, $v_E/(|L_n|\Omega_{ci}) = 0.109$ (e) $B_0 = 180$ G, $E_0 = 2$ V/m, $v_E/(|L_n|\Omega_{ci}) = 0.168$. Here, ω and $k_y v_E$ are normalized by the lower-hybrid frequency ω_{LH}. Parameters for these figures are: $T_e = 10$ eV, $n = 1 \times 10^{17}$ m^{-3}, $m_{xenon} = 2.18e-25$ kg, $k_x = 0.0$ m^{-1}, $L_n = -0.05$ m.

following condition [30],

$$4\lambda^3\bar{\sigma}^4 + (\lambda^2 + 18\lambda - 27)\bar{\sigma}^2 + 4 \geq 0\ . \tag{3.21}$$

We have a quadratic trinomial with respect to $\bar{\sigma}^2$, therefore we can rewrite condition (3.21) in this form

$$\lambda^3(\bar{\sigma}^2 - \mu_1)(\bar{\sigma}^2 - \mu_2) \geq 0\ , \tag{3.22}$$

where $\mu_{1,2}$ are the roots of the left hand side of inequality (3.21) as a quadratic equation that can be founded by its discriminant,

$$\mu_{1,2} = \frac{1}{\lambda^3}[27 - 18\lambda - \lambda^2 \pm \sqrt{(27 - 18\lambda - \lambda^2)^2 - 64\lambda^3}]. \tag{3.23}$$

The sign of discriminant expresses the type of roots which can be real or complex (μ_1 corresponds to the sign "–," and μ_2 to the sign "+"). Analyzing the stability of plasma perturbations in this regard shows that the necessary and sufficient condition of gradient drift instability can be expressed as [30]:

$$\begin{aligned} \sigma^2 &> \mu_1, && \text{for } \lambda \leq 0 \\ \mu_1 < \bar{\sigma}^2 &< \mu_2, && \text{for } 0 < \lambda < 1. \end{aligned} \tag{3.24}$$

Figure (3.19) shows the stability diagram of dispersion relation (3.17) in the plane of $\bar{\sigma}^2 - \lambda$ for corresponding plasma parameters $B_0 = 180$ G, $E_0 = 2$ V/m. The red line shows μ_1, blue line shows μ_2 and black line shows the curve $\bar{\sigma}^2 = \alpha\sigma/(1 - \lambda)$. The corresponding curves are for the plasma parameters that are mentioned in the caption of the figure. It should be noted that λ and $\bar{\sigma}^2$ are the function of k_y therefore μ_1 and μ_2 implicitly are function of k_y.

In Fig. (3.19b), as k_y grows along the black curve from the left to the right, there is a cut-off of the short-wavelength modes (yellow point) occurs with the maximal possible k_{ymax} defined by the relation $\alpha_0\sigma_0/(1-\lambda) = \mu_2$, at the intersection with the μ_2 instability boundary. This point with $\bar{\sigma}^2 = 2.36 = (k_y v_E/\omega_{LH})^2$ has good consistency with the maximum $k_y v_E/\omega_{LH} = 1.53$ of island instability in Fig. (3.19a). It is clear that this island instability regime starts from $\bar{\sigma}^2$ more than zero, and its cut off occurs in the lower $\bar{\sigma}^2$ which extends the instability region between two values of $k_y v_E/\omega_{LH}$.

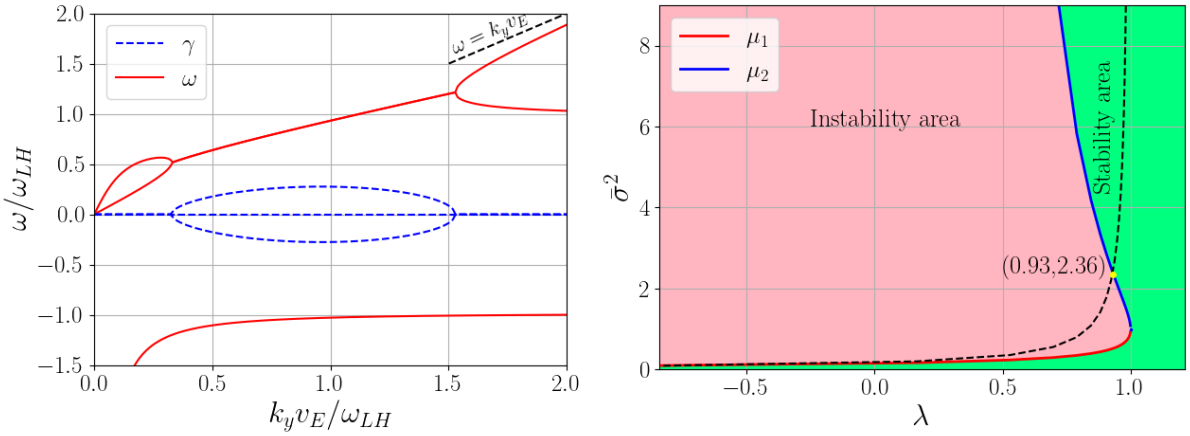

(a) **(b)**

Figure 3.19: (a) Frequency and growth rate of purely azimuthal dispersion relation of the lower-hybrid instability in a cold plasma, (b) Stability diagram in the plane $\bar{\sigma}^2 - \lambda$. Parameters for this figure are: $n = 1 \times 10^{17}$ m^{-3}, $m_{xenon} = 2.18e - 25$ kg, $k_x = 0.0$ m^{-1}, $L_n = -0.05$ m.

3.5 Summary

We have compared the linear stability of LHDI from the fluid models with the kinetic model through solving corresponding dispersion relations. We show that for larger values of the azimuthal wavevector, the Simon-Hoh instability loses its consistency with the kinetic model as expected. On the other hand, we indicate that the advanced fluid dispersion model [20] that is based on the electron gyroviscosity and includes finite Larmore radius has a good consistency with the kinetic model except for the electric field strength at the order of 100 V/m. Comparing eigenmodes of the advanced fluid model with the kinetic one for Hall thruster parameters in two regions of the Hall channel reveals good consistencies between the fluid and the kinetic models. We have found a new regime of lower-hybrid modes for the cold plasma that occurs not only for the strong field but also for the low field subject to the $v_e/|L_n|\Omega_{ci} \approx 0.1$.

Chapter 4

Particle-in-cell simulations

In this chapter, I review the principles ideas of the PIC algorithm, and in the next chapter, I will give the actual results of PIC simulation of Buneman type instability.

4.1 Review of basic Particle-In-Cell algorithms

Computer simulations are indispensable tools to study and predict the evolution of complex plasma systems where non-linearity and many degrees of freedom are essential. Collisionless plasma as a system of charged particles that interact through the electromagnetic field is modeled by coupling Vlasov and Maxwell equations to describe the evolution of the phase-space distribution function. In this regard, there are two main approaches: the Eulerian and Lagrangian approaches. The Lagrangian method uses a moving frame, while the Eulerian process uses a fixed frame to solve the equations. Particle-in-cell (PIC) methods solve Maxwell equations on a fixed grid (Eulerian approach) and represent distribution function by moving particles through Newton's law (Lagrangian approach). These particle trajectories are characteristics of the corresponding Vlasov equation.

There is another simulation method for plasma which is called the Vlasov method. Instead of following the particle trajectories, this method solves the Maxwell-Vlasov equations directly on a stationary grid of phase space (Eulerian approach). It has proven to be a low-noise alternative to the PIC method for some specific problems.

Since PIC simulations are the most widely used computational tools in plasma physics, I will review the general idea of collisionless PIC algorithms in the following sections.

4.2 PIC algorithm

The core of a PIC code consists of two coupled solvers. The first one is "particle pusher," which moves charged particles in space under the influence of electromagnetic fields and then calculates the density and currents of particles due to their motions. The second one is "field solver," which solves Maxwell's equations using particle positions and velocities. Between these two solvers, the full collisionless behavior of a kinetic plasma can be sim-

ulated. The first step in PIC modeling is to approximate the equations with a series of algebraic equations needed for discretizing and numerical calculations. We begin this step by replacing the continuous-time and space variable with a series of discrete temporal and spatial steps covering a short period of time or space.

The applied spatial grid (mesh) in PIC codes is divided into blocks called cells. The cell corners are known as grid points (nodes), and the spatial distance between nodes is called the spatial step and denoted by Δx. Nodes are shared among neighbor cells. The cells can have an arbitrary shape based on problem configuration, but they should not overlap. Since the computational resources are limited, it is impossible to resolve the infinite amount of available information in the continuous real world. Therefore discretizing space and time and choosing these intervals based on the physical and the computational limitations are some of the remarkable points in simulation methods.

The standard procedure of PIC codes can be briefly summarized in Fig. (4.1) for completeness.

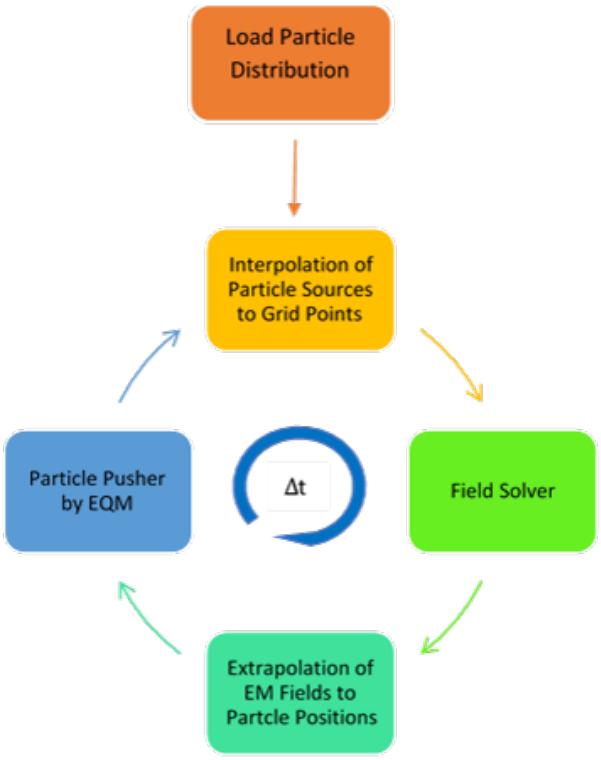

Figure 4.1: The algorithm of the main cycle.

1. Calculation of electromagnetic sources (ρ and $\mathbf{j}$) from macro-particle in the grid points by interpolating methods.

2. Calculation of electromagnetic fields in the grid points using $\mathbf{j}$ and ρ from the previous step.

3. Calculation of electromagnetic fields in the macro-particle position by extrapolating methods.

4. Integration of equation of motion (EQM) and updating the position and velocity of macro-particle in time.

This cycle is repeated until a desired time. The study of particle evolution in simulation models is explained in detail in the following sections.

4.2.1 Initial loading of particles

Placing particles in $\mathbf{x}$, $\mathbf{v}$ at $t = 0$ and injecting or removing particles during a simulation run, start with prescribed density in space $n_0(x)$ and inlet velocity distribution function in velocity $f_0(v)$. The formal process for converting $n_0(x)$ and $f_0(v)$ into $(x, v)_i$ of the particles is called inversion of the cumulative density [31] that will be explained in detail in chapter 5.

In most cases, the density function of particles is uniform. Therefore, we can load particles in the simulation box in different ways based on simulation conditions. We categorize them into three major groups:

- Uniform loading in x and random loading of Gaussian in v.
- Uniform loading in x and uniform loading of Gaussian in v.
- Uniform loading in x and non-random loading of Gaussian in v.

The first model of loading particles is too noisy and can not be acceptable, particularly in observing low-level physics. The second model is called multi beams, and the last model is called quiet start and will be discussed in detail in the next chapter.

Regarding the number of injected particles from density to simulation box, we define the expression of macro-particles (super-particles) instead of individual particles. Each macro-particle consists of N_w particles, where N_w is called the weight of the macro-particle. Since the acceleration factor in the Lorentz force depends only on the charge-to-mass ratio, the trajectory which a super-particle will follow is the same as a real particle. Moreover, since the number of calculated particles from an experimental plasma density is out of the scope of the computer's capabilities, we obtain useful information from one or two-dimensional simulations without the need to perform three-dimensional ones. We are often interested in the collective behavior of plasma at a wavelength longer than the Debye length, therefore if the number of particles in the Debye cube of confined fusion plasma is $N_D = n\lambda_D^3 = 10^6$, for 1D-simulation, we use $N_{1D} = n\lambda_D = (10^6)^{1/3} = 10^2$ and for 2D-simulation is $N_{2D} = n\lambda_D^2 = (10^6)^{1/2} = 10^3$ [31].

In fact, in a 1D simulation, a charged particle is like a plane that moves perpendicularly to its normal and has a plate mass and charge. In a 2D simulation charged particle is like a rod with a rod mass and charge. The charge to mass ratio of these plates and rods in the equations of motion has the same absolute value.

$$\text{In 1D-model}: \frac{\rho_{sheet}}{m_{sheet}} = \frac{q}{m},\ m_{sheet} = [\text{kg/m}^2],\ \rho_{sheet} = [\text{c/m}^2],$$
$$\text{In 2D-model}: \frac{\rho_{nod}}{m_{nod}} = \frac{q}{m},\ m_{nod} = [\text{kg/m}],\ \rho_{nod} = [\text{c/m}].$$

4.2.2 Interpolation and extrapolation

For calculating the electric and magnetic fields on the grid points, the charge and current of each particle need to be deposited onto the grid; this process is called interpolation. Conversely, to determine the force on a particle, we require knowledge of the electric and magnetic field at the position of particles x. Since the electromagnetic fields are known only at grid points, determining the fields at an arbitrary location x requires a further interpolation step called extrapolation. For avoiding self forces and conserving particle momentum, it is recommended to use an identical interpolation and extrapolation scheme [32, 33].

There are different interpolation schemes. The simplest one is the zero-order interpolating where the number of particles is counted within distance $\pm\Delta x/2$ (one cell width) about the jth grid point and assign that number to that point, $N(j)$ Fig. (4.2). In one dimension it is simply $n_j = N(j)/\Delta x$ and the common name for this scheme is nearest grid point (NGP) assignment. This interpolation scheme can produce an effective rectangular particle shape function $S(x)$ of width Δx Fig. (4.2),

$$S_0(x) = \begin{cases} \frac{1}{\Delta x}, & \text{If } |x|<\Delta x/2, \\ \\ 0, & \text{otherwise.} \end{cases} \tag{4.1}$$

The first-order interpolation scheme that is called cloud-in-cell (CIC), in one dimension, divides the charge q_i of particle i, at position x_i, amongst its two nearest grid points j and $j+1$, at the positions X_j and X_{j+1}, respectively, using linear interpolation (Fig. 4.2). In this scheme, we no longer view the particles as point particles; rather, we consider them as a finite-sized particle [31],

$$q_j = q_i \frac{X_{j+1} - x_i}{\Delta x}, \tag{4.2}$$
$$q_{j+1} = q_i \frac{x_i - X_j}{\Delta x}. \tag{4.3}$$

The linear interpolation scheme can also be seen to produce an effective triangular particle shape function $S(x)$ of width $2\Delta x$ Fig. (4.2), [32, 33, 34].

$$S_1(x) = \frac{1}{\Delta x}\begin{cases} 1-|x|/\Delta x, & \text{If } |x|<\Delta x, \\ 0, & \text{otherwise.} \end{cases} \tag{4.4}$$

As the super-particle moves through the grid, it will contribute to the grid much more smoothly than the zero-order interpolation and contribute much less noise. This is the preferred interpolation function used throughout many simulations. A higher-order interpolation scheme using a quadratic or Gaussian function can also be used to further reduce the noise in the density and field at the cost of increased computation [31].

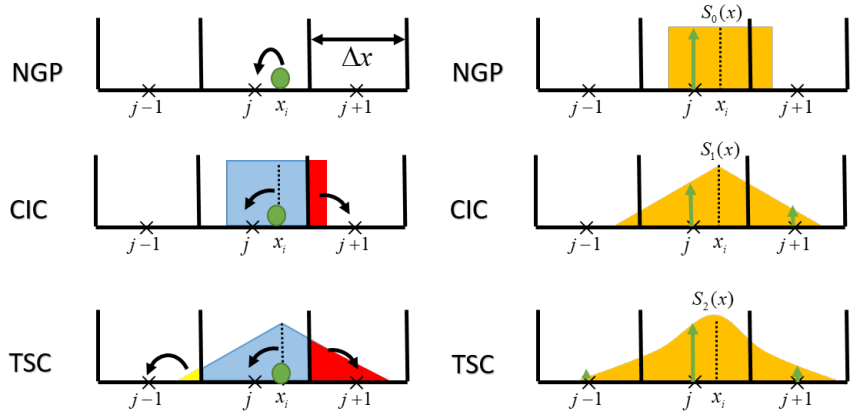

Figure 4.2: Weighting scheme in 1D.

The amount of charge and current density assigned to the grid point X_j by a particle located at x_i is determined by the value of $S(X_j - x_i)$. In particular, for a total of N_p particles, each having the coordinate and velocity x_i and v_i respectively, the total contribution to the charge and current density at X_j is,

$$\rho_j = \sum_i^{N_p} N_w q_i S(X_j - x_i), \tag{4.5}$$

$$J_j = \sum_i^{N_p} N_w q_i v_i S(X_j - x_i), \tag{4.6}$$

where N_w is the weight of the macro-particle.

In the NGP scheme (zero-order interpolation) of a 2D simulation, the whole charge of the particle belongs to the center of the cell where the particle is located. In fact, each cell is the center of the point of the mesh. In this method, whenever the particle passes through the edges of the cell, its charge is given to the next cell. On the other hand, the first-order interpolation scheme, which is referred to (CIC), divides the charge q_i of particle i, at position x_i, amongst its four nearest grid points by using bilinear interpolation.

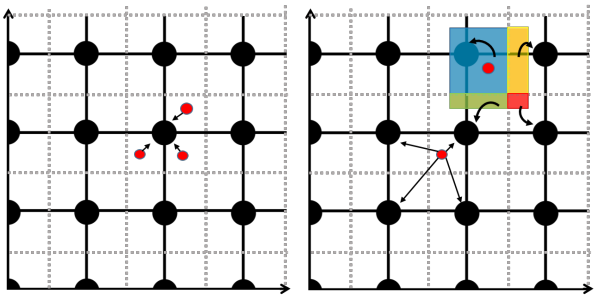

(a) **(b)**

Figure 4.3: (a) NGP interpolation scheme in 2D (b) CIC interpolation scheme in 2D.

Now we use a similar scheme to the one used for interpolating the particle charge to the grid as an extrapolation of the calculated electric field on the grid back to the position of the particles. For example, in CIC interpolation in 1D, the electric field at the particle's position x_i is evaluated from the electric field stored at the two nearest grid points to that particle [31]:

$$E_x(x_i) = E_{x(j)}\left[\frac{X_{j+1} - x_i}{\Delta x}\right] + E_{x(j+1)}\left[\frac{x_i - X_j}{\Delta x}\right]. \tag{4.7}$$

4.2.3 Field solver

The first step in discretizing the mathematical model approximates the equations with a series of algebraic equations needed for numerical calculations. In this step, the continuous-time and space variables are replaced with a series of discrete temporal and spatial phases, each covering a short time or space.

As mentioned in the previous section, charge and current density from the particles is accumulated on the grid. This charge and current density on the grid then provide the sources term in Maxwell's equation to obtain the electric and magnetic fields. Here we consider two outlooks (electrostatic and electromagnetic) on the plasma problem.

Electrostatic

In the electrostatic problem, $\nabla \times \mathbf{E} = -\partial \mathbf{B}/\partial t \approx 0$, and solving Maxwell's equation, for one-dimensional simulation becomes these two differential equations to be solved,

$$\mathbf{E} = -\nabla\phi \text{ and } \nabla \cdot \mathbf{E} = \frac{\rho}{\epsilon_0}, \tag{4.8}$$

which are combined to obtain Poisson's equation,

$$\nabla^2\phi = -\frac{\rho}{\epsilon_0}. \tag{4.9}$$

One approach for solving Poisson's equation numerically with the known boundary conditions is the finite difference and using charge density on the grid points called "Direct

solver"

$$\frac{\phi_{(j-1)} - 2\phi_{(j)} + \phi_{(j+1)}}{\Delta x^2} = -\frac{\rho_j}{\epsilon_0} \rightarrow A\phi = -\frac{\Delta x^2}{\epsilon_0}\rho, \tag{4.10}$$

where A is the coefficient matrix. Then calculate the electric field

$$E_j = \frac{\phi_{(j-1)} - \phi_{(j+1)}}{2\Delta x}. \tag{4.11}$$

A prevalent and powerful approach recommended for a periodic system is to use the fast Fourier transform (FFT) based on the discrete Fourier transform for all grid quantities. This approach provides spatial-spectral information related to plasma theory and increases control over the spectrum of field quantities [31]. In the first sequence of this method, density is expressed in terms of its Fourier transform:

$$\rho(k) = \frac{1}{\sqrt{2\pi}} \int \rho(x) e^{-ikx} dx. \tag{4.12}$$

Then by using the Poisson's equation that is diagonalized in k-space, the potential can be calculated in k-space,

$$\phi(k) = \frac{\rho(k)}{\epsilon_0 k^2}. \tag{4.13}$$

The next step is, taking the inverse Fourier transform of $\phi(k)$, to obtain $\phi(x)$ and then $E(x)$ through Gauss's law,

$$\phi(x) = \frac{1}{\sqrt{2\pi}} \int \phi(k) e^{ikx} dk. \tag{4.14}$$

Constructing a dispersion diagram is one of the advantages of using the Fourier transform. This is done by transforming $E(x)$ into $E(k)$ at each time interval. Once a series of $E(k)$ at each time interval is obtained, the Fourier transform is applied in the time domain of $E(x)$ to obtain $E(k)$, which is in the frequency domain. Thus, the classical $\omega - k$ diagram can be constructed and used to study wave dispersion, and growth rate properties [31].

Electromagnetic

Electromagnetic programs are more complicated than electrostatic programs and generally more expensive. For the complete electromagnetic program, we must consider the set of Maxwell's equations. This feature of Maxwell's equations that it can be written as a hyperbolic system of partial differential equations gives them access to robust and stable conservative techniques for numerical solutions.

The fields are integrated forward using time derivatives by Faraday and Ampere-

Maxwell laws,

$$\frac{\partial \mathbf{B}}{\partial t} = -\nabla \times \mathbf{E}, \tag{4.15}$$

$$\mu_0 \epsilon_0 \frac{\partial \mathbf{E}}{\partial t} = -\nabla \times \mathbf{B} - \mu_0 \mathbf{j}. \tag{4.16}$$

Time derivatives of $\mathbf{B}(\mathbf{E})$ on the left-hand side, following the $\mathbf{E}(\mathbf{B})$ field occurring on the right-hand side, suggest the use of the leap-frog scheme for time and spatial integration which has a second-order accuracy and shown schematically in Fig. (4.4) where Δt is time step. We can show the performance of this schema in one dimension, in the space-time

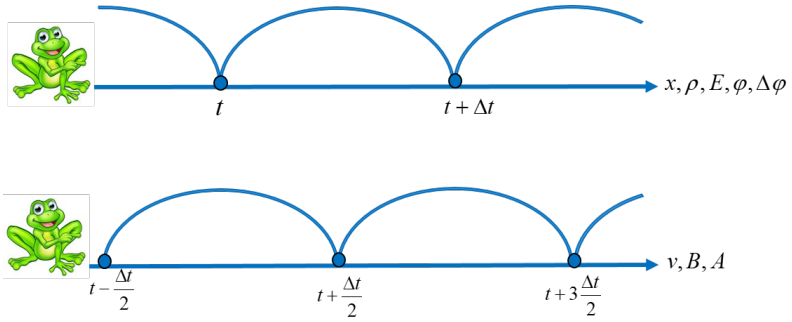

Figure 4.4: Temporal outline of field and particle quantities used in leap-frog integration of Maxwell's equations. Charge density, scalar potential, electric field and position are advanced in actual time steps while current, vector potential, magnetic filed and velocity are advanced in half time steps. The figure is adopted from [31].

network (Fig. 4.5) as follows: The time derivative becomes,

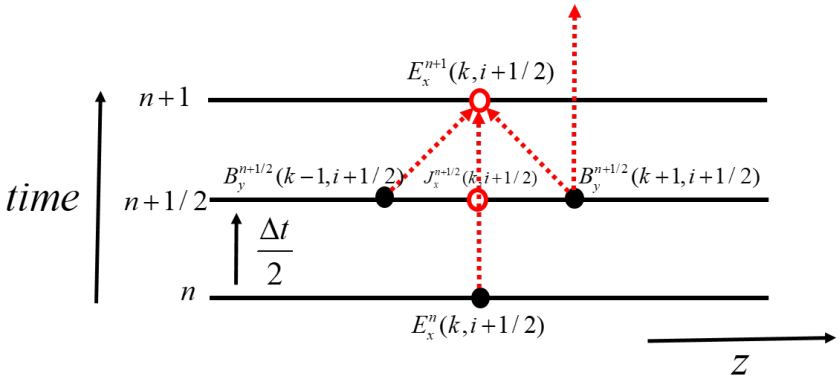

Figure 4.5: Space-time network. Spacial layout shows the location of the TM field components and time layout shows time-stepping of E_x by using J_x and B_y.

$$(\partial_t E_x)^{n+1/2}_{k,i+1/2} = \frac{E_x^{n+1}(k, i+1/2) - E_x^{n}(k, i+1/2)}{\Delta t}, \tag{4.17}$$

where $E_x^n(k, i+1/2) = E_x(k\Delta z, [i+1/2]\Delta x, , n\Delta t)$.

The differenced Maxwell Eq. (4.16), (4.15) for TM components are,

$$(\partial_t B_y)^n_{k+1/2,i+1/2} = -(\partial_x E_z - \partial_z E_x)^n_{k+1/2,i+1/2}, \tag{4.18}$$

$$(\mu_0\epsilon_0\partial_t E_x)^{n+1/2}_{k,i+1/2} = (-\partial_z B_y - \mu_0 J_x)^{n+1/2}_{k,i+1/2}, \tag{4.19}$$

$$(\mu_0\epsilon_0\partial_t E_z)^{n+1/2}_{k+1/2,i} = (-\partial_x B_y - \mu_0 J_z)^{n+1/2}_{k+1/2,i}. \tag{4.20}$$

For instance, from the Eq. (4.17), we can expand Eq. (4.19) to,

$$\mu_0\epsilon_0\left(\frac{E_x^{n+1}(k,i+1/2) - E_x^n(k,i+1/2)}{\Delta t}\right) = \\ -\left(\frac{B_y^{n+1/2}(k+1,i+1/2) - B_y^{n+1/2}(k-1,i+1/2)}{\Delta z}\right) - \mu_0 J_x^{n+1/2}(k,i+1/2).$$

The code first advances **B** in time and then **E**, as shown in Fig. (4.4). At each step, the new values overwrite old values.

4.2.4 Particle pusher

In PIC simulation, the Newton-Lorentz equation of motion governs the dynamics of the particles and is integrated in time. The position x_i and the velocity v_i of the ith particle are then updated [33, 31]

$$\frac{d\mathbf{v}_i}{dt} = \frac{q[\mathbf{E}(x_i,t) + \mathbf{v}_i \times \mathbf{B}(x_i,t)]}{m}, \tag{4.21}$$

$$\frac{d\mathbf{x}_i}{dt} = \mathbf{v}_i. \tag{4.22}$$

Here $\mathbf{B}(x_i,t)$ and $\mathbf{E}(x_i,t)$ are magnetic and electric fields at the position of particle i, at time t. The centered-difference technique is used to solve these equations numerically,

$$\frac{\mathbf{v}_i^{t+\Delta t/2} - \mathbf{v}_i^{t-\Delta t/2}}{\Delta t} = \frac{q}{m}\left[\mathbf{E}(x_i,t) + \frac{\mathbf{v}_i^{t+\Delta t/2} - \mathbf{v}_i^{t-\Delta t/2}}{2} \times \mathbf{B}(x_i,t)\right]. \tag{4.23}$$

Updating the particle velocity

There are two standard methods for updating the particle velocities in the simulation called the Buneman and Boris methods. The first method (Buneman, 1967) subtracts the drift velocity $\mathbf{E}\times\mathbf{B}/B_0^2$ from v_i,

$$\mathbf{v}'_{old} = \mathbf{v}_i^{t-\Delta t/2} - \frac{\mathbf{E}\times\mathbf{B}}{B_0^2}, \tag{4.24}$$

$$\mathbf{v}'_{new} = \mathbf{v}_i^{t+\Delta t/2} - \frac{\mathbf{E}\times\mathbf{B}}{B_0^2}. \tag{4.25}$$

By substituting velocity in the Eq. (4.21), we will have only one rotation for $v_\perp$ and free acceleration for $v_\parallel$,

$$\frac{\mathbf{v}'_{new} - \mathbf{v}'_{old}}{\Delta t} = \frac{q}{m}\left[\mathbf{E}_\parallel(x_i,t) + \frac{\mathbf{v}'_{new} + \mathbf{v}'_{old}}{2} \times \mathbf{B}(x_i,t)\right]. \tag{4.26}$$

Another method separates the electric and magnetic forces (Boris, 1970). By defining two times t^- and t^+, we can rewrite the Newton-Lorentz equivalent in the form that only electric filed effect on the particles,

$$\mathbf{v}_i^{\,t-\Delta t/2} = \mathbf{v}^- - \frac{q\mathbf{E}(x_i,t)}{m}\frac{\Delta t}{2}, \tag{4.27}$$

$$\mathbf{v}_i^{\,t+\Delta t/2} = \mathbf{v}^+ + \frac{q\mathbf{E}(x_i,t)}{m}\frac{\Delta t}{2}. \tag{4.28}$$

When substituting the above equation into the equation (4.23), Then $\mathbf{E}$ cancel entirely, and the only velocity vector which rotates with a specific angle that depends on the electric field remain.

$$\frac{\mathbf{v}^+ - \mathbf{v}^-}{\Delta t} = \frac{q}{2m}(\mathbf{v}^+ + \mathbf{v}^-) \times \mathbf{B} \tag{4.29}$$

Therefore, the process of calculation of particle velocity is briefly as follows:

1. In the first half of time step $\Delta t/2$, electric field update velocity from $\mathbf{v}_i^{\,t-\Delta t/2}$ to $\mathbf{v}^-$ (**Half acceleration**).

2. Then magnetic field rotate $\mathbf{v}^-$ to obtain $\mathbf{v}^+$ about an axis parallel to $\mathbf{B}$, (**Rotation**)(Fig. (4.6)).

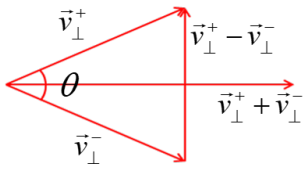

Figure 4.6: Rotation from $\mathbf{v}_\perp^-$ to $\mathbf{v}_\perp^+$. Summation and difference of these two vectors are perpendicular to each other. The figure is adopted from [31].

where angle of rotation can be calculated by,

$$|\tan(\frac{\theta}{2})| = \frac{|\mathbf{v}_\perp^+ - \mathbf{v}_\perp^-|}{|\mathbf{v}_\perp^+ + \mathbf{v}_\perp^-|} = \frac{qB_0}{m}\frac{\Delta t}{2}. \tag{4.30}$$

3. In the last half of time step $\Delta t/2$, electric field update velocity from $\mathbf{v}^+$ to $\mathbf{v}_i^{\,t+\Delta t/2}$ (**Half acceleration**).

As mentioned in step 2, the magnetic field provides purely rotation of the velocity from $\mathbf{v}^-$ to $\mathbf{v}^+$ while the magnitude of the vector remains unchanged. Boris adds two more

steps to maintain the immutability of magnitude (Fig. 4.7).

$$\mathbf{v}' = \mathbf{v}^- + \mathbf{v}^- \times \mathbf{t}, \tag{4.31}$$

$$\mathbf{v}^+ = \mathbf{v}^- + \mathbf{v}' \times \mathbf{s}, \tag{4.32}$$

$$\mathbf{t} = \frac{q\mathbf{B}\Delta t}{2m}, \text{ and } \mathbf{s} = \frac{2\mathbf{t}}{(1+t^2)}, \tag{4.33}$$

where $\mathbf{v}'$ is an intermediate velocity. The parameter $\mathbf{s}$ is a scaled version of $\mathbf{t}$ to satisfy

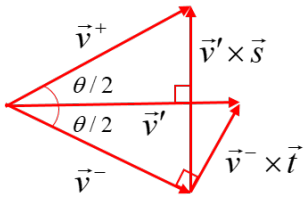

Figure 4.7: Rotation of $\mathbf{v}^-$ to $\mathbf{v}^+$. First $\mathbf{v}^-$ is advanced by vector $\mathbf{t}$ to produce intermediate vector $\mathbf{v}'$ where its advancement by vector $\mathbf{s}$ results in $\mathbf{v}^+$. The velocities are projections of the total velocities onto the plane perpendicular to B. The figure is adopted from [31].

this equality $|\mathbf{v}^-| = |\mathbf{v}^+|$. This method is proper wherever velocities and positions are in the plane normal to the uniform magnetic field.

Updating the particle position

The standard leapfrog technique is used to update the position of a particle by using the particle's velocity. The leapfrog technique provides a method to numerically integrate Eq. (4.22) in time, which is second-order accurate,

$$\frac{\mathbf{x}_i^{t+\Delta t} - \mathbf{x}_i^t}{\Delta t} = \mathbf{v}_i^{t+\Delta t/2} \rightarrow \mathbf{x}_i^{t+\Delta t} = \mathbf{x}_i^t + \mathbf{v}_i^{t+\Delta t/2}\Delta t. \tag{4.34}$$

4.2.5 Stability of the numerical techniques

Selecting cell size Δx and time step Δt play an essential role in the stability of the simulation method. These values should be chosen so that the numerical errors resulting from the numerical techniques employed to solve the differential equation do not increase over time. Because in this case, the order of errors will be more than the order of the answer and disrupt the simulation method [35]. Nonphysical instabilities generally arise due to temporal or spatial aliasing of the plasma dynamics due to improper choices of the time step and the cell sizes [33, 34].

Selection of the cell size

A key requirement for selecting Δx is that, it should be much smaller than the smallest wavelengths in the system. Otherwise, the fields, forces, and phenomena at length less than a grid cell are not observable and will cause many errors in calculations. Plasma is non-neutral only on length scales smaller than the Debye length and the cell volume should be smaller than volume of the Debye sphere,

$$\Delta x \Delta y \Delta z < \frac{4\pi\lambda_D^3}{3}, \tag{4.35}$$

where $\lambda_D = \sqrt{\epsilon_0 K_B T_e/(n_e q_e^2)}$ and K_B is Boltzmann's constant. Similarly, for 1D simulation, the spatial step Δx cannot be much larger than the Debye length λ_D,

$$\Delta x < \lambda_D. \tag{4.36}$$

Also, since we are interested in observing the collective behavior of plasmas, the system length must be larger than Debye length $L > \lambda_D$. Depending on the problem, different types of mesh, such as uniform or nonuniform and curved or straight meshes, can be used.

Selection of number of particles in Debye length

The plasma oscillation period is the fundamental time scale associated with collective effect,

$$\tau_p = \frac{2\pi}{\omega_p} = \sqrt{\frac{\pi m}{ne^2}}. \tag{4.37}$$

It can be shown roughly [31] that the particle-particle collision time τ_c is related to the characteristic time for collective oscillations by

$$\frac{\tau_p}{\tau_c} = \frac{K}{N_D}, \tag{4.38}$$

where K is approximately constant of the order of unity, and N_D is the number of particles in the Debye sphere. Therefore, as the N_D becomes large ($N_D >> 1$), the collision time becomes long, the collective effect becomes the primary phenomena of interest, and the impact of collisions is of secondary importance. As a result, such a physical system can be described by a particle-field model.

Selection of the time step

Discretizing the governor equation in the PIC method is based on the centered difference scheme in space and the leapfrog method in time. The stability of the leapfrog scheme can be illustrated for particles in simple harmonic motion [36]:

$$\frac{\partial^2 x}{\partial t^2} = -\omega_0^2 x. \tag{4.39}$$

Finite differencing using a centre difference (leapfrog) gives

$$\frac{x^{t+\Delta x} - 2x^t + x^{t-\Delta t}}{\Delta t^2} = -\omega_0^2 x^t, \tag{4.40}$$

where the solution are of the form

$$x^t = C \exp(-i\omega t), \tag{4.41}$$

$$x^{t+\Delta t} = C \exp(-i\omega(t + \Delta t)), \tag{4.42}$$

we get this result by using Euler 's identity,

$$\sin\left(\frac{\omega \Delta t}{2}\right) = \pm \frac{\omega_0 \Delta t}{2}. \tag{4.43}$$

For $\omega_0 \Delta t > 2$, ω has an imaginary component that grows or decays exponentially with time and shows numerical instability [36].

Based on the above-simplified analysis, we deduce that for maintaining the stability of the leapfrog scheme, we require

$$\omega_p \Delta t < 2, \tag{4.44}$$

where ω_p is the highest natural frequency of the plasma. The experience in PIC simulation reveals that for reasonable accuracy and stability, the applicable criteria is $\omega_p \Delta t < 0.5$ [33].

To investigate the stability condition of Maxwell equations solved by the second-order accuracy centered difference scheme in space and leapfrog method in time, we consider the propagation of the following electromagnetic wave in a vacuum. We consider wave equation in one dimension [36],

$$\frac{\partial^2 \Psi}{\partial t^2} = c^2 \frac{\partial^2 \Psi}{\partial x^2}, \tag{4.45}$$

For sinusoidal wave,

$$\Psi(x, t) = \exp(i(\omega t - kx)), \tag{4.46}$$

after discretization by centred difference scheme, we have

$$\Psi_j^{t+\Delta t} = \left(c\frac{\Delta t}{\Delta x}\right)^2 (\Psi_{j+1}^t - 2\Psi_j^t + \Psi_{j-1}^t) + 2\Psi_j^t - \Psi_{j+1}^{t-\Delta t}, \tag{4.47}$$

$$\Psi_j^t = \exp(i(\omega t - \tilde{k} j \Delta x)), \tag{4.48}$$

where $c = 1/\sqrt{\epsilon_0 \mu_0}$ is the speed of light and $\tilde{k}$ is numeric wave number. By putting the

discretization form of a sinusoidal wave in the wave equation, we will have,

$$\frac{\exp\left(i\omega\Delta t\right)+\exp\left(-i\omega\Delta t\right)}{2}=\left(c\frac{\Delta t}{\Delta x}\right)^{2}\left(\frac{\exp\left(i\tilde{k}\Delta x\right)+\exp\left(-i\tilde{k}\Delta x\right)}{2}-1\right)+1. \quad (4.49)$$

Therefore we drive the numerical dispersion relation of the light mode as follows:

$$\cos\left(\omega\Delta t\right)=\left(c\frac{\Delta t}{\Delta x}\right)^{2}\left(\cos\left(\tilde{k}\Delta x\right)-1\right)+1. \quad (4.50)$$

As it is clear from Fig. (4.8), for $c\Delta t/\Delta x=1$ and $\Delta t\rightarrow 0,\Delta x\rightarrow 0$, numeric wave number $\tilde{k}=\omega/c=k$ and for the case $c\Delta t/\Delta x=0$ the limit state of numerical dispersion relation becomes,

$$1-\frac{(\omega\Delta t)^{2}}{2}+...=(c\frac{\Delta t}{\Delta x})^{2}(\cos\left(\tilde{k}\Delta x\right)-1)+1, \quad (4.51)$$

$$\frac{(\omega\Delta t)}{c}=\sqrt{2(1-\cos\left(\tilde{k}\Delta x\right))}. \quad (4.52)$$

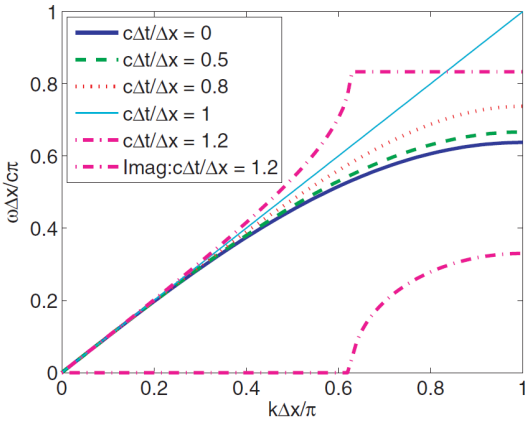

Figure 4.8: Vacuum dispersion curve for leapfrog difference scheme for wave equation. For $c\Delta t/\Delta x=1.2$, both the real and imaginary parts are shown. The figure is adopted from [36].

For the case $c\Delta t/\Delta x>1$ there is an imaginary root that grows dramatically as follows:

$$\frac{\exp\left(\omega_{i}\Delta t\right)+\exp\left(-\omega_{i}\Delta t\right)}{2}=\left(c\frac{\Delta t}{\Delta x}\right)^{2}\left(\frac{\exp\left(i\tilde{k}\Delta x\right)+\exp\left(-i\tilde{k}\Delta x\right)}{2}-1\right)+1, \quad (4.53)$$

$$\frac{\omega_{i}\Delta x}{c}=\frac{\Delta x}{c\Delta t}\cosh^{-1}\left[(c\frac{\Delta t}{\Delta x})^{2}(\cos\left(\tilde{k}\Delta x\right)-1)+1\right]. \quad (4.54)$$

where $\cos\left(\tilde{k}\Delta x\right)$ becomes more than 1, for $\tilde{k}\Delta x>\cos^{-1}\left[1-2\left(\frac{\Delta x}{c\Delta t}\right)^{2}\right]$. That's why it

should always be $c\Delta t/\Delta x < 1$ which is called the CFL condition[1]. This condition for multi dimension is $\Delta t \leq \frac{1}{c}[\sum_i \frac{1}{(\Delta x_i)^2}]^{-1/2}$, where i shows coordinate and Δx_i is spatial distance in each direction [31].

Generally, The most striking point to note based on Courant condition is that for maintaining the stability and accuracy of any explicit discrete scheme, the distance that any information travels during the timestep length within the mesh must be lower than the distance between mesh elements [37]. In other words, information from a given cell or mesh element must propagate only to its immediate neighbors. In the numerical investigation of electrostatic plasma phenomena, the maximum speed of the particle, which can be its thermal velocity, substitutes the speed of light $\Delta t < \Delta x/v_{te}$.

4.3 Parallelization of the PIC code

One of the major drawbacks of plasma simulation that makes them computationally expensive and unfeasible is the existence of millions of individual charged particles [33]. This problem nowadays has been alleviated by the advent and readily availability of high-performance computing and parallel computing environments [33]. Message Passing Interface (MPI) is used to increase the PIC code's performance by the particle decomposition technique that allowed our simulation code to run on distributed memory systems. According to the Ref. [38] in this technique, the main process performs initial distribution over velocity and coordination for all particles and then uniformly distributes the particles between the client processes. During the primary cycle of simulations, each client process advances its particles and calculates charge density distribution due to these particles. Finally, the main process collects the charge density distributions from all client processes, solves Poisson's equation, sends the potential profile back to the client processes, and performs the diagnostic output.

[1] Courant–Friedrichs–Lewy condition

Chapter 5

PIC simulation of unmagnetized and magnetized Buneman instability

In this chapter, I study the linear and nonlinear aspects of the simple case of Buneman instability in magnetized and unmagnetized plasma through 1D-PIC simulations. Therefore I start with theoretical description of the Buneman instability in section (5.1). Then in section (5.2) I analyze the effect of noise in linear stage of PIC simulations of the Buneman instability in unmagnetized plasmas in low drift regime. In Section (5.3) I move forward into two aspects of the nonlinear stage of the Buneman instability in unmagnetized plasma. In the Section (5.4), I review the theoretical description of magnetized Buneman instability and then in section (5.5) I present the results of 1D-PIC simulation of the magnetized Buneman two stream instability.

5.1 Buneman instability

The Buneman instability is an electrostatic instability driven by relative electrons and ions drift velocities perpendicular to a magnetic field, which occurs when this relative drift velocity of the electrons and ions surpasses the electron thermal velocity. In categorizing instabilities, Buneman instability is a reactive version of ion-acoustic instability. Considering that, the growth rate of ion-acoustic is lower than Buneman instability, and the relative streaming velocity between the ions and electrons is sufficiently less than the electron thermal speed. The transition from ion-acoustic to Buneman instability is not clearly defined, but in general, the ion-acoustic instability is a limiting case of the more general Buneman instability [39].

The importance of this system of drifting electrons perpendicular to a magnetic field is producing an ion source. The results of experimental measurements of electron cross-field transport in the Hall thruster acceleration region reveal that Buneman instability is more likely to excite this ion current [40] rather than ion-acoustic one. Because the $\mathbf{E} \times \mathbf{B}$ drift in this region was limited to the order of the electron thermal speed [41].

5.1.1 Theoretical description of the unmagnetized Buneman instability in linear regime

The dispersion relation of unmagnetized Buneman instability in simplest case is obtained by considering a beam of cold electron with $T_e = 0$ moving with velocity $\mathbf{v}_0$ through a homogeneous background of the cold ions with $T_i = 0$ and density n_0 in unmagnetized plasma $\mathbf{B} = 0$. The main condition for excitation of the Buneman instability is that the initial electron drift velocity $\mathbf{v}_0 = v_0\hat{y}$ is sufficiently larger than electron thermal velocity v_{te}, $v_0 >> v_{te}$ [4].

The continuity equation from the fluid approach for electrons and ions can be written as below:

$$m_i n_0 \frac{\partial \mathbf{v}_{i1}}{\partial t} = q_i n_0 \mathbf{E}_1. \tag{5.1}$$

$$m_e n_0 (\frac{\partial \mathbf{v}_{e1}}{\partial t} + (\mathbf{v}_0 \cdot \nabla)\mathbf{v}_{e1}) = q_e n_0 \mathbf{E}_1. \tag{5.2}$$

The momentum equation for both species are:

$$\frac{\partial n_{i1}}{\partial t} + n_0 \nabla \cdot \mathbf{v}_{i1} = 0. \tag{5.3}$$

$$\frac{\partial n_{e1}}{\partial t} + n_0 \nabla \cdot \mathbf{v}_{e1} + (\mathbf{v}_0 \cdot \nabla) n_{e1} = 0. \tag{5.4}$$

Since it is assumed that $\mathbf{v}_0$ is uniform, the term $(\mathbf{v}_{e1} \cdot \nabla)\mathbf{v}_0$ in Eq. (5.2) is dropped and the term $(\mathbf{v}_{i0} \cdot \nabla)\mathbf{v}_{i1}$ does not appear in Eq. (5.1), because it is considered that $\mathbf{v}_{i0} = 0$.

We are looking for a solution in the form of $\boldsymbol{\xi}_1 = \xi e^{i(k_y y - \omega t)}\hat{y}$ for the vector quantities and without $\hat{y}$ for scalar quantities. Therefore, the Fourier analysis and the linearization of these set of equations yields:

$$\begin{aligned} v_i &= \frac{i q_i E}{\omega m_i}, \\ v_e &= \frac{i q_e}{m_e} \frac{E}{(\omega - k_y v_0)}, \\ n_i &= \frac{i q_i n_0 k_y E}{\omega^2 m_i}, \\ n_e &= \frac{i q_e n_0 k_y E}{(\omega - k_y v_0)^2 m_e}. \end{aligned} \tag{5.5}$$

Neutrality condition $n_i = n_e$ is no longer valid since the unstable waves are high-frequency and short-wavelength plasma oscillations. Therefore, we use Poisson's equation (1.6) to

result in the dispersion relation of the Buneman instability [4],

$$1 - \frac{\omega_{pe}^2}{(\omega - k_y v_0)^2} - \frac{\omega_{pi}^2}{\omega^2} = 0, \tag{5.6}$$

where $\omega_{pe} = \sqrt{n_0 q_e^2/\varepsilon_0 m_e}$ and $\omega_{pi} = \sqrt{n_0 q_i^2/\varepsilon_0 m_i}$ are the electron and ion plasma frequencies respectively.

The instability occurs for $kv_0 < \omega_{pe}(1 + (m_e/m_i)^{1/3})^{3/2}$, with the maximum mode growth rate $\gamma = (\sqrt{3}/2)(m_e/2m_i)^{1/3}\omega_{pe}$ at $k_y \approx \omega_{pe}/v_0$, and real part of the frequency $\omega = 0.5(m_e/2m_i)^{1/3}\omega_{pe}$. Although the relative streaming velocity among electrons and ions is the crucial factor in exciting instability, in the limit of vanishing temperatures of both electron and ion, the maximum growth rate ends up being independent of the initial drift velocity, and it only relies upon the electron to ion mass ratio.

Since any natural plasma has a finite temperature, thermal effects should be considered by including kinetic theory treatment. Consider a plasma in Cartesian space where the initial equilibrium distribution for ions and electrons along the y direction can be described as two Maxwellian distributions drifting relative to each other while applying the drift velocity higher than electron thermal speed ($v_0 > v_{te}$).

By considering zeroth-order Maxwellian distribution function for the stable situation and coupling Poisson equation with the kinetic equation for the electrostatic plasma case, the dispersion relation of Buneman instability results in (Detailed in chapter 1):

$$1 - \frac{\omega_{pi}^2}{2k^2 v_{ti}^2} Z'\left(\frac{\omega}{\sqrt{2}kv_{ti}}\right) - \frac{\omega_{pe}^2}{2k^2 v_{te}^2} Z'\left(\frac{\omega - k_y v_0}{\sqrt{2}kv_{te}}\right) = 0. \tag{5.7}$$

Here $v_{ti} = \sqrt{T_{0i}/m_i}$ and $v_{te} = \sqrt{T_{0e}/m_e}$ are the ion and electron initial thermal velocities, respectively and T_{0i} and T_{0e} are the initial temperatures of ions and electrons.

Fig. (5.1) presents the numerical solution of Buneman dispersion function (5.7) for hydrogen plasma while both electrons and ions have the same temperature $T_{0i} = T_{0e} =$ 0.2 eV with density $n_0 = 1 \times 10^{17}$ m^{-3}.

It can be concluded from the graph that increasing drift velocity from $v_0 = 2v_{te}$ to $v_0 = 8v_{te}$ (which is closer to the cold plasma limit $v_0/v_{te} \gg 1$) shifts the most unstable mode toward lower wavenumber. Furthermore, the positive growth rate region becomes smaller, the growth rate diagram becomes sharper, and the maximum growth rate increases.

One point that is important to mention is that the frequency of the case $v_0 = 2v_{te}$ is larger than the growth rate over the whole wave modes, while for other cases growth rate is larger than frequency before it reaches to its peak. I discuss in the following that the low growth rate of $v_0 = 2v_{te}$ compare to the others cases makes it comparable to the noise of PIC simulation.

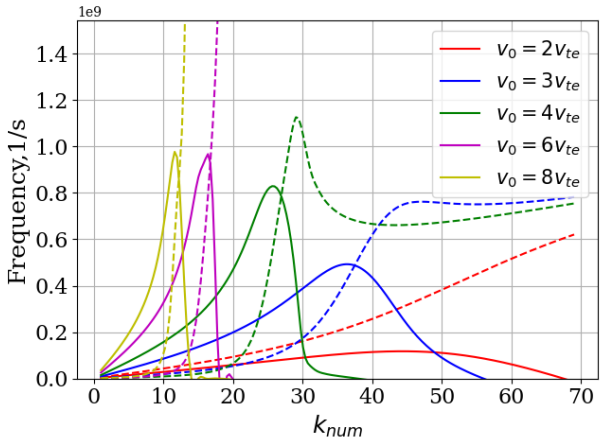

Figure 5.1: The linear growth rate (solid line) and frequency (dashed line) of Buneman dispersion relation for several drift velocities.

5.2 Role of noise in the 1D-PIC simulation of unmagnetized Buneman instability

In this section I analyze the effect of noise in PIC simulations on the occurrence of the Buneman instability in unmagnetized plasmas. The performed simulations show that the investigation of the dynamics of kinetic of Buneman instability with a low relative drift velocity of the electrons with respect to ions $v_0 = 2v_{te}$ using the conventional PIC simulation models is challenging, as it is mentioned in references [31, 32]. The cause of this difficulty is owing to the small level of signal-to-noise ratio in resolving the entire distribution function with discrete particles. Basically, using a small number of particles to represent a natural plasma, enhances collisionality and leads to random statistical fluctuations in the electric field. One possible remedy for reducing this noise is increasing the number of macro-particles N_p, as it has been proved that in random particle loading of usual PIC simulations, the statistical noise scales by $1/\sqrt{N_p}$. However, increasing the number of macro-particles for having a typical experimental plasma is impractical, and it has a high computational cost. Another solution is using quiet start methods to have a uniform particle loading in phase space, reducing the statistical noise.

In view of that, a series of highly-resolved PIC simulations with increasingly large numbers of particles per cell and implementing the quiet start initialization of particles is performed using two different PIC codes. Although increasing the number of particles and employing a quiet start method make growth rates closer to the linear growth rate calculated from the linear theory, all growth rates resulting from the simulations were larger than the analytical ones.

These investigations are a part of the teamwork of benchmarking with different Vlasov and PIC codes.

In this study, the ions are taken to be hydrogen with mass $m_i = 1$ amu, the initial plasma density is $n_0 = 1 \times 10^{17}$ m^{-3} and the initial temperature for ions and electrons is $T_{0i} = T_{0e} = 0.2$ eV which the same temperature for both spices is commonly satisfied in space plasma [42].

The roots of Eq. (5.7) for the case study of $v_0 = 2v_{te}$ are calculated by the method of Newton iteration in the Python solver that I have developed. Figure (5.2) shows this growth rate and frequency based on mode numbers. The most unstable growth rate corresponds to the mode $m = 44$. Compared with other drift velocities in Fig. (5.1), in this case, the positive growth rate region is wider, and the maximum growth rate is lower.

Table (5.1) depicts the growth rate of some selected modes from Fig. (5.2) for comparing with simulation result.

Table 5.1: Analytical growth rate.

$kL/2\pi$	$\gamma \times 10^8$ s^{-1}
30	0.90
37	1.08
44	1.17
51	1.07

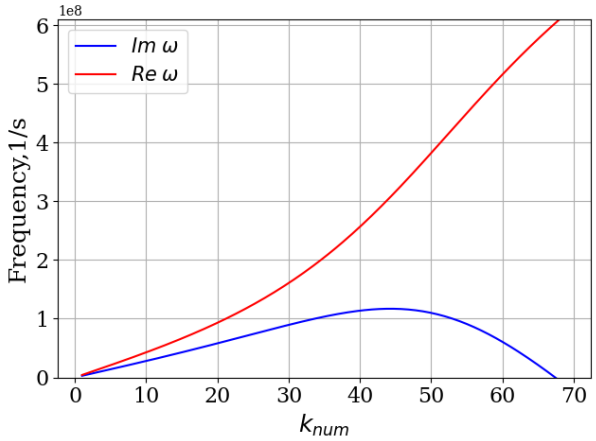

Figure 5.2: The linear growth rate (blue) and frequency (red) for the case of $v_0 = 2v_{te}$ resulted from Eq. (5.7).

5.2.1 Simulation model

Since the linear dispersion equation has complex theoretical nature and many pitfalls are associated with obtaining a correct and general solution from that equation, it seems that the safest and most general approach for solving the Vlasov-Poisson system of equations is on the computer by the numerical PIC method.

Particle-in-cell simulations for our experiments are performed with two PIC codes. The first one is the 1D2v (one spatial, two velocity space direction) electrostatic Xes1 code, which is a version of the ES1 code (described in [31]) with the support of a graphical user interface (X-Window System). ES1 code simulates plasma in a periodic domain, with electrostatic potential solver in Fourier space using Fast-Fourier transform. Integration of equations of motion is done with a popular leap-frog method and Boris scheme for magnetized particles described in chapter 4. The second one is 3D VSim [43] software from TechX corporation, which uses a powerful Vorpal computation engine and comes with the VSim composer that is a graphical user interface.

For analyzing the noise effects in time evolution and the linear and nonlinear part of Buneman instability, I have performed Particle-in-cell simulations as benchmarking of two PIC codes with three different initial distributions for particles: random Maxwellian distribution, quiet start with a well-represented Maxwellian, and quiet start with perturbing modes for our target case $v_0 = 2v_{te}$.

In this 1D1v simulation, we consider the Debye length λ_D, as the length scale and ion plasma frequency ω_{pi}, as the time scale. The general and simulation parameters I use in the simulation are as follows:

Table 5.2: Plasma parameters used for simulations.

General parameters
$L = 0.006$ m
$n_0 = 10^{17}\text{m}^{-3}$
$m_i = 1$ amu
$T_{0e} = T_{0i} = 0.2$ eV
$m_e = 9.10938356 \times 10^{-31}$ kg
$c_s = \sqrt{T_0/m_i} = 4.3928 \times 10^3$ m/s
$\lambda_D = \sqrt{\epsilon_0 T_0/q_e^2 n_0} = 1.0513 \times 10^{-5}$ m
$v_0 = 2v_{te} = 2\sqrt{T_{e0}/m_e} = 3.7511 \times 10^5$ m/s

Simulation parameters

Simulation time = 170 ns

System size = $570\lambda_D = 0.006$ m

Time step size = $10^{-4} \times \omega_{pi}^{-1} = 2.3933 \times 10^{-13}$s

Spatial grid step size = 0.2787 $\lambda_D = 2.93 \times 10^{-6}$m $\implies$ 2048 cells

Number of macro-particles per cell for each species = 1000 and 10000 PPC

The simulation time step and cell size resolve accuracy and stability by providing the practical criteria of $\omega_{pi}\Delta t < 0.5$ and $\Delta x/\lambda_D < 1$. In addition, Δt satisfies the CFL condition on the Δx grid for hypothetical velocities as large as 1.22×10^7 m/s. The typical electron velocities from the simulation are only $O(10^6)$ m/s, hence the CFL stability is ensured.

In all simulations, I use the periodic boundary condition in a system of 6 mm length, resolved by a grid of 2048 points. In addition, the periodic boundary conditions are applied in all simulations, so the number of particles is constant, and the length of the system is large enough to enable the excitation of several modes with mode numbers $m = kL/2\pi$. Furthermore, the electrons and ions have Maxwellian velocity distributions in their rest frames with the corresponding thermal velocity of $v_{t\alpha}$, where $\alpha = e, i$.

5.2.2 Maxwellian random start

The first simulation is done by Vsim code with 1000 macro-particle per cell (1kPPC). Figure (5.3a) shows the evolution of the amplitude of the chosen modes $m = \{30, 37, 44, 51\}$ of the electric field, and Fig. (5.3b) shows the evolution of electrostatic energy with time. As we can see, after some initial oscillations, the amplitude of each mode shows noisy growth. The slope of this growth is not clear for measuring each mode's growth rate, and different intervals can lead to slightly different growth rates. I use the ploy fit technique with the lowest residual to measure the growth rate of each mode.

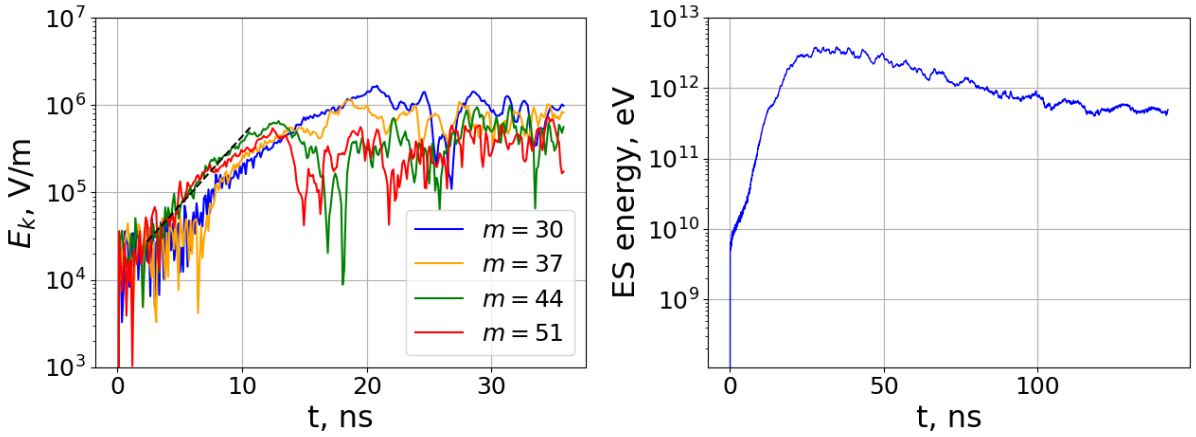

(a) **(b)**

Figure 5.3: (a) Evolution of individual modes of the electric field, (b) Evolution of the electrostatic energy, using 10^3 PPC, from VSim with random start. The dashed black line shows the fitted line on the $m = 44$ mode.

Table (5.3) shows the values of the linear growth rates calculated from simulations and the linear theory for comparison. These imprecise growth rates of the simulations with

Table 5.3: Comparison of the analytical growth rates with the growth rates observed in VSim-10^3 PPC, Xes1-10^4 PPC, and VSim-10^4 PPC simulations.

m	γ (Theory) $\times 10^8 s^{-1}$	γ (VSim-1kPPC) $\times 10^8 s^{-1}$	γ (Xes1-10kPPC) $\times 10^8 s^{-1}$	γ (VSim-10kPPC) $\times 10^8 s^{-1}$
30	0.90	2.39	3.37	2.67
37	1.08	2.67	2.22	1.79
44	1.17	3.63	3.15	3.55
51	1.07	3.16	2.46	2.5

1000 macro-particle per cell (PPC), which deviates significantly from the expectations of linear theory, indicate the interference of noise level in linear growth of simulation. In order to reduce the noise level, I increase the macro-particles per cell to 10^4 and redo the simulations with two PIC codes Xes1 and VSim.

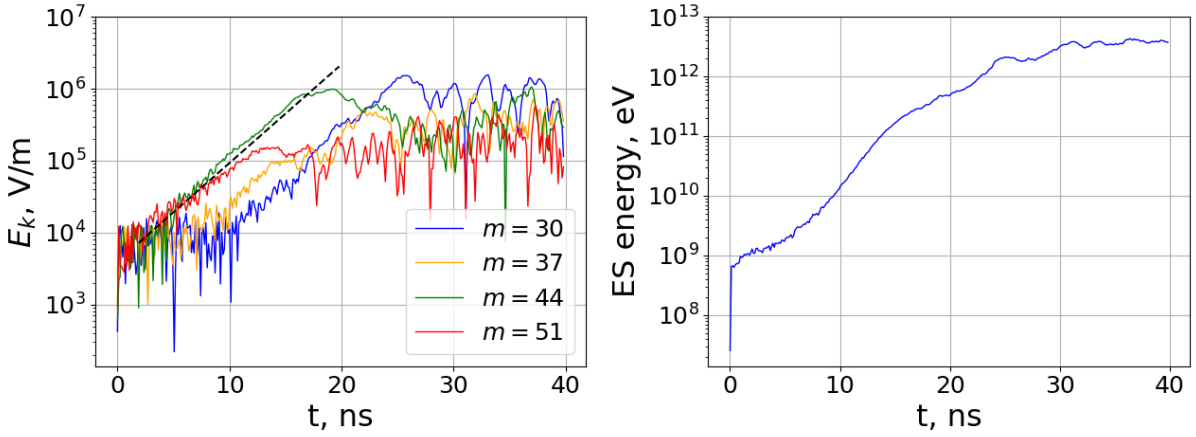

(a) **(b)**

Figure 5.4: (a) Evolution of individual modes of the electric field, (b) Evolution of the electrostatic energy, using 10^4 PPC, from Xes1 with random start. The dashed black line shows the fitted line on the $m = 44$ mode.

It is evident from Figs. (5.4, 5.5) that increasing macro-particles from 10^3 to 10^4 reduces the initial electrostatic energy by an approximate factor of 1/10, while the initial amplitude of individual modes is reduced by an approximate factor of $1/\sqrt{10}$. This proves that the initial noise is reduced approximately by a factor of $1/\sqrt{N_p}$, as expected. In comparison with the simulation with 10^3 particles per cell, the growth rates of Fig. (5.4) and Fig. (5.5) in Table (5.3) are closer to the analytical growth rates. Despite this improvement, the linear growth rates calculated in these simulations are still much larger than the analytical growth rates.

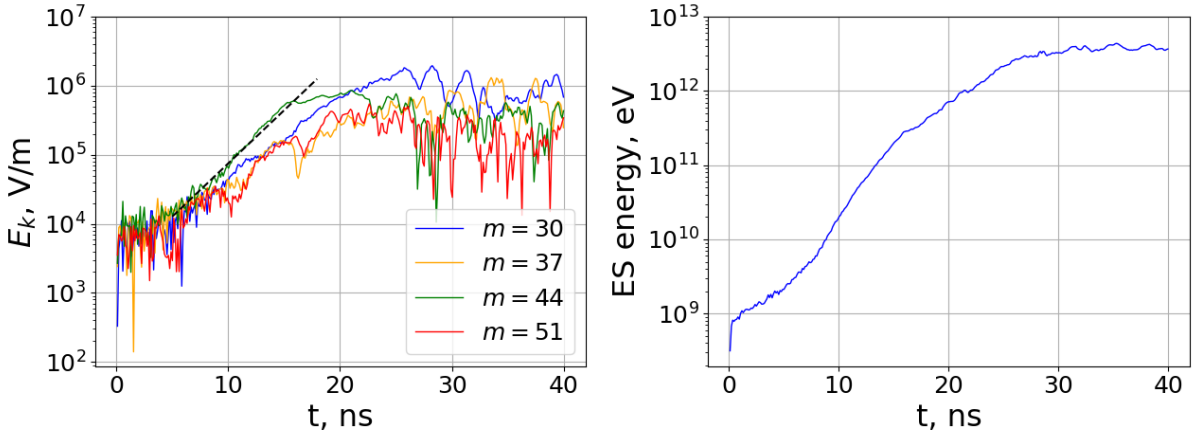

(a) (b)

Figure 5.5: (a) Evolution of individual modes of the electric field, (b) Evolution of the electrostatic energy, using 10^4 PPC, from VSim with random start. The dashed black line shows the fitted line on the $m = 44$ mode.

To reduce the adverse effects of the initial noise, a quiet start initialization has been proposed [33, 44], in contrast to the random start. Before redo simulations with quiet start initialization, in the next subsection I review the general idea of loading particles in particle in cell codes.

5.2.3 Particles loading in PIC simulation

One of the important issues in PIC simulation is distributing particles in the initial step in the phase space. The placement of particles in $\mathbf{x}-\mathbf{v}$ at $t = 0$ starts with desired space and velocity densities, $n_0(x)$ and $f_0(v)$ respectively. The systematic approach for generating the positions and velocities of each particle from density functions is called inversion of "cumulative density". Suppose we have $d(\xi)$ as the density function from $\xi = a$ to $\xi = b$, the cumulative distribution function is:

$$R_s(\xi) = \frac{\int_a^{\xi} d(\xi')d\xi'}{\int_a^{b} d(\xi')d\xi'}, \tag{5.8}$$

where ξ' can be either x or v. R_s is a uniform distribution of numbers $0 < R_s < 1$, that can be set as a numerical sequence, which generates quasi-random numbers with low discrepancy. Several sequences have been proposed in the literature, such as bit-reversed or Hammerssely sequence [45, 31, 46], Sobol sequence [47], and Fibonacci sequence [48]. This cumulative density calculates the probability of each component of v or x. By setting R_s, if the integral of distribution can be done explicitly, the inversion will produce the v or x corresponding to the distribution $d(\xi)$, otherwise the integral should be done numerically.

In plasma we have Maxwellian distribution function of particles in v space, $f_0(v) = \exp(-v^2/2v_t^2)$ which is in an equilibrium state. We are going to invert it to place particles in phase space. 1-Dimensional Maxwellian distribution function can not be integrated explicitly; therefore, the numerical method such as midpoint or trapezoidal rules is used with a uniform set of numbers for R_s, and then the corresponding velocity will find by interpolating; this method is called "quiet Maxwellian" velocity distribution [31].

Another direct way which is more common in particle in cell simulation is working with random numbers generator that produces a random normal Maxwellian distribution proved as a qualified distribution for velocity [45]. One problem does arise from the use of the random function. This randomness leads to the activation of unwanted Fourier modes and increases noises, making it impossible to distinguish the low-level physics from them.

Regarding particle's position, in most cases like our simulations, the density function of particles is uniform; therefore, we can use the uniform scheme mentioned before for R_s to load particle in x directly. For 1D distribution, the position of particles which limited in simulation box $0 < x_i < L$ can be defined as linear function of R_s like $x_i = LR_s$. The point is that the R_s set for velocity and position should be uncorrelated to avoid unwanted bunching in phase space.

We have selected a quiet start initialization in our 1d1v PIC simulations, which is proposed by J. A. Byers [44]. This scheme employs a smooth loading of particles in phase space to reduce the noise in PIC simulation. It uses the bit-reversed set for placing particles in position and the quiet Maxwellian scheme for particle velocity. I write a Matlab program based on the quiet start's method of Xes1 code proposed in Birdsall's book [31] to make the initial position and velocity of particles for loading into the simulation box of the VSim machine.

As a concise description of the bit-reversed scheme, the particle's position is calculated as follows:

$$x_i = LR_s + 0.5\frac{L}{N_p}, \tag{5.9}$$

where N_p is the number of macro-particles, L is the simulation box, and R_s is the result of radix-two digit reversal bit reversing plus zero [31]. Basically, there are N_p macro-particles numbered $i = 0$ to $N_p - 1$, which converted to a base-2 numbering system that contains only two digits, a "0" or a "1". We can also have binary weighting for values of less than 1 by producing unsigned fractional binary numbers. This happens by placing the binary digit to the right of the decimal point. Thus all fractional digits have respective weightings, which are negative powers of two, creating binary fraction as shown in the following Table (5.4),

Table 5.4: Base 2 bit-reversed fraction used for generating R_s.

particle's number	base-2	base-2 fraction	base-2 calculation of decimal	decimal (R_s)
0	0	0.0	0×2^{-1}	0
1	1	0.1	1×2^{-1}	1/2=0.5
2	10	0.01	$0 \times 2^{-1} + 1 \times 2^{-2}$	1/4=0.25
3	11	0.11	$1 \times 2^{-1} + 1 \times 2^{-2}$	1/2+1/4=3/4=0.75
4	100	0.001	$0 \times 2^{-1} + 0 \times 2^{-2} + 1 \times 2^{-3}$	1/8=0.125
5	101	0.101	$1 \times 2^{-1} + 0 \times 2^{-2} + 1 \times 2^{-3}$	1/2+1/8=5/8=0.625

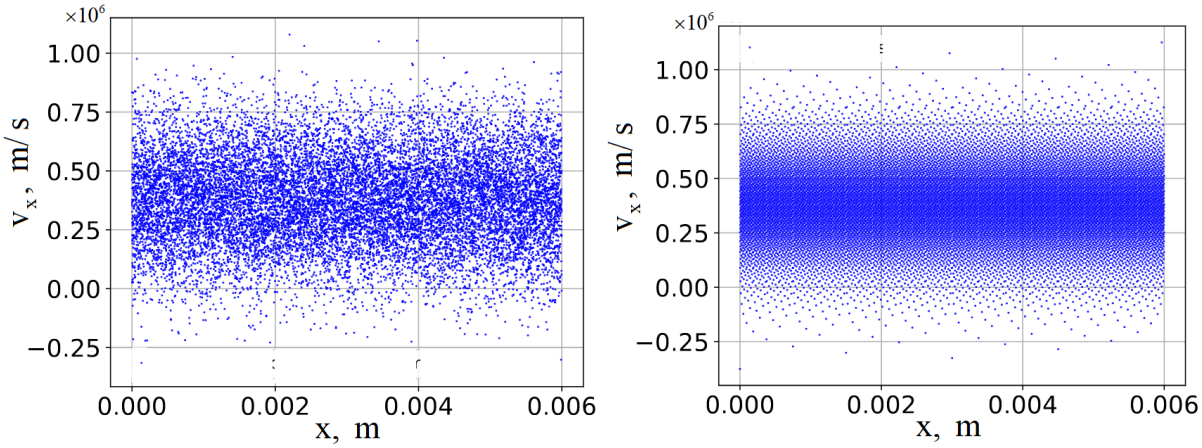

(a) **(b)**

Figure 5.6: Comparing the phase space of 16000 electrons with uniform loading (bit-reversed) in x and (a) random Maxwellian in v_x and (b) quiet Maxwellian in v.

5.2.4 Quiet start

Quiet start loading without perturbation

Instead of random loading particle's velocity, we use nonrandom initializations for v designed to achieve a quiet start besides bit reversed loading of particle's position. Loading particles using a quiet start algorithm leads to the more ordered phase space Fig. (5.6b).

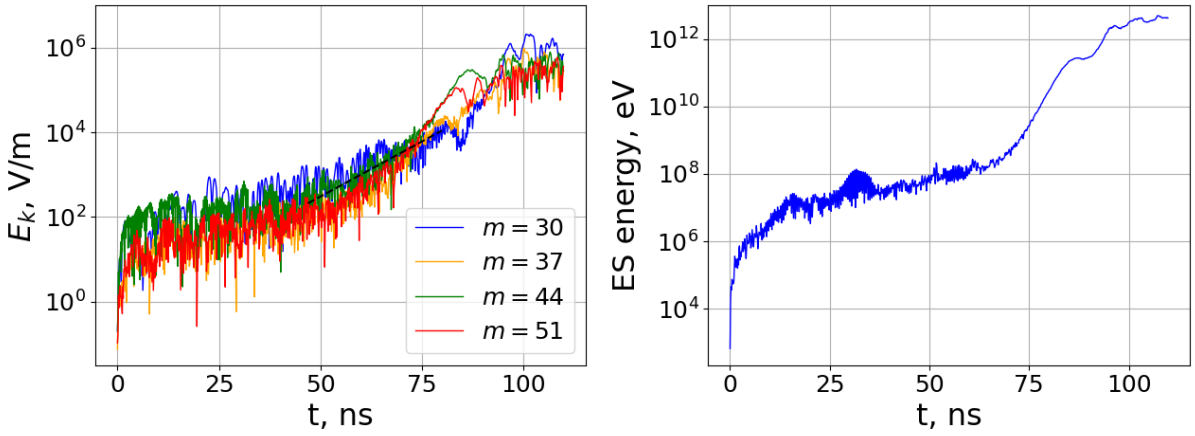

(a) **(b)**

Figure 5.7: (a) Evolution of individual modes of the electric field, b) Evolution of the electrostatic energy, using 10^4 PPC, from Xes1 with quiet start scheme without perturbation. The dashed black line shows the fitted line on the $m = 44$ mode.

Table 5.5: Comparison of the analytical growth rates with the growth rates observed in Xes1-quiet start without perturbation-10^4 PPC simulation.

m	γ (Theory) $\times 10^8 s^{-1}$	γ (Xes1) $\times 10^8 s^{-1}$
30	0.90	0.63
37	1.08	0.72
44	1.17	1.19
51	1.07	0.78

Fourier analysis of the electric field E_k reveals that the initial fluctuation level is much lower, and the growth rates of the individual modes experience one-third reduction from $\gamma = 3.15 \times 10^8$ s^{-1} in mode 44 for random start to the $\gamma = 1.19 \times 10^8$ s^{-1}. The most important effect of using quiet start is a substantial reduction by more than four orders of magnitude of the initial level of electrostatic energy from 10^9 eV to 10^5 eV. In addition, it seems that the linear growth starts with a delay from 40 ns and saturates at 80 ns, compares to the experiment without quiet start that starts at 5 ns and saturates at 20 ns.

The usage of quiet start distribution lets particles fill phase space smoothly. Hence, for a finite amount of time, particles act nearly like a continuous system that causes a delay in initiating plasma particle interactions.

It is clear that applying regular quiet start decreases the initial noise level and postpones the development of the thermal fluctuations; however, high amplitude fast oscillation in

modes undermine the accuracy of the simulation make the growth rate of individual mode is still out of the analytical results.

Since the ion and electron macro-particles are positioned in the same way, so the plasma is quasi-neutral. In common test, we have perturbed a particular mode with a finite amplitude in x, initially.

Quiet start loading with perturbation

The initial perturbation over the distribution starts interactions in plasma. Exciting a certain mode in the system requires introducing a disturbance in the particle's spatial or velocity distribution. In our simulations, we use a spatial perturbation for uniform x loading. A cold stationary plasma of charged particles is set up and then perturbed in any given mode [49].

Perturbation in space means that disturbing electrons from their equilibrium positions to oscillate about their equilibrium position with a defined amplitude which is equal to the initial displacement and frequency is given by:

$$f_{pe} = \frac{\omega_{pe}}{2\pi} = \frac{q_e}{2\pi}\sqrt{\frac{N_{pe}}{Lm_e\epsilon_0}}, \tag{5.10}$$

where ω_{pe} is the electron plasma frequency, L is the total length of the grid, m_e is the mass of the electron, and N_{pe} is the number of electron macro-particles. If we perturb all the electrons, a particle's position is given by:

$$x = x_0 + \epsilon \ \cos\left(\frac{2x_0\pi m}{L}\right), \tag{5.11}$$

where x is the electron position, x_0 is the electron's equilibrium position, ϵ is the amplitude of the displacement, m is the mode of excitation. According to the Ref. [49], ϵ should be very small compared with particle spacing, and in simulation with more particles than grid points, it is even smaller compared to the grid spacing Δx. Setting high ϵ leads to overlapping the particle displacements and makes it impossible to see sinusoidal waves [49].

Such a perturbation causes a sinusoidal charge density, and as a result of that, it stimulates a given mode in the spatial electric field, which oscillates with the plasma frequency [49].

For investigate the role of the initial perturbation in the quiet-start simulations, I have performed four PIC simulations with perturbing mode $m = 1$, mode $m = 31$, mode $m = 44$, and a group of modes $m = \{30, 37, 44, 51\}$. Figure (5.8) shows the configuration of the quiet phase space of 1000 electrons per cell while mode $m = 1$ is perturbed. The evolution of each modes of electric field for this setup can be seen in Fig. (5.9).

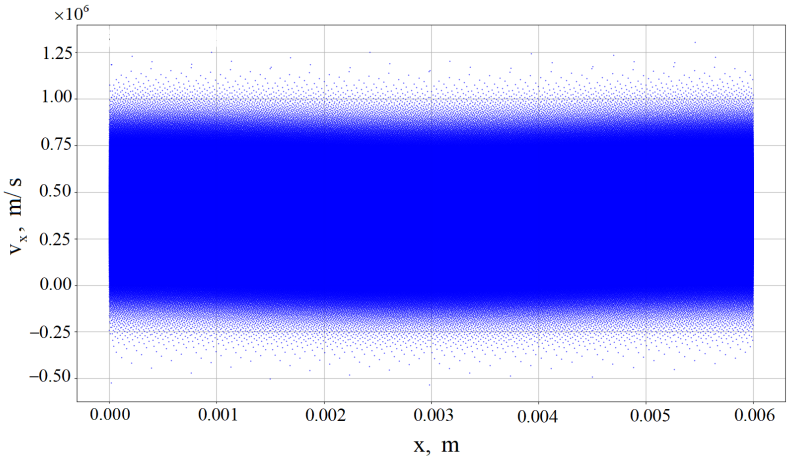

Figure 5.8: Phase space of 1000 electrons per cell with perturbing mode $m = 1$ in quiet start with amplitude $\epsilon = 0.02$ m. For better visualization, the number of particles shown here is reduced, and the amplitude of the perturbation is increased compared to those in actual simulations.

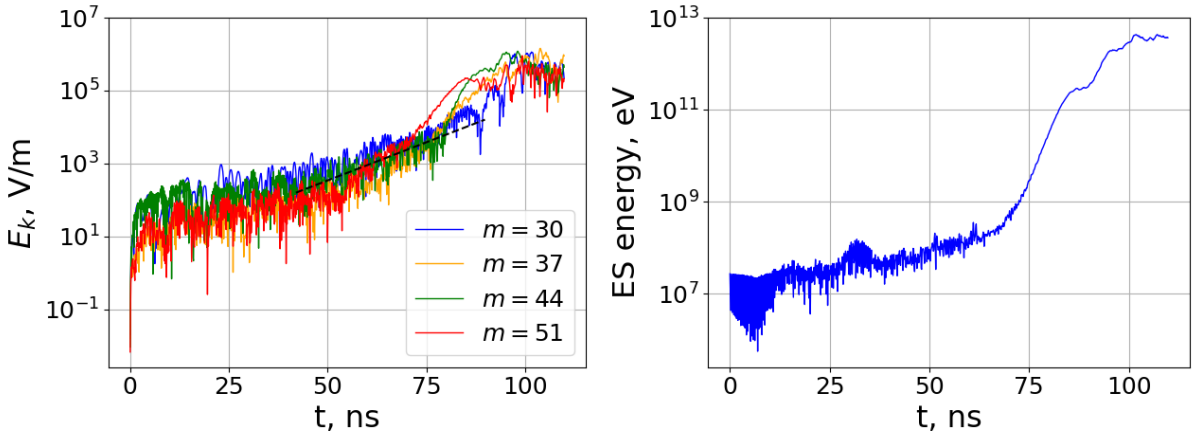

(a) **(b)**

Figure 5.9: (a) Evolution of individual modes of the electric field, (b) Evolution of the electrostatic energy, using 10^4 PPC, from Xes1 with quiet start and perturbing mode $m = 1$ with amplitude $\epsilon \approx 10^{-8}$ m. The dashed black line shows the fitted line on the $m = 44$ mode.

Table 5.6: Comparison of the analytical growth rates with the growth rates observed in Xes1-quiet start with perturbing mode $m = 1$ simulation.

m	γ (Theory) $\times 10^8 s^{-1}$	γ (Xes1) $\times 10^8 s^{-1}$
30	0.90	0.66
37	1.08	1.43
44	1.17	0.96
51	1.07	1.46

It can be seen from Fig. (5.9) perturbing mode $m = 1$ which belongs to the lowest frequency, with a small amplitude of $\epsilon \approx 10^{-8}$m, does not make any considerable improvement in the linear stage of the instability compare with the analytical result. The Fourier analysis of the electric field modes illustrates that the growth rate of modes near the unstable mode looks the same and indistinguishable, while they are supposed to be different. In this part, I show the simulation, which is initialized with $m = 31$ perturbations.

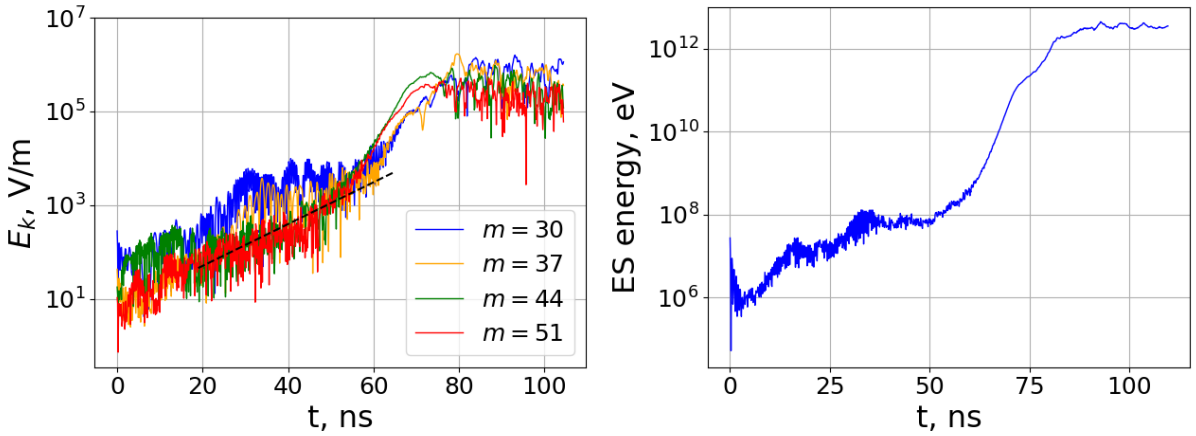

(a) **(b)**

Figure 5.10: (a) Evolution of individual modes of the electric field, (b) Evolution of the electrostatic energy, using 10^4 PPC, from Xes1 with quiet start and perturbing mode $m = 31$ with amplitude $\epsilon \approx 10^{-8}$ m. The dashed black line shows the fitted line on the $m = 44$ mode.

Table 5.7: Comparison of the analytical growth rates with the growth rates observed in Xes1-quiet start with perturbing mode $m = 31$ simulation.

m	γ (Theory) $\times 10^8 s^{-1}$	γ (Xes1) $\times 10^8 s^{-1}$
30	0.90	1.48
37	1.08	1.65
44	1.17	1.02
51	1.07	0.83

From Fig. (5.10) we can see perturbing mode $m = 31$ with a small amplitude of $\epsilon \approx 10^{-8}$ m which is near the unstable mode 44, makes an initial drop in electrostatic energy and electric field of mode 31. Exciting this mode decreases the time of transferring to the non-linear regime; therefore, saturation followed by the trapping oscillations happens at 70 ns. It can be seen that the growth of mode 37, which is affected by perturbing mode 31, dominates mode 44 between 20 ns to 50 ns and also becomes dominant in the saturation stage.

At this stage, I have perturbed the most unstable mode $m = 44$ and depicted the results of simulations with two different codes Xes1 and VSim. Figure (5.11) shows the configuration of quiet phase space while mode $m = 44$ is perturbed.

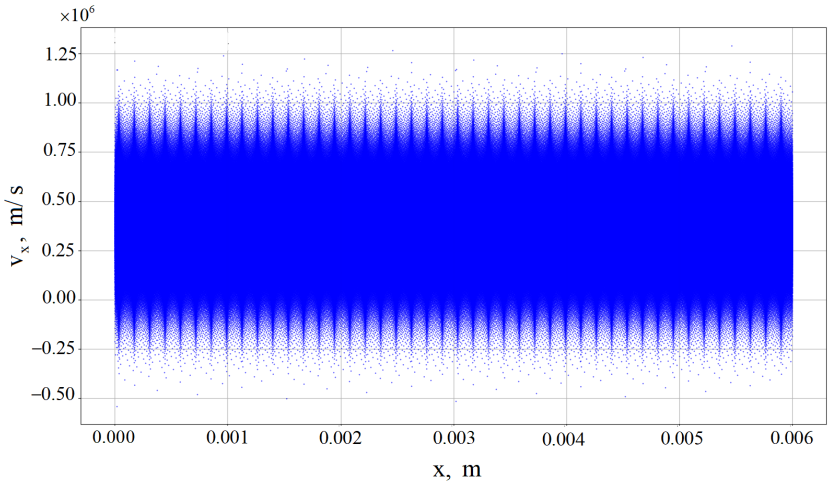

Figure 5.11: Phase space of 1000 electrons per cell with perturbing mode 44 in quiet start with amplitude $\epsilon = 0.02$ m. For better visualization, the number of particles shown here is reduced, and the amplitude of the perturbation is increased compared to those in actual simulations.

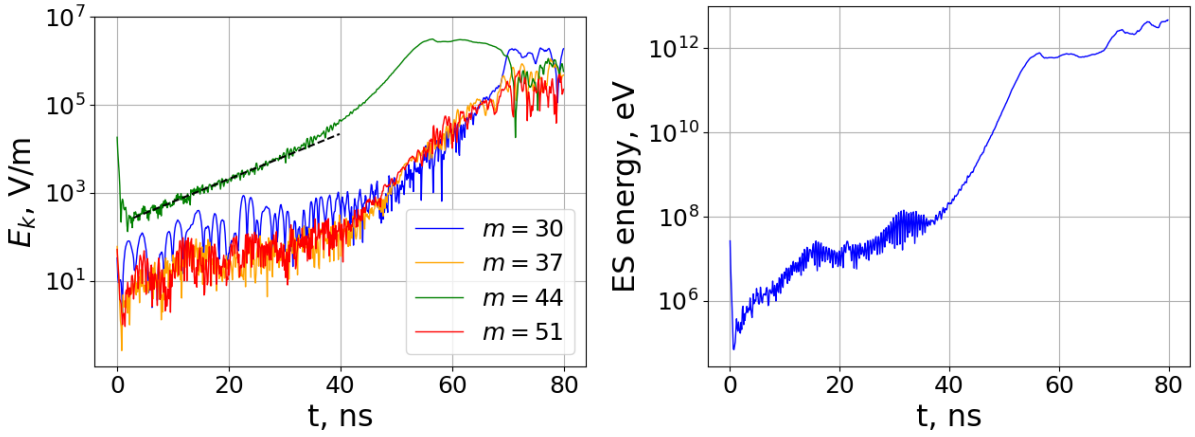

(a) **(b)**

Figure 5.12: (a) Evolution of individual modes of the electric field, (b) Evolution of the electrostatic energy, using 10^4 PPC, from Xes1 with quiet start and perturbing mode $m = 44$ with amplitude $\epsilon \approx 10^{-8}$ m. The dashed black line shows the fitted line on the $m = 44$ mode.

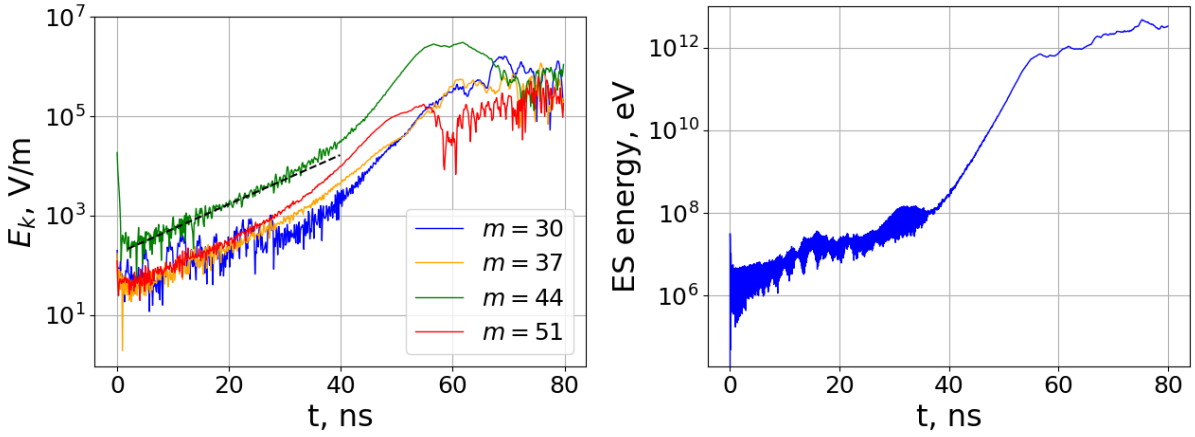

(a) **(b)**

Figure 5.13: (a) Evolution of individual modes of the electric field, (b) Evolution of the electrostatic energy, using 10^4 PPC, from VSim with quiet start and perturbing mode $m = 44$ with amplitude $\epsilon \approx 10^{-8}$ m. The dashed black line shows the fitted line on the $m = 44$ mode.

Table 5.8: Comparison of the analytical growth rates with the growth rates observed in Xes1 and VSim-quiet start with perturbing mode $m = 44$ simulation.

m	γ (Theory) $\times 10^8 s^{-1}$	γ (Xes1) $\times 10^8 s^{-1}$	γ (VSim) $\times 10^8 s^{-1}$
30	0.90	0.61	0.82
37	1.08	0.70	1.11
44	1.17	1.18	1.14
51	1.07	0.62	1.16

Figures (5.12, 5.13) show a surprising decrease in noise level of Fourier mode of electric field by perturbing unstable mode $m = 44$. Additionally, the numerical results show a qualitative agreement with the theory. The growth rate obtained from the numerical simulations, notably Xes1's results, has a 0.8% difference on unstable mode 44 with the analytical value. It can be concluded that exciting maximum-growth rate mode puts other modes in sequence and decreases the effect of the mode's interference. It seems that when two or more modes compete, the growth stage of the Fourier mode of wave electric field becomes non-uniform, noisy, and far from the analytical result in the linear regime. Comparing the electrostatic energy and Fourier analysis of E_k of Vsim and Xes1 results, reveals that except for a drastic plunge in the first 2 ns of simulation with Xes1, the initial energy and saturation level of both are consistent. In this part, I investigate the effect of perturbing a group of modes.

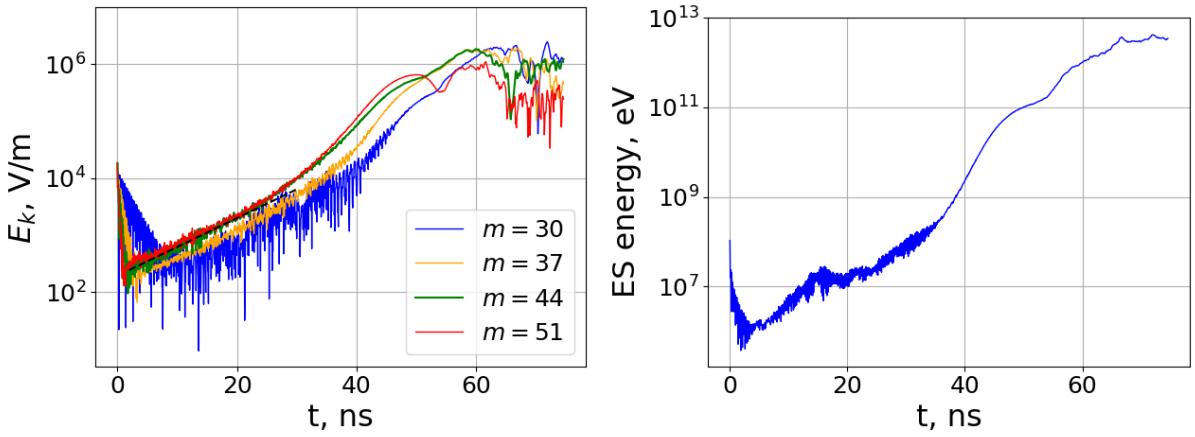

(a) **(b)**

Figure 5.14: (a) Evolution of individual modes of the electric field, (b) Evolution of the electrostatic energy, using 10^4 PPC, from Xes1 with quiet start and perturbing mode $m = 30, 37, 44, 51$ with amplitude $\epsilon \approx 10^{-8}$ m. The dashed black line shows the fitted line on the $m = 44$ mode.

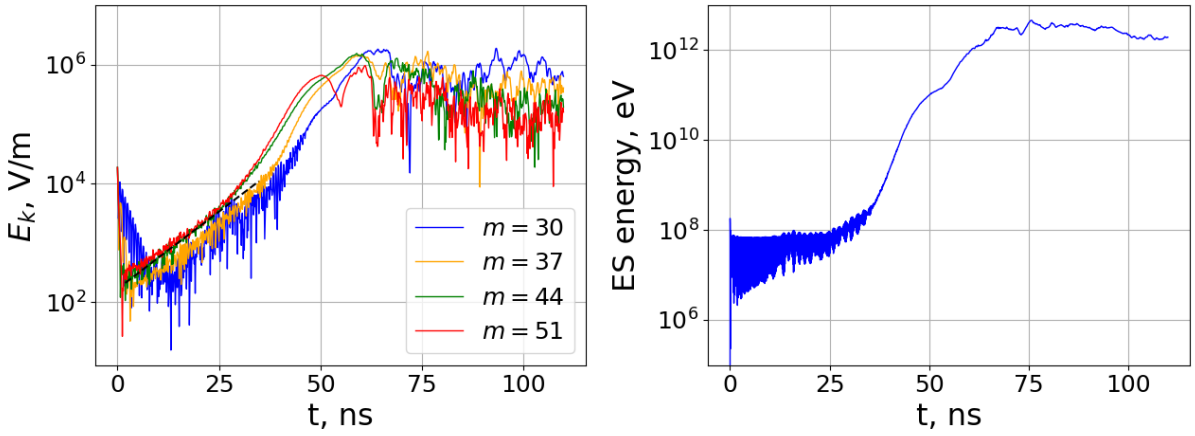

(a) **(b)**

Figure 5.15: (a) Evolution of individual modes of the electric field, b) Evolution of the electrostatic energy, using 10^4 PPC, from VSim with quiet start and perturbing mode $m = 30, 37, 44, 51$ with amplitude $\epsilon \approx 10^{-8}$ m. The dashed black line shows the fitted line on the $m = 44$ mode.

Table 5.9: Comparison of the analytical growth rates with the growth rates observed in Xes1 and VSim-quiet start with perturbing mode $m = 30, 37, 44, 51$ simulation.

m	γ (Theory) $\times 10^8 s^{-1}$	γ (Xes1) $\times 10^8 s^{-1}$	γ (VSim) $\times 10^8 s^{-1}$
30	0.90	0.98	1.66
37	1.08	1.16	1.13
44	1.17	1.16	1.19
51	1.07	1.16	1.11

Perturbing multimode by seven modes away from each other and near the unstable mode increases the amplitude of their Fourier mode of wave electric field. Furthermore, this initialization method indicates an improvement in the linearity of growth than the simulations with perturbing one mode; also, noisy behavior in perturbed mode decreases, and all selected modes experience a significant drop in their electric field in the first 2 ns. Although they do not stand in sequence in the growth stage, in saturation time, the unstable mode dominates others and makes other modes follow their sequence. Moreover, the measured growth rate of this case is much closer to the theory than its corresponding random-start simulation.

It is worth mentioning that quiet start loading without perturbation decreases initial electrostatic energy from 10^9 eV for random start to 10^5 eV, while perturbing the selected

mode despite a dramatic drop at the level of electrostatic energy increases electrostatic energy to 5×10^7 eV at the initial step, while perturbing the multimode rises electrostatic energy to the 10^8 eV.

From the physics point of view, the electrostatic energy figures show that the wave energy grows monotonically and eventually saturates, then it fluctuates at a certain level. The electron kinetic energy causes the initial growth in the wave energy. Basically, when the energy of the electrons is transferred to the waves, the velocity space distribution of the electrons becomes flattened. According to Ref. [2], in random start simulations, the main source of deviation of each mode's growth rate from analytical results is the sensitivity of growth rate to flattening the electron distribution function. In this work, although we confirm that using the quiet start scheme gives us a good result only if the most unstable mode is perturbed initially, this scheme does not completely solve the problem of initial noise in the low-frequency plasma physics problem.

5.3 Anomalous resistivity and backward waves in nonlinear regime of the Buneman instability

5.3.1 Anomalous resistivity

Buneman instability has been studied in various settings as a mechanism of turbulence and source of anomalous resistivity in space plasmas [50, 42, 51, 52, 53]. The linear regime of this instability is addressed in several studies [54, 55]. Since the nonlinear regime is complicated, the various nonlinear dynamics of that, like trapping, resultant holes [56, 57, 58, 59], nonlinear Landau damping [60], etc. still remain the several question of interest. In this regard, the numerical simulations assist in complementing the analytical theories.

In this section, I investigate and compare the evolution of average electron and ion current of the aforementioned PIC simulations of Buneman instability with $v_0 = 2v_{te}$ through passing the linear stage to the nonlinear phase with the similar case of Vlasov simulation that is performed by Arash Tavassoli in Ref. [2].

In collisionless plasmas, when the electron velocity relative to the ions exceeds a critical threshold whose upper value is v_{te}, plasma collective effects become significant and make it unstable. We witness in all the foregoing simulations, after a few nanoseconds, apart from the noisy behavior of PIC simulations, the field fluctuations grow exponentially at the expense of electron kinetic energy. The growing potential wells of waves trap electrons inside themselves and slow down the growth of instability and bring the linear stage to an end. At this time, the electric field reaches a peak that is followed by a slow decay due to the transfer of energy from waves to the plasma and particle heating. Trapping,

de-trapping, and scattering of electrons from large amplitude fluctuation of the potential result in the dramatic increase of electron temperature and decelerate electrons which are called anomalous resistivity while they lead to accelerating ions.

In the first stage, I present the result of the average electron and ion current of the Vlasov simulation, which linear stage of that is well in accordance with the prediction of linear theory. Then I show and compare the result of three PIC simulations that come from two PIC codes, Xes1 and VSim.

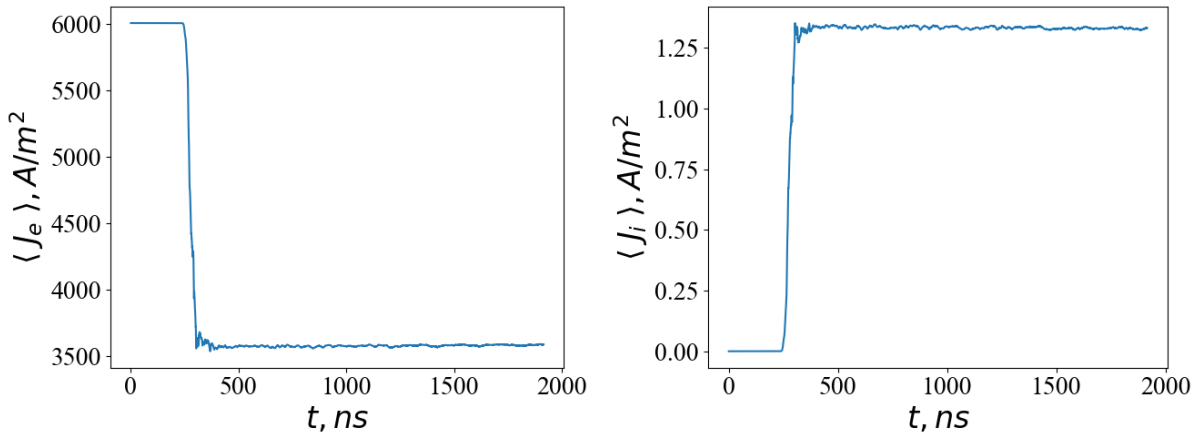

(a) (b)

Figure 5.16: Evolution of (a) electron and (b) ion current of Vlasov simulation performed by Arash Tavassoli.

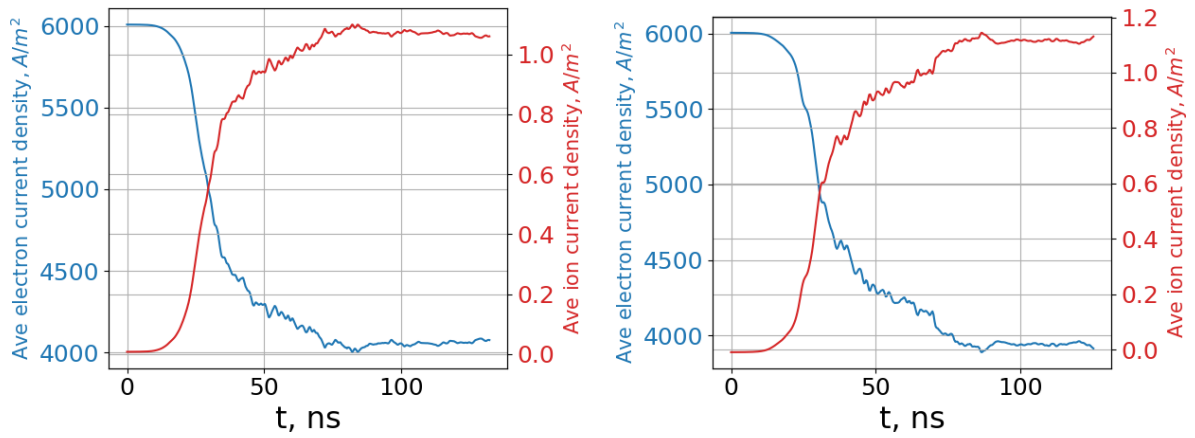

(a) (b)

Figure 5.17: Evolution of electron (solid blue line) and ion (solid red line) current of (a) VSim, (b) Xes1 with random start.

Looking at the electron current density of VSim and Xes1 with the random start in

Fig. (5.17) shows that in both, initial current starts at 6000 A/m^2, then it starts to drop in 15 ns, which is the time of ending linear stage of instability. Electron current of VSim reaches its saturation level at 4100 A/m^2 in 80 ns, while electron current of Xes1 levels off at 3900 A/m^2, in 85 ns. The saturation level of VSim and Xes1 code's results are almost 12% and 8.3% respectively, more than the corresponding Vlasov simulation result (3600 A/m^2).

The results of ion current density of Fig. (5.17) in both random start Xes1 and VSim illustrate that, initial current of both stand at 0 A/m^2 for the first 15 ns. The Ion current of VSim reaches its saturation level at 1.16 A/m^2 in 80 ns, while ion current of Xes1 levels off, in 85 ns it saturates at 1.1 A/m^2. The saturation level of the VSim code result and Xes1 are 14% and 18% respectively, less than the corresponding Vlasov simulation result (1.35 A/m^2).

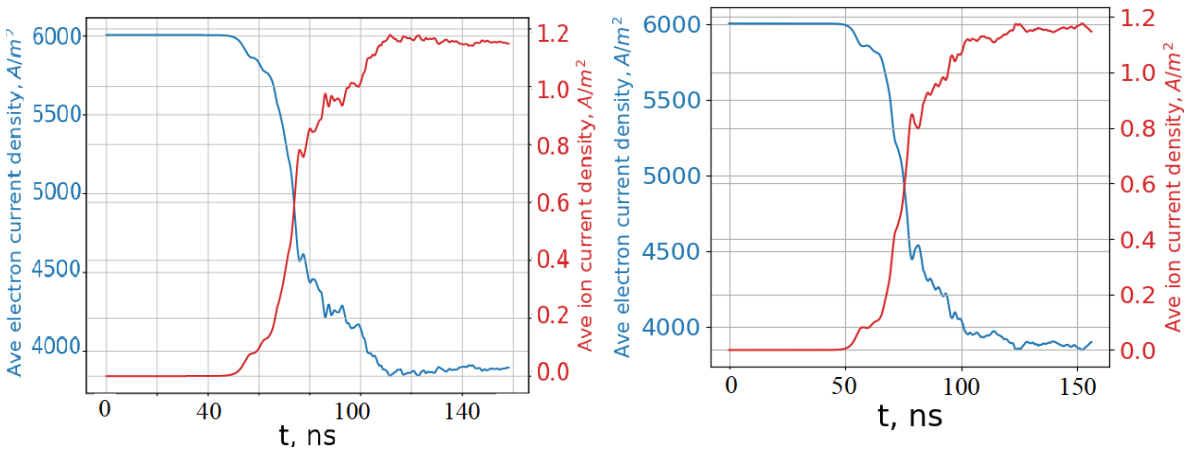

Figure 5.18: Evolution of electron (solid blue line) and ion (solid red line) current of (a) VSim, (b) Xes1 with quiet start loading and perturbing mode $m = 44$.

Comparing the result of current density from these two PIC simulations in Fig. (5.18) with Vlasov simulation in Fig. (5.16) shows that the initial electron current of VSim and Xes1 with quiet start perturbing mode 44, stands at 6000 A/m^2 and then starts to drop in 50 ns. Electron current of VSim reaches its saturation level at 3890 A/m^2 in 112 ns while for Xes1, it happens in 125 ns at the same level. In general, the saturation levels of electron current of these two PIC codes are 5% more than the corresponding Vlasov simulation result.

The result of ion current density of Fig. (5.18) indicates that the ion current of VSim and Xes1 have a good consistency. They both level off at 1.16 A/m^2 in 112 ns for VSim and 125 ns for Xes1. The point is that the saturation levels of ion current of the VSim and Xes1 are 14% less than the corresponding Vlasov simulation result.

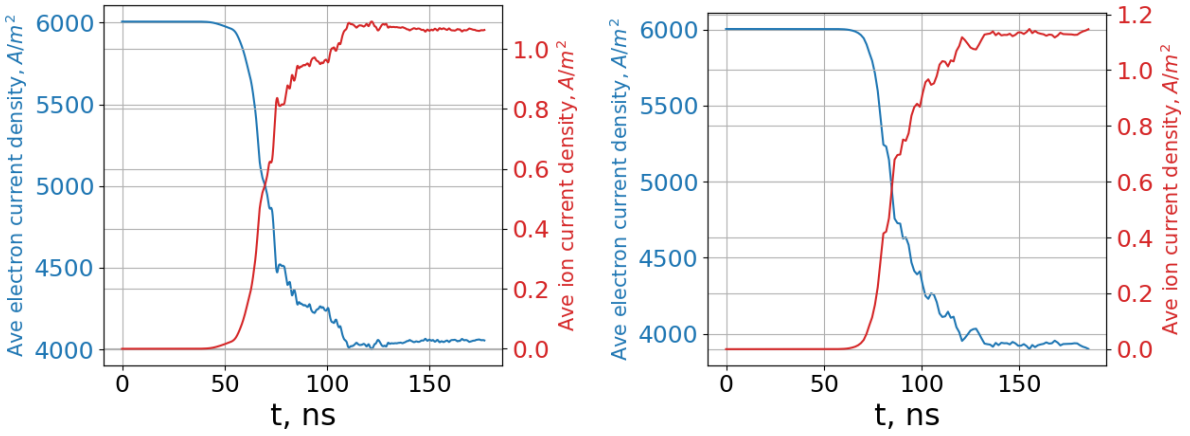

Figure 5.19: Evolution of electron (solid blue line) and ion (solid red line) current of (a) VSim, (b) Xes1 with quiet start loading and perturbing multi-modes: $m = 30, 37, 44, 51$.

From Fig. (5.19) of electron and ion current of VSim and Xes1 quiet start with perturbation in modes $m = 30, 37, 44, 51$, it can be concluded that The saturation level of electron current is 11% more than Vlasov simulation result, while the level of electron current of Xes1 saturates at 3900 A/m^2, almost 8% more than Vlasov simulation result and the level of ion current of VSim with 21%, Xes1 with 16% less than Vlasov simulation plateau.

The result of our comparison reveals that despite the fact the initial noise in PIC simulations deviates the linear growth rates from the prediction of linear theory, the anomalous resistivity of our PIC simulations as one of the nonlinear aspects of Buneman instability show a maximum 21% difference with Vlasov simulation result.

5.3.2 Backward waves

In the paper [1], that I have a contribution, we report the investigation of low- and high-frequency backward waves in the nonlinear regime of the unmagnetized Buneman instability. These backward waves are sub-waves that are propagating in the opposite direction of the first initial drift of electrons in the nonlinear stage of instability; therefore, they are not expected from linear theory. According to the Ref. [53] the excitation of the backward waves coincides with the enhancement of anomalous resistivity. In this paper, we find that the backward waves are excited if the value of the initial drift velocity exceeds a certain threshold, which was in our simulations somewhere between $v_0 = 1.5v_{te}$ to $v_0 = 1.75v_{te}$.

In this paper, we explain the mechanism of backward wave formation based on the linear theory for the stability of the electron velocity distribution function modified by

nonlinear effects. In this regard, we fit several Maxwellian functions over the velocity distribution function that we get from simulation, which has shown the extension of a wide plateau in the negative velocity region. As my contribution in this work I develop a Matlab solver and solve the related dispersion relation to get modes spectra and compare with simulation results. The resultant analytical mode frequency and corresponding growth rate show a close resemblance to eigen-mode spectra obtained from simulations.

5.4 Magnetized Buneman two-stream instability

Magnetized Buneman two-stream instability (MBTSI) happens due to relative drift of ions through electrons in the applied magnetic field $\mathbf{B} = B_0\hat{e}_z$ of cold plasmas. Technically, the beginning of ECDI mechanisms can be tracked down to this instability. In this regime the interaction is in the perpendicular plane to $\mathbf{B}$ and particles have position variable y and velocities v_x, v_y and possibly v_z [31]. The coordinates used are shown in Fig. (5.20). In general, Buneman instability is unmagnetized and strictly perpendicular to

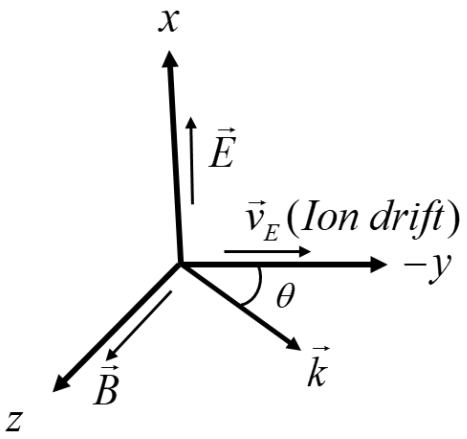

Figure 5.20: Theoretical model for drift-excited instabilities.

the magnetic field, and consider just the electron perpendicular motion in y-direction so $k_z = 0$. While, in the magnetized type of Buneman instability, both electron motions (parallel and perpendicular) are mentioned, [19].

5.4.1 Theoretical description of the MBTSI in linear regime

Taking cold electron limit $T_e \to 0$ of Eq. (2.1) results in remaining only two harmonics $m = 0$ and $m = 1$ of sum over all harmonics and other modes disappear automatically thus the general dispersion relation yields the following relation, that is called **magnetized Buneman two-stream instability**,

$$1 - \frac{\omega_{pi}^2}{\omega^2} - \frac{{k_z}^2\omega_{pe}^2}{k^2(\omega - k_y v_E)^2} - \frac{k_y^2\omega_{pe}^2}{k^2((\omega - k_y v_E)^2 - {\Omega^2}_{ce})} = 0. \tag{5.12}$$

This dispersion relation consists of both the modified two-stream instability (MTSI) and upper hybrid two-stream instability. In the modified two-stream instability as we see in chapter 2, the effect of the electron parallel and perpendicular motion is typically considered.

5.5 1D-PIC simulation of MBTSI

5.5.1 Simulation model

In this work, both ions and electrons are treated as cold, so ion's temperature equals zero ($T_{0i} = 0$) and $v_{ti} = 0$ and electron's temperature is low at $T_{0e} = 0.0002$ eV. One of the main threshold values that must be considered for investigating the Buneman instability is that the relative drift velocity between ions and electrons must be larger than the electron and ion thermal velocity. ($v_E > v_{te}, v_E > v_{ti}$).

It is common to use the electron frame (electrons not drifting) for investigating this instability. In the electron frame, the ions have a steady drift v_E in $-y$ direction. In this frame, the cold dispersion relation, as investigated by Buneman (1962), is

$$1 - \frac{k_y^2\omega_{pe}^2}{k^2(\omega^2 - \Omega_{ce}^2)} - \frac{k_z^2\omega_{pe}^2}{k^2\omega^2} - \frac{\omega_{pi}^2}{(\omega - k_y v_E)^2} = 0. \tag{5.13}$$

By considering $\tan\theta = k_z/k_y$ in Fig. (5.20), we can see two regimes of instabilities. One is upper hybrid two stream instability where ($\theta = 0$ and $k_z = 0$) and the other one is modified two stream instability, which is when $\theta \neq 0$ and the wave vector $\mathbf{k}$ has a non-zero component along magnetic field $\mathbf{B}$.

By assuming $k_z = 0$ of MBTSI, it can be possible to investigate some of the features of this instability with 1D simulation and compare the result with the result of the numerical solution of dispersion relation for $k_z = 0$. In this regard, I perform two test case 1D-PIC simulations with Xes1 code. For the first experiment I consider ion-to-electron mass ratio $m_i = 100m_e$, and for the second experiment I consider hydrogen plasma.

Fig. (5.21) presents the numerical solution of magnetized Buneman dispersion relation (5.12) with the general parameters of simulation are described in Table (5.10). The growth rate and frequency are presented as a function of k_y for hydrogen plasma and plasma with ion mass $m_i = 100m_e$. One can see from Fig. (5.21) is that by reducing the value of k_z, we reach the limit corresponding to the limit $k_z = 0$ in the Eq. (5.12).

One can notice from Fig. (5.21) is that in this limit just two harmonics for each chosen k_z remain and others disappear. Furthermore, as it can be seen from the graph, for mass ratio $m_i = 100m_e$ the maximum growth rate for the $k_z\lambda_D = 0.00001$, occurs at almost $k_y/k_0 = 15$ with $\gamma = 1.16\omega_{pi} = 2.06 \times 10^9(1/\text{s})$ and for mass ratio $m_i = 1836m_e$, the maximum growth rate happens in $k_y/k_0 = 60$ with $\gamma = 2\omega_{pi} = 0.83 \times 10^9(1/\text{s})$.

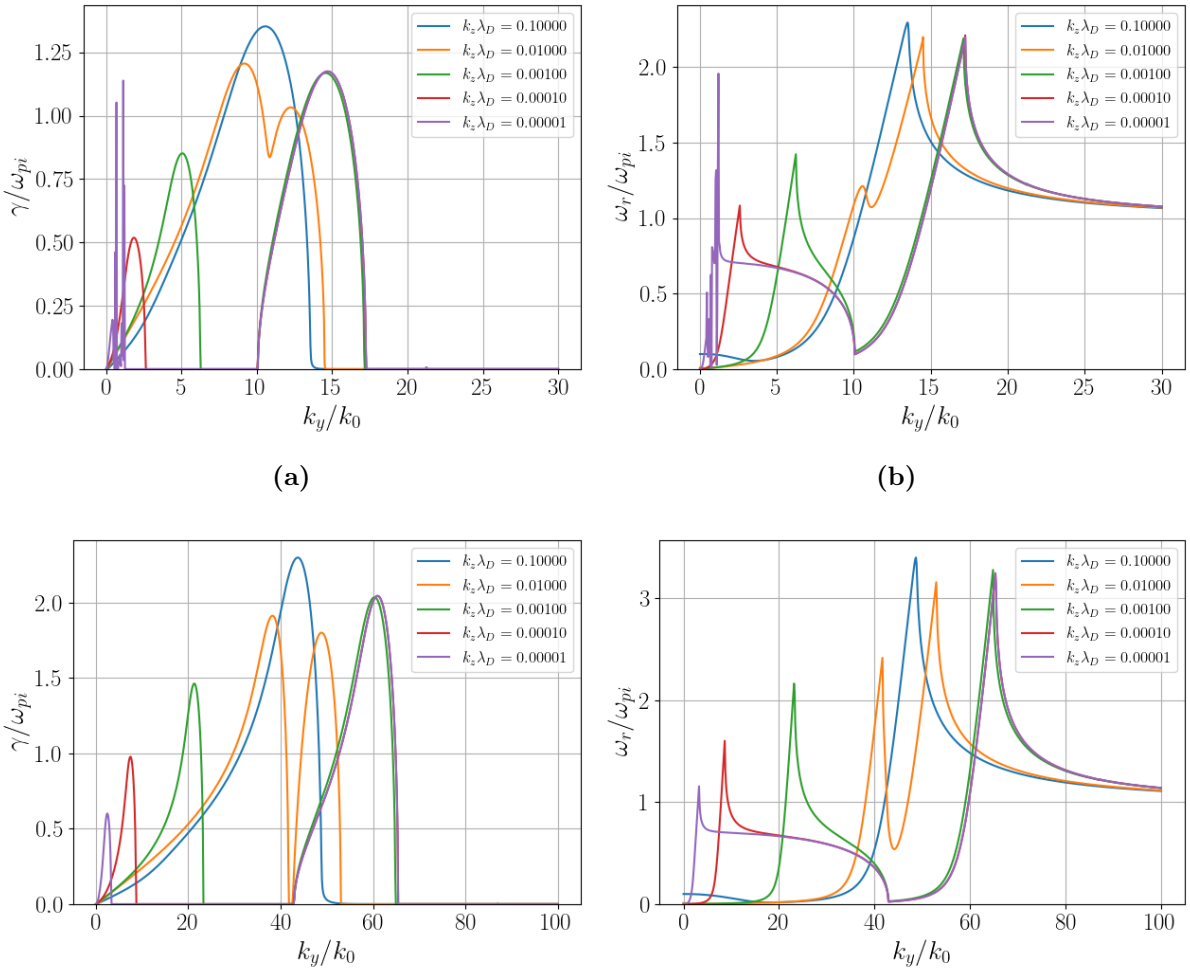

Figure 5.21: (a) growth rate and (b) frequency of the instability for mass case $m_i = 100m_e$. (c) growth rate and (d) frequency of the instability for mass case $m_i = 1836m_e$, here $k_0 = \omega_{pi}/v_E$.

5.5.2 Simulation results

The initial parameters used for investigating Buneman type two-stream instability by Xes1 code are in the following. The simulation time step resolves accuracy and stability by providing the practical criteria of $\omega_p \Delta t < 0.5$ and Δt satisfies the CFL condition on the Δx grid which is $\Delta t < \Delta x/v_{te}$. These simulations are done by using Beamcycl.inp project file.

Table 5.10: Plasma parameters used for simulations.

General parameters
$E_0 = 2.598848 \times 10^5 \mathrm{V}/m$
$B_0 = 0.1015625$ T
$L = 0.006$ m
$n_0 = 10^{17} \mathrm{m}^{-3}$
$T_{0e} = 0.0002$ eV
$T_{0i} = 0.0$ eV
$v_E = 2.56 \times 10^6 \mathrm{m}/s$
$\omega_{pe} = 1.78 \times 10^{10} 1/\mathrm{s}$
$\lambda_D = 3.33 \times 10^{-7} \mathrm{m}$

Simulation parameters

Time step (Δt) = 11.23 ps

Number of grid points = 64

Cell size (Δx) = 0.93×10^{-4}m

Number particles for each species = 20000

Number of particles per cell = 312

Test case 1

Simulation is performed in the electron frame with ion drift velocity $v_E = 2.56 \times 10^6$m/s, mass ratio $m_i = 100 m_e$, and electron thermal velocity $v_{te} = 5.93 \times 10^3$ m/s.

The evolution of phase space in Fig. (5.22) represents, when the wave energy becomes large, plasma goes into the nonlinear regime, and particles execute vortex-like motion in the phase space (i.e., they are trapped by the waves).

The time evolution of the amplitude of electrostatic field energy is shown in Fig. (5.23). One can see the linear growth and nonlinear saturation of the Buneman type two-stream instability. The dashed red line represents a polynomial with a degree of 1, $y = 2\gamma t + c$ that fits the given data to evaluate the growth rate. The value of growth rate is $\gamma = 1.8793 \times 10^9 (1/\mathrm{s})$ which is comparable with the numerical result $\gamma = 1.16\omega_{pi} = 2.06 \times 10^9 (1/\mathrm{s})$.

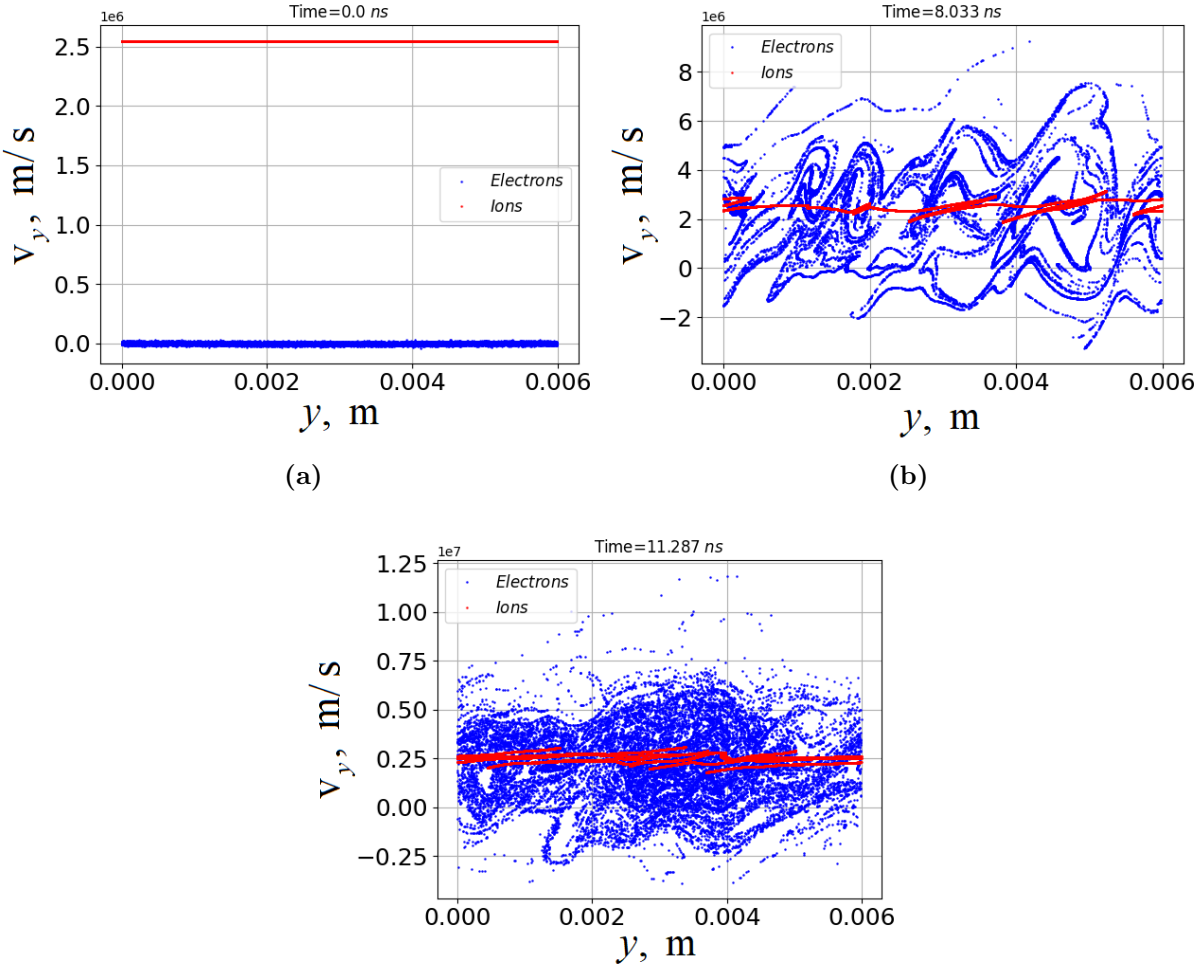

Figure 5.22: Evolution of the electrons and ions phase space $(v_y - y)$ in the case of $m_i = 100m_e$. (a), (b) and, (c) show the phase space at three different time windows $t = 0$ ns, $t = 8.0335$ ns and, $t = 11.287$ ns respectively. Bold blue dots represent the electrons and bold red dots indicate the ions.

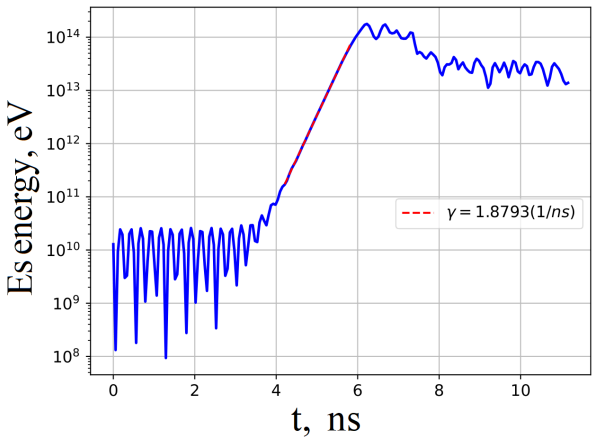

Figure 5.23: Evolution of the electrostatic energy versus time.

Test case 2

In the test case 2, simulation is performed in the electron frame with ion drift velocity $v_E = 2.56 \times 10^6$ m/s, mass ratio $m_i = 1836 m_e$, and electron thermal velocity $v_{te} = 5.93 \times 10^3$ m/s.

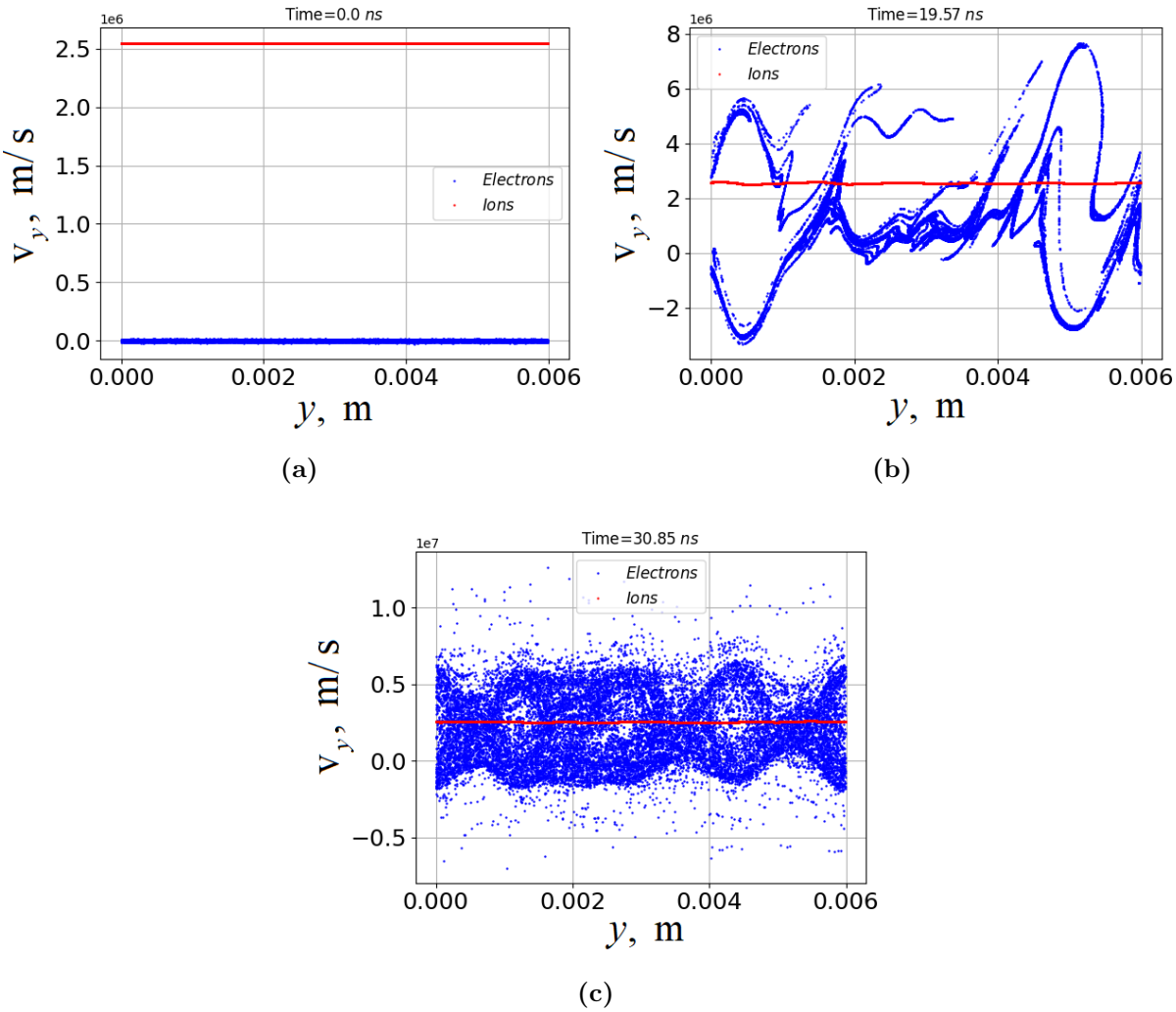

Figure 5.24: Evolution of the electrons and ions phase space ($v_y - y$) in the case of $m_i = 1836 m_e$. (a), (b) and, (c) show the phase space at three different time windows $t = 0$ ns, $t = 19.57$ ns and, $t = 30.85$ ns respectively. Bold blue dots represent the electrons and bold red dots indicate the ions.

The value of growth rate is in Fig. (5.25) $\gamma = 0.6201 \times 10^9 (1/\text{s})$, compare to the result of numerical solution that is $\gamma = 2\omega_{pi} = 0.83 \times 10^9 (1/\text{s})$.

Comparing the electrostatic evolution of these two test cases reveals that, despite a clear difference in growth time which is almost 6 ns for hydrogen plasma and 2 ns for the case with mass ratio, $m_i = 100 m_e$, the initial and saturation energy are the same.

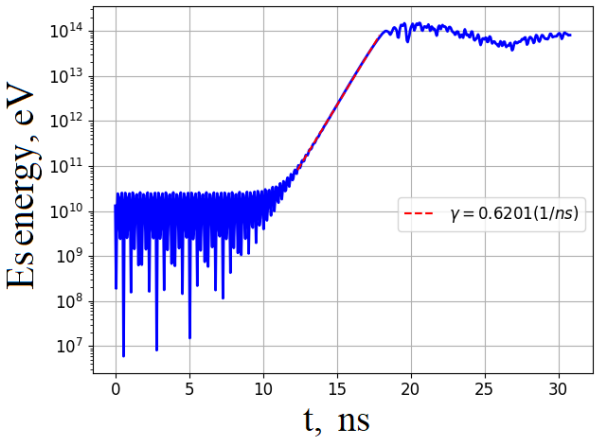

Figure 5.25: Evolution of the electrostatic energy versus time.

5.6 Summary

In the first part of this chapter, the effect of noise in PIC simulations on the occurrence of the Buneman instability in unmagnetized plasmas is reported. The performed simulations show that investigation of the dynamics of kinetic of Buneman instability for low relative drift velocity of the electrons with respect to ions $v_E = 2v_{te}$ which consist of low-level physics using the conventional PIC simulation models, is difficult and the linear stage of the instability in PIC simulations differs significantly from the analytical predictions. One possible solution for reducing this statistical noise is increasing the number of macro-particles N_p, which is impossible due to expensive computational costs. Another treatment is applying a standard quiet start scheme. In this regard, 1D-PIC simulations with two codes are performed. Our results confirm that the initial noise interferes with linear growth and undermines simulation accuracy in the linear regime and nonlinear stage. Furthermore, the quiet start scheme cannot solve the problem entirely unless accompanied by perturbing the most unstable mode.

In the second part, We address two aspects of the nonlinear stage of unmagnetized Buneman instability. We compare the anomalous resistivity of PIC simulations with the similar case of Vlasov simulation, which shows the maximum 21% discrepancy. Then We explain the existence of backward-propagating waves based on modifying electron velocity distribution function by nonlinear effects. The modes spectra from solving related dispersion relation show good consistency with simulation ones.

In the third part, We report the 1D-PIC simulation of magnetized Buneman two-stream instability. The performed simulation for mass case $m_i = 100m_e$ of plasma indicates 91% consistency between the growth rate of simulation and analytical results, while for the hydrogen mass plasma, this consistency drops to 75%.

Chapter 6

Summary

This dissertation investigates the gradient density drift and two-stream instabilities with analytical models and PIC simulations. In this respect, in chapter 2, the linear instability criterion of three alternative regimes: ion-acoustic, modified two-stream, and electron cyclotron drift modes for $T_e >> T_i$ without taking into account the effect of the density gradient are confirmed. We evaluate the impact of finite values of wavevector along the magnetic field, and We observe the broadening of ECDI resonances and transition toward the ion-acoustic regime. For solving dispersion relations, We employ the technique provided in Ref.[12]. Studying the effect of density gradient on ECDI reveals that for purely azimuthal wave vectors, the negative gradients density increase the growth rates of ECDI resonances. In contrast, the positive gradients density reduce the growth rates. This study also reveals that the azimuthal long-wavelength mode is most strongly affected by the density gradient corresponding to the lower-hybrid mode. Despite having a weaker growth rate in this branch compared to higher modes, they are predicted to be more critical for transport [19] due to difficulty in stabilizing them.

In chapter 3, the lower-hybrid modes as a subset of more general ECDI are studied. In order to do so, we perform an eigenfrequencies analysis of the kinetic model of LHDI and fluid models in linear stage. The comparison for different limits with generic Hall thruster parameters indicates that the kinetic model and an advanced fluid model [20] are quite consistent. This advanced fluid model is governed by the equilibrium electron current, electron inertia, electron temperature, plasma density gradient, and the Debye length. Meanwhile, a distinct new regime of lower-hybrid modes for cold electron approximation ($T_e \to 0$) is observed that occurs not only for the strong fields but also for the low fields subject to the $v_E/|L_n|\Omega_{ci} \approx 0.1$. These results suggest that fluid model, which is much less demanding computationally, provides a viable alternative to fully kinetic models.

In chapter 5, we perform a set of PIC simulations investigating the linear and nonlinear features of magnetized and unmagnetized Buneman instability as a limit of ECDI.

We present 1D-PIC simulations for the magnetized case of Buneman instability for cold electron limit. The results of simulations in the linear stage indicate 91% consistency between the growth rate of simulation and analytical findings for the mass case $m_i = 100m_e$ of plasma; for the hydrogen mass plasma, this consistency is 75%. Regarding unmagnetized Buneman instability, we discover that in the regime of low drift velocity $v_0 = 2v_{te}$, the growth rate of the linear stage of instability from 1D simulation of two PIC codes differs considerably from the analytical expectations. Therefore, we perform a series of high-resolved PIC simulations with two PIC codes to reduce the noise issues caused by particle discreteness. In this respect, besides increasing the number of macro-particles, we apply the method of quiet start for loading macro-particles uniformly in the phase space. From the results of both simulation codes, we conclude that although applying the quiet start scheme with perturbing the most unstable mode improves the accuracy of the linear stage, the noise issue of PIC simulation in this regime is not resolved entirely.

Bibliography

[1] A. Tavassoli, M. Shoucri, A. Smolyakov, M. Papahn Zadeh, and R. J. Spiteri, "Backward waves in the nonlinear regime of the Buneman instability," *Physics of Plasmas*, vol. 28, no. 2, p. 022307, 2021.

[2] A. Tavassoli, S. Janhunen, O. Chapurin, M. Jimenez Jimenez, T. Zintel, M. Papahn Zadeh, M. Shoucri, R. Spiteri, L. Couedel, and A. Smolyakov, "Nonlinear and noise effects in development of Buneman instability," in *APS Division of Plasma Physics Meeting Abstracts*, vol. 2020, pp. VO04–007, 2020.

[3] A. Piel, *Plasma physics: an introduction to laboratory, space, and fusion plasmas*. Springer, 2017.

[4] F. F. Chen, *Introduction to plasma physics*. Springer Science & Business Media, 2012.

[5] D. R. Nicholson, *Introduction to plasma theory*. Wiley New York, 1983.

[6] N. A. Krall and A. W. Trivelpiece, *Principles of plasma physics*, vol. 41. American Association of Physics Teachers, 1973.

[7] J. A. Bittencourt, *Fundamentals of plasma physics*. New York: Springer, 3rd ed. ed., 2004.

[8] S. P. Gary, *Theory of space plasma microinstabilities*. Cambridge university press, 1993.

[9] A. Vlasov, "On the kinetic theory of an assembly of particles with collective interaction," *Russian Physics Journal*, vol. 9, pp. 25–40, 1945.

[10] J. D. Huba, *NRL plasma formulary*, vol. 6790. Naval Research Laboratory, 1998.

[11] A. Fridman, "The critical magnetic field and anomalous diffusion in a weakly ionized plasma," *Doklady Akademii Nauk SSSR (U.S.S.R.) English translation currently published in a number of subject-oriented journals*, vol. 154, 1964.

[12] J. Cavalier, N. Lemoine, G. Bonhomme, S. Tsikata, C. Honore, and D. Gresillon, "Hall thruster plasma fluctuations identified as the $\mathbf{E} \times \mathbf{B}$ electron drift instability: Modeling and fitting on experimental data," *Physics of Plasmas*, vol. 20, no. 8, p. 082107, 2013.

[13] C. Lashmore-Davies and T. Martin, "Electrostatic instabilities driven by an electric current perpendicular to a magnetic field," *Nuclear Fusion*, vol. 13, no. 2, p. 193, 1973.

[14] S. P. Gary and J. Sanderson, "Longitudinal waves in a perpendicular collisionless plasma shock: I.Cold ions," *Journal of Plasma Physics*, vol. 4, no. 4, pp. 739–751, 1970.

[15] E. Priest and J. Sanderson, "Ion acoustic instability in collisionless shocks," *Plasma Physics*, vol. 14, no. 10, p. 951, 1972.

[16] J. Boeuf and L. Garrigues, "Low frequency oscillations in a stationary plasma thruster," *Journal of Applied Physics*, vol. 84, no. 7, pp. 3541–3554, 1998.

[17] R. Hofer, I. Mikellides, I. Katz, and D. Goebel, "Wall sheath and electron mobility modeling in hybrid-PIC Hall thruster simulations," in *43rd AIAA/ASME/SAE/ASEE Joint Propulsion Conference & Exhibit*, pp. 52–67, 2007.

[18] I. Kronhaus, A. Kapulkin, V. Balabanov, M. Rubanovich, M. Guelman, and B. Natan, "Investigation of physical processes in CAMILA Hall thruster using electrical probes," *Journal of Physics D: Applied Physics*, vol. 45, no. 17, p. 175203, 2012.

[19] S. Janhunen, A. Smolyakov, D. Sydorenko, M. Jimenez, I. Kaganovich, and Y. Raitses, "Evolution of the electron cyclotron drift instability in two-dimensions," *Physics of Plasmas*, vol. 25, no. 8, p. 082308, 2018.

[20] A. Smolyakov, O. Chapurin, W. Frias, O. Koshkarov, I. Romadanov, T. Tang, M. Umansky, Y. Raitses, I. Kaganovich, and V. Lakhin, "Fluid theory and simulations of instabilities, turbulent transport and coherent structures in partially-magnetized plasmas of discharges," *Plasma Physics and Controlled Fusion*, vol. 59, no. 1, p. 014041, 2016.

[21] O. Koshkarov, A. Smolyakov, Y. Raitses, and I. Kaganovich, "Self-organization, structures, and anomalous transport in turbulent partially magnetized plasmas with crossed electric and magnetic fields," *Physical Review Letters*, vol. 122, no. 18, p. 185001, 2019.

[22] N. A. Krall and P. C. Liewer, "Low-frequency instabilities in magnetic pulses," *Physical Review A*, vol. 4, no. 5, p. 2094, 1971.

[23] A. Fruchtman, "The lower-hybrid drift instability in a slab geometry," *Physics of Fluids B: Plasma Physics*, vol. 1, no. 2, pp. 422–429, 1989.

[24] A. Simon, "Instability of a partially ionized plasma in crossed electric and magnetic fields," *The Physics of Fluids*, vol. 6, no. 3, pp. 382–388, 1963.

[25] I. Romadanov, A. Smolyakov, E. Raitses, I. Kaganovich, and S. Ryzhkov, "Structure of unstable nonlocal gradientdrift modes in Hall $\mathbf{E} \times \mathbf{B}$ discharges, submitted to," *Physics of Plasmas*, vol. 23, no. 12, p. 122111, 2016.

[26] Y. Sakawa, C. Joshi, P. Kaw, F. Chen, and V. Jain, "Excitation of the modified Simon-Hoh instability in an electron beam produced plasma," *Physics of Fluids B: Plasma Physics*, vol. 5, no. 6, pp. 1681–1694, 1993.

[27] S. Bal and M. Bose, "Modified Simon-Hoh instability in a magnetized inhomogeneous dusty plasma," *Journal of Physics: Conference Series*, vol. 208, no. 1, p. 012081, 2010.

[28] N. Marusov, E. Sorokina, V. Lakhin, V. Ilgisonis, and A. Smolyakov, "Gradient-drift instability applied to Hall thrusters," *Plasma Sources Science and Technology*, vol. 28, no. 1, p. 015002, 2019.

[29] A. Hirose and I. Alexeff, "Electrostatic instabilities driven by currents perpendicular to an external magnetic field," *Nuclear Fusion*, vol. 12, no. 3, p. 315, 1972.

[30] V. Lakhin, V. Ilgisonis, A. Smolyakov, E. Sorokina, and N. Marusov, "Effects of finite electron temperature on gradient drift instabilities in partially magnetized plasmas," *Physics of Plasmas*, vol. 25, no. 1, p. 012106, 2018.

[31] C. K. Birdsall and A. B. Langdon, *Plasma physics via computer simulation*. CRC press, 2004.

[32] R. Hockney and J. Eastwood, *Computer Simulation Using Particles*. CRC Press, 1988.

[33] J. M. Dawson, "Particle simulation of plasmas," *Reviews of Modern Physics*, vol. 55, no. 2, p. 403, 1983.

[34] D. W. Forslund, "Fundamentals of plasma simulation," *Space Science Reviews*, vol. 42, no. 1-2, pp. 3–16, 1985.

[35] D. Potter, *Computational Physics*. A Wiley-Interscience publication, J. Wiley, 1973.

[36] J. P. Verboncoeur, "Particle simulation of plasmas: review and advances," *Plasma Physics and Controlled Fusion*, vol. 47, no. 5A, p. A231, 2005.

[37] C. B. Laney, *Computational gas dynamics*. Cambridge university press, 1998.

[38] D. Sydorenko, *Particle-in-cell simulations of electron dynamics in low pressure discharges with magnetic fields*. PhD thesis, University of Saskatchewan, 2006.

[39] P. Yoon and T. Umeda, "Nonlinear turbulence theory and simulation of Buneman instability," *Physics of Plasmas*, vol. 17, no. 11, p. 112317, 2010.

[40] A. Lopez Ortega, I. Katz, and V. H. Chaplin, "A first-principles model based on saturation of the electron cyclotron drift instability for electron transport in hydrodynamics simulations of Hall thruster plasmas," *Pasadena, CA: Jet Propulsion Laboratory, National Aeronautics and Space*, vol. 178, no. 1, pp. 46–56, 2017.

[41] O. Buneman, "Instability of electrons drifting through ions across a magnetic field," *Journal of Nuclear Energy. Part C, Plasma Physics, Accelerators, Thermonuclear Research*, vol. 4, no. 2, p. 111, 1962.

[42] H. Che, "Electron two-stream instability and its application in solar and heliophysics," *Modern Physics Letters A*, vol. 31, no. 19, p. 1630018, 2016.

[43] C. Nieter and J. R. Cary, "VORPAL: a versatile plasma simulation code," *Journal of Computational Physics*, vol. 196, no. 2, pp. 448–473, 2004.

[44] J. A. Byers and M. Grewal, "Perpendicularly propagating plasma cyclotron instabilities simulated with a one-dimensional computer model," *The Physics of Fluids*, vol. 13, no. 7, pp. 1819–1830, 1970.

[45] J. Hammersley and D. Handscomb, "Monte Carlo methods (Methuen & CO LTD, Ed," *London: Springer*, vol. 10, pp. 978–94, 1964.

[46] J. Gonichon, S. Chen, L.-L. Lin, and R. Temkin, "Quiet start and autotasking for PARMELA," in *Proceedings of International Conference on Particle Accelerators*, vol. 4, pp. 2696–2698, IEEE, 1993.

[47] P. Bratley and B. L. Fox, "Algorithm 659: Implementing Sobol's quasirandom sequence generator," *ACM Transactions on Mathematical Software (TOMS)*, vol. 14, no. 1, pp. 88–100, 1988.

[48] S. Parker and W. Lee, "A fully nonlinear characteristic method for gyrokinetic simulation," *Physics of Fluids B: Plasma Physics*, vol. 5, no. 1, pp. 77–86, 1993.

[49] D. Martin, "Electrostatic PIC simulation of plasmas in one dimension," tech. rep., Project Report, the university of Manchester, 2007.

[50] H. Che, J. Drake, M. Swisdak, and P. Yoon, "Nonlinear development of streaming instabilities in strongly magnetized plasma," *Physical Review Letters*, vol. 102, no. 14, p. 145004, 2009.

[51] P. Hellinger, P. Travnicek, and J. D. Menietti, "Effective collision frequency due to ion-acoustic instability: Theory and simulations," *Geophysical Research Letters*, vol. 31, no. 10, p. L10806, 2004.

[52] H. Che, J. Drake, M. Swisdak, and P. Yoon, "Electron holes and heating in the reconnection dissipation region," *Geophysical Research Letters*, vol. 37, no. 11, p. L11105, 2010.

[53] L. P. Dyrud and M. M. Oppenheim, "Electron holes, ion waves, and anomalous resistivity in space plasmas," *Journal of Geophysical Research — Space Physics*, vol. 111, no. A1, p. A01302, 2006.

[54] O. Buneman, "Instability, turbulence, and conductivity in current-carrying plasma," *Physical Review Letters*, vol. 1, no. 1, p. 8, 1958.

[55] O. Buneman, "Dissipation of currents in ionized media," *Physical Review*, vol. 115, no. 3, p. 503, 1959.

[56] I. H. Hutchinson, "Electron holes in phase space: What they are and why they matter," *Physics of Plasmas*, vol. 24, no. 5, p. 055601, 2017.

[57] F. Califano, L. Galeotti, and C. Briand, "Electrostatic coherent structures: The role of the ions dynamics," *Physics of Plasmas*, vol. 14, no. 5, p. 052306, 2007.

[58] A. Ghizzo, M. M. Shoucri, P. Bertrand, M. Feix, and E. Fijalkow, "Nonlinear evolution of the beam-plasma instabilities," *Physics Letters A*, vol. 129, no. 8-9, pp. 453–458, 1988.

[59] M. Shoucri, "Formation of electron holes in the long-time evolution of the bump-on-tail instability," *Laser and Particle Beams*, vol. 35, no. 4, p. 706, 2017.

[60] C. Villani, "Particle systems and nonlinear Landau damping," *Physics of Plasmas*, vol. 21, no. 3, p. 030901, 2014.

Appendix A

Dielectric response of plasma in the presence of magnetic field

In this appendix, the method of integration over characteristics is applied to calculate dispersion relation of the electrostatic wave in magnetized homogeneous plasma. In this method the Vlasov equation is integrated (1.40) over the unperturbed orbit of electron motion. These re-derivations are based on Ref. [8].

The distribution function based on the unperturbed orbit of a charged particle in the magnetic field **B** is defined in the form of:

$$\tilde{f}_\alpha(\mathbf{x},\mathbf{v},t) = \frac{q_\alpha}{m_\alpha}\int_{-\infty}^{t} dt'\ \nabla'\tilde{\phi}(\mathbf{x}',\mathbf{t}')\cdot\frac{\partial f_{0\alpha}(\mathbf{v}')}{\partial \mathbf{v}'}. \tag{A.1}$$

The $\tilde{f}_\alpha$ can be written in the Fourier space,

$$\tilde{f}_\alpha(\mathbf{k},\mathbf{v},\omega) = -\frac{q_\alpha}{m_\alpha}\tilde{\phi}(\mathbf{k},\omega)\int_{-\infty}^{t} dt'\ i\mathbf{k}\cdot\frac{\partial f_{0\alpha}(v')}{\partial \mathbf{v}'}\exp\{i[\mathbf{k}\cdot(\mathbf{x}'-\mathbf{x})-\omega(t'-t)]\}. \tag{A.2}$$

Integrating the first order of distribution function over the velocity yields the density of the αth component

$$\tilde{n}_\alpha(\mathbf{k},\omega) = \int \tilde{f}_\alpha d^3v = \frac{q_\alpha}{m_\alpha}\tilde{\phi}(\mathbf{k},\omega)\int d^3v\int_{-\infty}^{t} dt'\ i\mathbf{k}\cdot\frac{\partial f_{0\alpha}(\mathbf{v}')}{\partial \mathbf{v}'}\exp\{i[\mathbf{k}\cdot(\mathbf{x}'-\mathbf{x})-\omega(t'-t)]\}. \tag{A.3}$$

The density of the αth component can be rewritten by using the definition of the αth component of susceptibility K_α:

$$\tilde{n}_\alpha(\mathbf{k},\omega) = -\frac{q_\alpha n_{0\alpha}k^2}{m_\alpha\omega_{p\alpha}^2}\tilde{\phi}(\mathbf{k},\omega)K_\alpha(\mathbf{k},\omega), \tag{A.4}$$

$$K_\alpha(\mathbf{k},\omega) = -\frac{\omega_{p\alpha}^2}{n_{0\alpha}k^2}\int d^3v\int dt' i\mathbf{k}\cdot\frac{\partial f_{0\alpha}(\mathbf{v}')}{\partial \mathbf{v}'}\exp i[\mathbf{k}\cdot(\mathbf{x}'-\mathbf{x})-\omega(t'-t)]. \tag{A.5}$$

The following results can be achieved by substituting the Maxwellian zeroth-order distribution function Eq. (1.23) in Eq. (A.5) and doing some calculations:

$$K_\alpha(\mathbf{k},\omega) = \frac{k_\alpha^2}{k^2}\left[1 + \frac{i\omega}{n_{0\alpha}}\int f_{0\alpha}(\mathbf{v}')d^3v \int \exp\{i[\mathbf{k}\cdot(\mathbf{x}'-\mathbf{x}) - \omega(t'-t)]dt'\right], \tag{A.6}$$

where $k_\alpha = \omega_{p\alpha}/v_{t\alpha}$. In the presence of uniform magnetic field $\mathbf{B} = B_0\hat{z}$ in the z direction, the position and velocity of charged particle can be obtained. The unperturbed orbit for charge particle can be calculated as follows by imposing the initial assumptions $\mathbf{x}(t') = \mathbf{x}(t), \mathbf{v}(t') = \mathbf{v}(t)$ and assuming $\tau = t' - t$:

$$\begin{aligned}
v_x(t') &= v_\perp \cos(\Omega_{c\alpha}\tau - \phi),\\
v_y(t') &= v_\perp \sin(\Omega_{c\alpha}\tau - \phi),\\
v_z(t') &= v_z,\\
x(t') &= x(t) + \frac{v_\perp}{\Omega_{c\alpha}}[\sin(\Omega_{c\alpha}\tau - \phi) + \sin\phi],\\
y(t') &= y(t) + \frac{v_\perp}{\Omega_{c\alpha}}[\cos(\Omega_{c\alpha}\tau - \phi) - \cos\phi],\\
z(t') &= z(t) + v_z\tau\ ,
\end{aligned} \tag{A.7}$$

where $(v_x(t'))^2 + (v_y(t'))^2 = v_\perp^2$, remain constant. Substituting $x(t') - x(t)$, $y(t') - y(t)$, $z(t') - z(t)$, in the $\exp\{i[\mathbf{k}\cdot(\mathbf{x}'-\mathbf{x}) - \omega(t'-t)]\}$ results in:

$$\mathbf{k}\cdot(\mathbf{x}'-\mathbf{x}) = k_x\left(\frac{v_\perp}{\Omega_{c\alpha}}[\sin(\Omega_{c\alpha}\tau - \phi) + \sin\phi]\right) + k_y\left(\frac{v_\perp}{\Omega_\alpha}[\cos(\Omega_{c\alpha}\tau - \phi) - \cos\phi]\right) + [k_z(v_z\tau)]. \tag{A.8}$$

By assuming the two dimensional wave vector in $y-z$ plane with $k \equiv |\mathbf{k}| = \sqrt{k_z^2 + k_y^2}$ the αth component of susceptibility K_α can be written as follows:

$$\exp\{i[k_y\left(\frac{v_\perp}{\Omega_{c\alpha}}[\cos(\Omega_{c\alpha}\tau - \phi) - \cos\phi]\right) + [(k_z v_z) - \omega)]\tau]\} = \exp[ib_\alpha(\tau,\omega)],$$

$$K_\alpha(\mathbf{k},\omega) = \frac{k_\alpha^2}{k^2}\left[1 + \frac{i\omega}{n_{0\alpha}}\int f_{0\alpha}(\mathbf{v}')d^3v \int_{-\infty}^{0} \exp\{ib_\alpha(\tau,\omega)\}d\tau\right]. \tag{A.9}$$

This integral is commonly encountered in linear Vlasov theory. For evaluating this integral, it is convenient to put the velocity in Cartesian coordinates:

$$\begin{aligned}
K_\alpha(\mathbf{k},\omega) = \frac{k_\alpha^2}{k^2}[1 + \frac{i\omega}{n_{0\alpha}}\frac{n_{0\alpha}}{(2\pi v_{t\alpha}^2)^{3/2}}\int \exp\left(-\frac{v_x^2+v_y^2+v_z^2}{2v_{t\alpha}^2}\right)dv_x dv_y dv_z\\
\int_{-\infty}^{0} \exp\{i[k_y(\frac{v_\perp}{\Omega_\alpha}[\cos(\Omega_\alpha\tau - \phi) - \cos\phi]) + [(k_z v_z) - \omega)]\tau]\}d\tau].
\end{aligned} \tag{A.10}$$

By using $\cos(\Omega_{c\alpha}\tau - \phi) = \cos(\Omega_{c\alpha}\tau)\cos(\phi) + \sin(\Omega_{c\alpha}\tau)\sin(\phi)$ and considering $v_x = v_\perp \cos(\phi)$, $v_y = v_\perp \sin(\phi)$ as initial conditions, susceptibility can be rewritten as

$$K_\alpha(\mathbf{k},\omega) = \frac{k_\alpha^2}{k^2}[1 + A_\alpha(\mathbf{k},\omega)]. \tag{A.11}$$

Since the velocity and time integration can be interchangeable, the following known integral

$$\int_{-\infty}^{\infty} dx \exp(-\alpha x^2 \pm i\beta x) = \left(\frac{\pi}{\alpha}\right)^{1/2} \exp\left(-\frac{\beta^2}{4\alpha}\right), \tag{A.12}$$

can be used three times for each velocity component,

$$\int_{-\infty}^{\infty} dv_x \exp(-\frac{{v_x}^2}{2v_{t\alpha}^2} + i\frac{k_y v_x}{\Omega_{c\alpha}}(\cos\Omega_{c\alpha}\tau - 1)) = \left(2\pi v_{t\alpha}^2\right)^{1/2} \exp\left(-\frac{v_{t\alpha}^2(\frac{k_y}{\Omega_{c\alpha}}(\cos\Omega_{c\alpha}\tau - 1))^2}{2}\right),$$

$$\int_{-\infty}^{\infty} dv_y \exp(-\frac{{v_y}^2}{2v_{t\alpha}^2} + i(\frac{k_y v_y}{\Omega_{c\alpha}}\sin(\Omega_{c\alpha}\tau)) = \left(2\pi v_{t\alpha}^2\right)^{1/2} \exp\left(-\frac{v_{t\alpha}^2(\frac{k_y}{\Omega_{c\alpha}}\sin(\Omega_{c\alpha}\tau))^2}{2}\right),$$

and

$$\int_{-\infty}^{\infty} dv_z \exp(-\frac{{v_z}^2}{2v_{t\alpha}^2} + i(k_z v_z)\tau) = \left(2\pi v_{t\alpha}^2\right)^{1/2} \exp\left(-\frac{v_{t\alpha}^2(k_z\tau)^2}{2}\right).$$

Since $(v_{t\alpha}^2 k_y^2/\Omega_{c\alpha}^2 \geq 1)$ the Taylor expansion of the Cosine function $(1 - \cos\Omega_{c\alpha}\tau \simeq (\Omega_{c\alpha}\tau)^2/2$ can be applicable,

$$A_\alpha(\mathbf{k},\omega) = i\omega \int d\tau \exp(-i\omega\tau) \exp\left(-\frac{v_{t\alpha}^2 k_y^2 \tau^2}{2} - \frac{v_{t\alpha}^2 k_z^2 \tau^2}{2}\right). \tag{A.13}$$

By using the definition of properties of plasma dispersion function and Gordeyev integral in Eqs. (A.14)-(A.16) Ref. [8]:

$$F_\alpha(\mathbf{k},\omega) = i\int_0^{\infty} d\tau V_\alpha(\tau), \tag{A.14}$$

$$V_\alpha(\tau) \equiv \exp(i\omega\tau) \exp\left[-\lambda_\alpha \frac{(\Omega_{c\alpha}\tau)^2}{2}\right] \exp\left(-\frac{v_{t\alpha}^2 k_z^2 \tau^2}{2}\right), \tag{A.15}$$

$$F_\alpha(\mathbf{k},\omega) = \frac{\exp(-\lambda_\alpha)}{\sqrt{2}k_z v_{t\alpha}} \sum_{m=-\infty}^{m=\infty} I_m(\lambda_\alpha) Z(\zeta_\alpha^m), \tag{A.16}$$

where $I_m(x)$ is the modified Bessel function of order m and $\zeta_\alpha^m = (\omega + m\Omega_{c\alpha})/(\sqrt{2}k_z v_{t\alpha})$

and $\lambda_\alpha = (k_y a_\alpha)^2$, the susceptibility can be written in the form of:

$$A_\alpha(\mathbf{k},\omega) = i\omega \int d\tau \exp(-i(\omega)\tau \exp\left(-\frac{v_{t\alpha}^2 k_y^2 \tau^2}{2} - \frac{v_{t\alpha}^2 k_z^2 \tau^2}{2}\right)$$
$$= \frac{\omega}{\sqrt{2}k_z v_{t\alpha}} \sum_{m=-\infty}^{m=\infty} \exp\left(-\frac{k_y^2 v_{t\alpha}^2}{\Omega_{c\alpha}^2}\right) I_m\left(\frac{k_y^2 v_{t\alpha}^2}{\Omega_{c\alpha}^2}\right) Z\left(\frac{\omega + m\Omega_{c\alpha}}{\sqrt{2}k_z v_{t\alpha}}\right) \quad \text{(A.17)}$$

$$K_\alpha(\mathbf{k},\omega) = \frac{k_\alpha^2}{k^2}\left[1 + \frac{\omega}{\sqrt{2}k_z v_{t\alpha}} \sum_{m=-\infty}^{m=\infty} \exp\left(-\frac{k_y^2 v_{t\alpha}^2}{\Omega_{c\alpha}^2}\right) I_m\left(\frac{k_y^2 v_{t\alpha}^2}{\Omega_{c\alpha}^2}\right) Z\left(\frac{\omega + m\Omega_{c\alpha}}{\sqrt{2}k_z v_{t\alpha}}\right)\right]. \quad \text{(A.18)}$$

At this point making use of the Poisson's equation and the definition of αth component susceptibility, result in the linear dispersion equation of electrostatic wave in magnetized plasma in the following form:

$$1 + \sum_\alpha K_\alpha(\mathbf{k},\omega) = 0. \quad \text{(A.19)}$$

If there is a zero-order uniform electric $\mathbf{E} = -E_0\hat{x}$ in plasma like ECDI configuration, the components of velocity in x and z direction do not change, but $\mathbf{v}_E = \mathbf{E} \times \mathbf{B} = E_0/B_0\ \hat{y}$, drift velocity will be added to y component of velocity in Eq. (A.7) as a Doppler shift, and $(v_x(t'))^2 + (v_y(t') - v_E)^2$ becomes a constant of zeroth-order motion.

Appendix B

Derivation of LHDI dispersion relation

In this appendix, the local dispersion relation of LHDI by solving the Vlasov equation is re-derived. The following derivations are adapted from Ref. [23]. The main procedure is to apply Fourier/Laplace analysis in the linear Vlasov equation to obtain particle density fluctuations that can then be inserted into the Poisson equation.

B.1 Stationary equilibrium state

Before calculating the perturbed distribution function, it is convenient to determine the equilibrium electrostatic potential $\phi_0(x)$ and corresponding electric field $E_0(x)$ by imposing quasineutrality on the chosen forms of the distribution function in Eq. (3.4):

$$\begin{aligned} n_{0i} &= n_{0e}, \\ \int\int f_{0i} dv_x dv_y &= \int\int f_{0e} dv_x dv_y, \end{aligned} \tag{B.1}$$

where,

$$\begin{aligned} f_{0i}(\mathbf{x},\mathbf{v}) &= \left(\frac{m_i n_A}{2\pi T_{\perp_i}}\right) \exp\left(-\frac{m_i v_{yi}^2}{2T_{\perp i}}\right) \exp\left(-\frac{H_\perp - v_{yi} p_y}{T_{\perp i}}\right) G_i(v_z), \\ f_{0e}(\mathbf{x},\mathbf{v}) &= \left(\frac{m_e n_A}{2\pi T_{\perp_e}}\right) \exp\left(-\frac{m_e v_{ye}^2}{2T_{\perp e}}\right) \exp\left(-\frac{H_\perp - v_{ye} p_y}{T_{\perp e}}\right) G_e(v_z). \end{aligned}$$

By solving this equality, the electrostatic potential and constant electric field can be determined in the form of:

$$\phi_0(x) = \frac{T_{\perp e} T_{\perp i} B_0}{(T_{\perp e} + T_{\perp i})} \left(\frac{v_{ye}}{T_{\perp e}} - \frac{v_{yi}}{T_{\perp i}}\right) x, \tag{B.2}$$

$$E_0(x) = \frac{T_{\perp e} T_{\perp i} B_0}{(T_{\perp e} + T_{\perp i})} \left(\frac{v_{yi}}{T_{\perp i}} - \frac{v_{ye}}{T_{\perp e}}\right). \tag{B.3}$$

The integration of the distribution function for each species yields the density profile, which is used to determine plasma thickness (d),

$$n_A \exp\left(-\frac{x}{d}\right) = \int\int f_{0e} dv_x dv_y,$$
$$d = \frac{T_{\perp e} + T_{\perp i}}{eB_0(v_{ye} + v_{yi})}. \tag{B.4}$$

Here v_{ye} and v_{yi} are electron and ion flow velocities, respectively, for which at least the value of one of them must be known. In some cases $v_{yi} = 0$ is assumed. However, it is common to define a coefficient of r as the ratio of these flow velocities and rewrite the electrostatic potential and the electric field based on these constant parameters

$$r = \frac{v_{yi}}{v_{ye}}, \tag{B.5}$$
$$\phi_0(x) = \left[\frac{(T_{\perp i} - T_{\perp e} r)}{e(1+r)}\right]\left(\frac{x}{d}\right), \tag{B.6}$$
$$E_0(x) = \left[\frac{(T_{\perp e} r - T_{\perp i})}{e(1+r)d}\right], \tag{B.7}$$
$$v_{ye} = \frac{(T_{\perp e} + T_{\perp i})}{eB_0 d(1+r)}. \tag{B.8}$$

By defining the equilibrium distribution function, it's time to evaluate the perturbed distribution function.

B.2 Integration over trajectory

By considering the weak plasma fluctuations, the Vlasov equation can be linearized

$$\frac{\partial \tilde{f}_\alpha(\mathbf{x},\mathbf{v},t)}{\partial t} + \mathbf{v}\cdot\frac{\partial \tilde{f}_\alpha(\mathbf{x},\mathbf{v},t)}{\partial \mathbf{x}} + \frac{q_\alpha}{m_\alpha}(\mathbf{E}+\mathbf{v}\times\mathbf{B})\cdot\frac{\partial \tilde{f}_\alpha(\mathbf{x},\mathbf{v},t)}{\partial \mathbf{v}} = -\frac{q_\alpha}{m_\alpha}\tilde{\mathbf{E}}(\mathbf{x},t)\cdot\frac{\partial f_{0\alpha}(\mathbf{x},\mathbf{v})}{\partial \mathbf{v}}. \tag{B.9}$$

and rearrange based on the distribution function,

$$\left[\frac{\partial}{\partial t} + \mathbf{v}\cdot\frac{\partial}{\partial \mathbf{x}} + \frac{q_\alpha}{m_\alpha}(\mathbf{E}_0+\mathbf{v}\times\mathbf{B}_0)\cdot\frac{\partial}{\partial \mathbf{v}}\right]\tilde{f}_\alpha(\mathbf{x},\mathbf{v},t) = \frac{q_\alpha}{m_\alpha}\nabla\tilde{\phi}(\mathbf{x},t)\left[m_\alpha(\mathbf{v}-v_z\hat{z})\frac{\partial f_{0\alpha}}{\partial H_\perp} + m_\alpha\hat{y}\frac{\partial f_{0\alpha}}{\partial p_y} + \hat{z}\frac{\partial f_{0\alpha}}{\partial v_z}\right]. \tag{B.10}$$

In the right-hand side of Eq. (B.10), the Laplace transformation in (t) for the perturbed electrostatic potential is employed in the form of:

$$\tilde{\phi}(\mathbf{x},t) = \tilde{\phi}(\mathbf{x})\exp(-i\omega t), \quad \text{Im}\ \omega > 0. \tag{B.11}$$

The Eq. (B.10) is integrated from $t' = -\infty$ to $t' = t$ by assuming the intial perturbation to be zero and v_z, $\partial f_{0\alpha}/\partial H_\perp$, and $\partial f_{0\alpha}/\partial v_z$ to be constant along unperturbed particle

trajectory:

$$\tilde{f}_\alpha(\mathbf{x},\mathbf{v},t) = \frac{q_\alpha}{m_\alpha}\left(\frac{\partial f_{0\alpha}}{\partial v_z} - m_\alpha v_z \frac{\partial f_{0\alpha}}{\partial H_\perp}\right) \times \int_{-\infty}^{t'} dt' \exp(-i\omega t') \frac{\partial}{\partial z'}\tilde{\phi}(\mathbf{x}'(t'))+$$
$$q_\alpha \frac{\partial f_{0\alpha}}{\partial H_\perp}\int_{-\infty}^{t'} dt' \times \exp(-i\omega t')\mathbf{v}'(t')\cdot\nabla'\tilde{\phi}(\mathbf{x}'(t') + q_\alpha \frac{\partial f_{0\alpha}}{\partial p_y}\int_{-\infty}^{t'} dt' \times \exp(-i\omega t')\frac{\partial}{\partial y'}\tilde{\phi}(\mathbf{x}'(t')). \tag{B.12}$$

Particle trajectories $\mathbf{x}'(t')$ and $\mathbf{v}'(t')$ satisfy the following single particle equation of motion

$$\begin{aligned}\frac{d}{dt'}\mathbf{x}' &= v',\\ \frac{d}{dt'}\mathbf{v}' &= \frac{q_\alpha}{m_\alpha}(\mathbf{E}(x') + \mathbf{v}'\times\mathbf{B}).\end{aligned} \tag{B.13}$$

The perturbed distribution function ca be achieved by making use of

$$\mathbf{v}'(t')\cdot\nabla'\tilde{\phi} = \frac{d}{dt'}\tilde{\phi}(x'), \tag{B.14}$$

and performing integration by parts

$$\begin{aligned}\tilde{f}_\alpha(\mathbf{x},\mathbf{v},t) = \frac{q_\alpha}{m_\alpha}\left(\frac{\partial f_{0\alpha}}{\partial v_z} - m_\alpha v_z \frac{\partial f_{0\alpha}}{\partial H_\perp}\right) \times \int_{-\infty}^{t} dt' \exp(-i\omega t') \frac{\partial}{\partial z'}\tilde{\phi}(\mathbf{x}'(t'))+\\ q_\alpha \frac{\partial f_{0\alpha}}{\partial H_\perp}\exp(-i\omega t)\tilde{\phi}(\mathbf{x}) + i\omega q_\alpha \frac{\partial f_{0\alpha}}{\partial H_\perp}\int_{-\infty}^{t} dt' \times \exp(-i\omega t')\tilde{\phi}(\mathbf{x}'(t')+\\ q_\alpha \frac{\partial f_{0\alpha}}{\partial p_y}\int_{-\infty}^{t} dt' \times \exp(-i\omega t')\frac{\partial}{\partial y'}\tilde{\phi}(\mathbf{x}'(t')),\end{aligned} \tag{B.15}$$

and then employing the Fourier transformation in y and z,

$$\begin{aligned}\tilde{\phi}(\mathbf{x}) &= \tilde{\phi}(x)\exp[i(k_y y + k_z z)],\\ \tilde{f}_\alpha(\mathbf{x},\mathbf{v},t) &= \tilde{f}_\alpha(x,\mathbf{v})\exp[i(k_y y + k_z z - \omega t)],\end{aligned} \tag{B.16}$$

in the form of:

$$\tilde{f}_\alpha(x,\mathbf{v}) = \frac{q_\alpha}{m_\alpha}\left(\frac{\partial f_{0\alpha}}{\partial v_z} - m_\alpha v_z \frac{\partial f_{0\alpha}}{\partial H_\perp}\right) ik_z I + q_\alpha \frac{\partial f_{0\alpha}}{\partial H_\perp}\tilde{\phi} + iq_\alpha\omega\frac{\partial f_{0\alpha}}{\partial H_\perp} I + ik_y q_\alpha \frac{\partial f_{0\alpha}}{\partial p_y} I, \tag{B.17}$$

where

$$I = \int_{-\infty}^{0} d\tau \exp(-i\omega\tau)\tilde{\phi}(x'(\tau)) \times \exp[ik_y(y(\tau) - y(0)) + ik_z(z(\tau) - z(0))]. \tag{B.18}$$

Lower-hybrid drift instability is characterized by strongly magnetized electrons and unmagnetized ions, $\Omega_{ci} << |\omega| << \Omega_{ce}$, where $k_z = 0$. As a result, for calculating the electron-perturbed distribution function, the integration along the unperturbed orbits, and for ions, the usual approximation that they are unmagnetized are performed. At this

point the perturbed electron distribution function is considered

$$\tilde{f}_e(x,v) = \frac{e}{T_{\perp e}} f_{0e}\tilde{\phi} + i\frac{e\omega}{T_{\perp e}} f_{0e} I - i\frac{k_y e v_{ye}}{T_{\perp e}} f_{0e} I. \tag{B.19}$$

Instead of using the Cartesian form of velocity, it is convenient to use the cylindrical coordinate $(v_\perp, \theta, v_z)$,

$$\begin{aligned} v_\perp \cos\theta &= v_x, \\ v_\perp \sin\theta &= v_y - v_{ye}. \end{aligned} \tag{B.20}$$

The following unperturbed orbits are inserted into the Eq. (B.18),

$$\begin{aligned} y(\tau) - y(0) &= v_E\tau - \frac{1}{\Omega_{ce}}[\cos(\Omega_{ce}\tau)v_\perp\cos\theta - \sin(\Omega_{ce}\tau) \times (-v_E + v_{ye} + v_\perp\sin\theta) - v_\perp\cos\theta)], \\ z(\tau) - z(0) &= v_z\tau, \end{aligned} \tag{B.21}$$

where v_E is drift velocity

$$v_E = -E_0/B_0 = \frac{1}{eB_0 d}\frac{T_{\perp i} - T_{\perp e} r}{(1+r)}, \tag{B.22}$$

and v_{ne} is diamagnetic drift

$$v_{ne} = \frac{1}{en_{0e}B_0}\frac{\partial(n_{0e}T_{\perp e})}{\partial x} = -\frac{T_{\perp e}}{eB_0 d}, \tag{B.23}$$

which yield to $v_{ye} = v_E + v_{ne}$. Therefore the integral I is written in the form of:

$$I = \tilde{\phi}\int d\tau \exp(-i(\omega - k_y v_E)\tau) \times \exp\left[ik_y\left(-\frac{1}{\Omega_{ce}}(v_\perp[\cos(\Omega_{ce}\tau+\theta)] - \sin(\Omega_{ce}\tau)\times(-v_E+v_{ye}) - v_\perp\cos\theta)\right)\right]. \tag{B.24}$$

The following identity has been used

$$\exp(-iz\sin\Psi) = \sum_{n=-\infty}^{\infty}\exp(-in\Psi)J_n(z), \tag{B.25}$$

to simplify the exponential part of Eq. (B.18) where J_n shows Bessel function of order of n,

$$\exp\left(-\frac{ik_y v_\perp}{\Omega_{ce}}[\sin(\Omega_{ce}\tau + \theta + \frac{\pi}{2}) - \sin(\theta + \frac{\pi}{2})\right) = \sum_{n=-\infty}^{\infty}\sum_{m=-\infty}^{\infty}\exp(-i[n(\Omega_{ce}\tau+\theta) - m\theta)J_n\left(\frac{v_\perp k_y}{\Omega_{ce}}\right)J_m\left(\frac{v_\perp k_y}{\Omega_{ce}}\right), \tag{B.26}$$

and

$$\exp\left(-ik_y\frac{1}{\Omega_{ce}}\sin(\Omega_{ce}\tau)\times(-v_E+v_{ye})\right)=\sum_{l=-\infty}^{\infty}\exp(il\Omega_{ce}\tau)J_{-l}\left(k_y\frac{v_{ne}}{\Omega_{ce}}\right). \tag{B.27}$$

Therefore, the simplification results in

$$I=\sum_{l=-\infty}^{\infty}\sum_{n=-\infty}^{\infty}\sum_{m=-\infty}^{\infty}\tilde{\phi}\int d\tau\exp(-i(\omega-k_yv_E)\tau)\times\exp(-i[n(\Omega_{ce}\tau+\theta)-m\theta) \\ J_n\left(\frac{v_\perp k_y}{\Omega_{ce}}\right)J_m\left(\frac{v_\perp k_y}{\Omega_{ce}}\right)\times\exp(il\Omega_{ce}\tau)J_{-l}\left(k_y\frac{v_{ne}}{\Omega_{ce}}\right). \tag{B.28}$$

By integrating the perturbed electron distribution function over the velocity space, the perturbed electron density can now be determined as

$$\tilde{\rho}_e=-e\int d^3v\tilde{f}_e=-e\int dv_xdv_ydv_z\left(\frac{e}{T_{\perp e}}f_{0e}\tilde{\phi}+i\frac{e\omega}{T_{\perp e}}f_{0e}I-i\frac{k_yev_{ye}}{T_{\perp e}}f_{0e}I\right)G_e(v_z). \tag{B.29}$$

One obtains by considering the normalization condition $\int_{-\infty}^{\infty}dv_zG_e(v_z)=1$,

$$\tilde{\rho}_e=-e\int d^3v\tilde{f}_e=-e\int dv_xdv_y\left(\frac{e}{T_{\perp e}}f_{0e}\tilde{\phi}\right)-e^2i\left(\frac{\omega-k_yv_{ye}}{T_{\perp e}}\right)\int dv_xdv_yf_{0e}I. \tag{B.30}$$

For calculating the perturbed electron density (B.30), this integral is split into two terms. For the first term, the definition of the first moment of distribution function that results the density profile is used

$$\text{Term1}=-e\int dv_xdv_y\left(\frac{e}{T_{\perp e}}f_{0e}\tilde{\phi}\right)=-\frac{n_Ae^2}{T_{\perp e}}\tilde{\phi}\exp\left(-\frac{x}{d}\right). \tag{B.31}$$

Instead of using the Cartesian coordinates to calculate the second term of Eq. (B.18) it is more convenient to use the cylindrical coordinate

$$\text{Term2}=-e^2i\left(\frac{\omega-k_yv_{ye}}{T_{\perp e}}\right)\int\int dv_xdv_yf_{0e}I=-e^2i\left(\frac{\omega-k_yv_{ye}}{T_{\perp e}}\right)\int\int v_\perp dv_\perp d\theta f_{0e}I, \tag{B.32}$$

$$f_{0e}=\left(\frac{m_en_A}{2\pi T_{\perp e}}\right)\exp\left(-\frac{m_e}{2T_{\perp e}}(v_y-v_{ye})^2\right)\exp\left(-\frac{m_ev_x^2}{2T_{\perp e}}\right)\exp\left(-\frac{x}{d}\right)= \\ \left(\frac{m_en_A}{2\pi T_{\perp e}}\right)\exp\left(-\frac{x}{d}\right)\exp\left(-\frac{m_e}{2T_{\perp e}}v_\perp^2\right), \tag{B.33}$$

$$\text{Term2}=-e^2i\left(\frac{\omega-k_yv_{ye}}{T_{\perp e}}\right)\int\int\int\sum_{l=-\infty}^{\infty}\sum_{n=-\infty}^{\infty}\sum_{m=-\infty}^{\infty}v_\perp dv_\perp d\theta d\tau f_{0e}\exp(-i(\omega-k_yv_E)\tau) \\ \times\exp(-i[n(\Omega_e\tau+\theta)-m\theta)J_n\left(\frac{v_\perp k_y}{\Omega_{ce}}\right)J_m\left(\frac{v_\perp k_y}{\Omega_{ce}}\right)\times\exp(il\Omega_{ce}\tau)J_{-l}\left(k_y\frac{v_{ne}}{\Omega_{ce}}\right). \tag{B.34}$$

The double summation over m and n is simplified by eliminating the repetitive terms,

$$\sum_{n=-\infty}^{\infty}\sum_{m=-\infty}^{\infty}\exp(-i[n(\Omega_{ce}\tau+\theta)-m\theta)J_n\left(\frac{v_\perp k_y}{\Omega_{ce}}\right)J_m\left(\frac{v_\perp k_y}{\Omega_{ce}}\right) = \sum_{n=-\infty}^{\infty}\exp(-in\Omega_{ce}\tau)J_n^2\left(\frac{v_\perp k_y}{\Omega_{ce}}\right), \quad \text{(B.35)}$$

$$\text{Term2}= -e^2 i\left(\frac{\omega-k_y v_{ye}}{T_{\perp e}}\right)\left(\frac{m_e n_A}{2\pi T_{\perp e}}\right)\tilde{\phi}\exp\left(-\frac{x}{d}\right)\int\int\int\sum_{l=-\infty}^{\infty}\sum_{n=-\infty}^{\infty}v_\perp dv_\perp d\theta d\tau \exp\left(-\frac{m_e}{2T_{\perp e}}v_\perp^2\right)\exp(-i(\omega-k_y v_E-(n-l)\Omega_{ce})\tau)J_n^2\left(\frac{v_\perp k_y}{\Omega_{ce}}\right)J_{-l}\left(k_y\frac{v_{ne}}{\Omega_{ce}}\right). \quad \text{(B.36)}$$

The following result is obtained by extending the summation over n and l and eliminating the repetitive sin and cos terms and considering the below properties of Bessel function (B.37):

$$\int\sum_{l=-\infty}^{\infty}v_\perp dv_\perp\frac{m_e}{T_{\perp e}}\exp\left(-\frac{m_e}{2T_{\perp e}}v_\perp^2\right)J_l^2\left(\frac{v_\perp k_y}{\Omega_{ce}}\right) = I_l\left(\frac{k_y^2 T_{\perp e}}{\Omega_{ce}^2 m_e}\right)\exp\left(-\frac{k_y^2 T_{\perp e}}{\Omega_{ce}^2 m_e}\right), \quad \text{(B.37)}$$

$$\text{Term2}= -e^2 i\left(\frac{\omega-k_y v_{ye}}{T_{\perp e}}\right)\left(\frac{n_A}{2\pi}\right)\tilde{\phi}\exp\left(-\frac{x}{d}\right)\int\int\sum_{l=-\infty}^{\infty}d\theta d\tau I_l\left(\frac{k_y^2 T_{\perp e}}{\Omega_{ce}^2 m_e}\right) \exp\left(-\frac{k_y^2 T_{\perp e}}{\Omega_{ce}^2 m_e}\right)\exp(-i(\omega-k_y v_E)\tau)J_{-l}\left(k_y\frac{v_{ne}}{\Omega_{ce}}\right). \quad \text{(B.38)}$$

Double integral of Term2 over θ and τ results in

$$\text{Term2}=\frac{e^2 n_A}{T_{\perp e}}(\omega-k_y v_{ye})\tilde{\phi}\exp\left(-\frac{x}{d}\right)\sum_{l=-\infty}^{\infty}\frac{I_l\left(\frac{k_y^2 T_{\perp e}}{\Omega_{ce}^2 m_e}\right)\exp\left(-\frac{k_y^2 T_{\perp e}}{\Omega_{ce}^2 m_e}\right)J_{-l}\left(k_y\frac{v_{ne}}{\Omega_{ce}}\right)}{(\omega-k_y v_E)}. \quad \text{(B.39)}$$

Electron flow velocity can be written based on diamagnetic drift velocity and $\mathbf{E}\times\mathbf{B}$ drift velocity, v_E

$$\frac{\omega-k_y v_{ye}}{\omega-k_y v_E} = 1-\frac{k_y v_{ne}}{\omega-k_y v_E}, \quad \text{(B.40)}$$

Then

$$\text{Term2}= -\frac{e^2 n_A}{T_{\perp e}}\tilde{\phi}\exp\left(-\frac{x}{d}\right)\left(-1+\frac{k_y v_{ne}}{\omega-k_y v_E}\right)\sum_{l=-\infty}^{\infty}I_l(\zeta)\exp(-\zeta)J_{-l}\left(k_y\frac{v_{ne}}{\Omega_{ce}}\right), \quad \text{(B.41)}$$

where $\zeta = k_y^2 T_{\perp e}/(\Omega_{ce}^2 m_e) = k_y^2 \rho_e^2$. Therefore, the perturbed electron density can be calculated in the form of:

$$\tilde{\rho}_e = -\frac{n_A e^2}{T_{\perp e}}\tilde{\phi}\exp\left(-\frac{x}{d}\right) - \frac{e^2 n_A}{T_{\perp e}}\tilde{\phi}\exp\left(-\frac{x}{d}\right)\left(-1+\frac{k_y v_{ne}}{\omega - k_y v_E}\right) \sum_{l=-\infty}^{\infty} I_l(\zeta)\exp(-\zeta)J_{-l}\left(k_y\frac{v_{ne}}{\Omega_{ce}}\right). \quad \text{(B.42)}$$

By assuming

$$\sum_{l=-\infty}^{\infty} I_l(\zeta)J_{-l}\left(k_y\frac{v_{ne}}{\Omega_{ce}}\right) = S, \quad \text{(B.43)}$$

one can obtain

$$\tilde{\rho}_e = -\frac{n_A e^2}{T_{\perp e}}\tilde{\phi}\exp\left(-\frac{x}{d}\right) \times \left(1 - S\exp(-\zeta) + \frac{k_y v_{ne}}{\omega - k_y v_E} S\exp(-\zeta)\right). \quad \text{(B.44)}$$

Since

$$k_y\frac{v_{ne}}{\Omega_{ce}} = \frac{(k_y\rho_e)^2}{k_y d}, \quad \text{(B.45)}$$

and this study is focused on the case of $(k_y\rho_e)^2 \leq 1$ and large kd, the wavelength of the perturbation is comparable to ρ_e and it is much smaller than the plasma thickness. Therefor S is approximated as the first term of the modified Bessel function, $S = I_0(\xi)$.

Now turn to the ions; since the wave frequency is assumed to be much larger than the ion cyclotron frequency, the usual approximation that ions are unmagnetized is used:

$$\left[\frac{\partial}{\partial t} + \mathbf{v}\cdot\nabla\right]\tilde{f}_i = \frac{e}{m_i}\nabla\tilde{\phi}\frac{\partial f_{0i}}{\partial v}, \quad \text{(B.46)}$$

$$\tilde{f}_i(\mathbf{x},\mathbf{v},t) = \tilde{f}_i(x,\mathbf{v})\exp(i\left(k_y y - \omega t\right)), \quad \text{(B.47)}$$

$$\tilde{f}_i = -\frac{e}{m_i(\omega - k_y v_y)}\tilde{\phi}k_y\frac{\partial f_{0i}}{\partial v_y}. \quad \text{(B.48)}$$

As a result, the integral of the perturbed ion distribution function yields the perturbed ion density

$$\tilde{\rho}_i = e\int d^3v\tilde{f}_i = \frac{-e^2}{m_i}\tilde{\phi}\int\frac{d^3v}{(\omega - k_y v_y)}k_y\frac{\partial f_{0i}}{\partial v_y} = \frac{-e^2}{m_i}\tilde{\phi}\int\frac{d^3v}{(\omega - k_y v_y)}k_y\frac{\partial f_{0i}}{\partial v_y}. \quad \text{(B.49)}$$

By making use of unperturbed ion distribution function

$$f_{0i} = \left(\frac{m_i n_A}{2\pi T_{\perp i}}\right)\exp\left(-\frac{m_i}{2T_{\perp i}}(v_y - v_{yi})^2\right)\exp\left(-\frac{m_i v_x^2}{2T_{\perp i}}\right)\exp\left(-\frac{x}{d}\right)G_i(v_z), \quad \text{(B.50)}$$

and

$$\frac{\partial f_{0i}}{\partial v_y} = -\frac{m_i}{T_{\perp i}}(v_y - v_{yi}) f_{0i}, \tag{B.51}$$

the perturbed ion density results in the form of:

$$\tilde{\rho}_i = \left(\frac{e^2 m_i n_A}{2\pi T_{\perp i}^2}\right) \tilde{\phi} \exp\left(-\frac{x}{d}\right) \int \frac{G_i(v_z) d^3 v}{(\omega - k_y v_y)} k_y (v_y - v_{yi}) \exp\left(-\frac{m_i}{2T_{\perp i}}(v_y - v_{yi})^2\right) \exp\left(-\frac{m_i v_x^2}{2T_{\perp i}}\right). \tag{B.52}$$

As a result of normalization condition $\int_{-\infty}^{\infty} dv_z G_e(v_z) = 1$ and using predefined integral (A.12) one obtain

$$\tilde{\rho}_i = \frac{e^2 m_i n_A}{2\pi T_{\perp i}^2} \tilde{\phi} \sqrt{\frac{2T_{\perp i}\pi}{m_i}} \exp\left(-\frac{x}{d}\right) \int \frac{dv_y}{(\omega - k_y v_y)} k_y (v_y - v_{yi}) \exp\left(-\frac{m_i}{2T_{\perp i}}(v_y - v_{yi})^2\right). \tag{B.53}$$

This integral can be recast by defining $v_y - v_{yi} = X$

$$\tilde{\rho}_i = -\frac{e^2 m_i n_A}{2\pi T_{\perp i}^2} \tilde{\phi} \sqrt{\frac{2T_{\perp i}\pi}{m_i}} \exp\left(-\frac{x}{d}\right) \int \frac{X dX}{(X - (\frac{\omega - k_y v_{yi}}{k_y}))} \exp\left(-\frac{X^2}{2v_{ti}^2}\right), \tag{B.54}$$

and changing the variable $X/\sqrt{2}v_{ti} = W$, where v_{ti} is the ion thermal velocity $v_{ti} = \sqrt{T_{\perp i}/m_i}$,

$$\tilde{\rho}_i = -\frac{e^2 m_i n_A}{2\pi T_{\perp i}^2} \tilde{\phi} \sqrt{\frac{2T_{\perp i}\pi}{m_i}} \exp\left(-\frac{x}{d}\right) \sqrt{2} v_{ti} \int \frac{W dW}{\left(W - (\frac{\omega - k_y v_{yi}}{\sqrt{2} v_{ti} k_y})\right)} \exp(-W^2), \tag{B.55}$$

$$\tilde{\rho}_i = -\frac{e^2 n_A}{\sqrt{\pi} T_{\perp i}} \tilde{\phi} \exp\left(-\frac{x}{d}\right) \int \frac{W dW}{\left(W - (\frac{\omega - k_y v_{yi}}{\sqrt{2} v_{ti} k_y})\right)} \exp(-W^2). \tag{B.56}$$

The following result, can be obtained by using the definition of plasma dispersion function $Z(\xi)$ and its property mentioned in Eq. (1.33):

$$\tilde{\rho}_i = -\frac{e^2 n_A}{T_{\perp i}} \tilde{\phi} \exp\left(-\frac{x}{d}\right) \left[1 + \frac{\omega - k_y v_{yi}}{\sqrt{2} v_{ti} k_y} \frac{1}{\sqrt{\pi}} \int \frac{dW \exp(-W^2)}{(W - (\frac{\omega - k_y v_{yi}}{\sqrt{2} v_{ti} k_y}))}\right], \tag{B.57}$$

$$\tilde{\rho}_i = -\frac{e^2 n_A}{T_{\perp i}} \tilde{\phi} \exp\left(-\frac{x}{d}\right) \left[1 + \left(\frac{\omega - k_y v_{yi}}{\sqrt{2} v_{ti} k_y}\right) Z\left(\frac{\omega - k_y v_{yi}}{\sqrt{2} v_{ti} k_y}\right)\right]. \tag{B.58}$$

At this point the electron and ion charge densities can be substituted into Poisson's equation:

$$\nabla^2 \tilde{\phi}(x) = -\frac{(\tilde{\rho}_e + \tilde{\rho}_i)}{\epsilon_0}, \tag{B.59}$$

$$\frac{d^2\tilde{\phi}(x)}{d^2x} - k^2\tilde{\phi} = -\frac{(\tilde{\rho}_e + \tilde{\rho}_i)}{\epsilon_0}, \tag{B.60}$$

$$\frac{d^2\tilde{\phi}(x)}{d^2x} - \left(k^2 + \frac{1}{\lambda_{De}^2}\exp\left(-\frac{x}{d}\right)\left(1 - I_0(\zeta)\exp(-\zeta) + \left(\frac{k_y v_{ne}}{\omega - k_y v_E}\right) I_0(\zeta)\exp(-\zeta) + \right.\right.$$
$$\left.\left.\frac{T_{\perp e}}{T_{\perp i}}\left[1 + \left(\frac{\omega - k_y v_{yi}}{v_{ti}k_y}\right) Z\left(\frac{\omega - k_y v_{yi}}{v_{ti}k_y}\right)\right]\right)\right)\tilde{\phi} = 0. \tag{B.61}$$

Here $\lambda_{De} = \sqrt{\epsilon_0 T_{\perp e}/n_A e^2}$ is the electron Debye length. Integrodifferential for potential of the perturbation is:

$$\frac{d^2\tilde{\phi}(x)}{d^2x} - q(x,\omega,k)\tilde{\phi}(x) = 0, \tag{B.62}$$

where $q(x,\omega,k)$ is the potential function, and by equating this function to zero the local dispersion relation of LHDI at the point of $x_0 = 0$ can be achieved in the form of:

$$q(x_0,\omega,k) = 0, \tag{B.63}$$

$$k^2 + \frac{1}{\lambda_{De}^2}\left(1 - \left(1 - \frac{k_y v_{ne}}{\omega - k_y v_E}\right) I_0(\zeta)\exp(-\zeta) + \frac{T_{\perp e}}{T_{\perp i}}\left[1 + \left(\frac{\omega - k_y v_{yi}}{v_{ti}k_y}\right) Z\left(\frac{\omega - k_y v_{yi}}{v_{ti}k_y}\right)\right]\right) = 0. \tag{B.64}$$